ELECTROMAGNETIC SCATTERING BY FLAKES OF ARBITRARY REFRACTIVE INDEX: THEORY, EXPERIMENT AND APPLICATION

By

KARL WILHELM TOMAS WALDEMARSSON

A DISSERTATION PRESENTED TO THE GRADUATE SCHOOL
OF THE UNIVERSITY OF FLORIDA IN PARTIAL FULFILLMENT
OF THE REQUIREMENTS FOR THE DEGREE OF
DOCTOR OF PHILOSOPHY

UNIVERSITY OF FLORIDA

2001

To my family and Karen

ACKNOWLEDGMENTS

I would like to thank a number of people who have contributed to my education and well being throughout my graduate work at the University of Florida. First and foremost, I wish to express my gratitude to my advisor and friend, Bo Gustafson, for his continued support, understanding and encouragement. During my Ph.D. studies Bo allowed me independence and freedom to pursue my research project, and yet, he was always there to offer guidance when needed.

My thanks are also extended to Stanley Dermott, Robert Piña and Ewan Thomson for serving on my graduate committee and for their encouragement and many helpful suggestions.

I wish to express my appreciation to my present and former colleagues at the Laboratory for Astrophysics for their friendship and research assistance. I would especially like to thank Ludmilla Kolokolova for her enthusiastic support, guidance and for always being willing to provide assistance – also during very hectic times; Yu-Lin Xu for helpful discussions on this project and theoretical light scattering in general; and Joanna Thomas-Osip for introducing me to the microwave scattering facility and for offering many helpful advice when I first arrived in Gainesville.

I gratefully appreciate the financial support for this research that was provided by "The University of Florida – Royal Institute of Technology, Stockholm Fellowship in Astrophysics and Space Technology".

I am indebted to Frank Giovane for his advice, support and friendship. I am very fortunate to have had the opportunity to learn from his expertise in instrumentation development and invaluable experience in project management.

Special thanks go to the Astronomy office staff Ann Elton, Debra Hunter, Audrey Sims, Glenda Smith, Janice Douglas and Tracey Phillips, for their generous help with administrative procedures and support when needed. I would also like to acknowledge Brent Nelson and Mark Wood for their assistance with computer related matters.

I would like to extend a most sincere thank you to the staff of the Physics and Astronomy machine shop for providing most of the precision plates used for the test measurements in the microwave scattering facility. I would especially like to thank Edward Storch, Marc Link and Robert Fowler for always being willing to offer valuable advice or to make an urgently needed piece.

I thank fellow graduate students Robert Hueckstaedt, Todd Vaccaro, Elizabeth Holmes, Veera Boonyiasait, Pimol Moth and Elisha Polomski, for their good friendship and for providing many fun and healthy distractions from graduate work.

Finally, my greatest depth of gratitude goes to my family; to my mother, Rut, who has always been there for me throughout these years; to my father, Sixten, who I know is always with me in spirit; to my sister, Ulrika, for always giving me support and showing me what is important in life; to my extended family in France and England for their enthusiastic encouragement. Above all, I would like to give the highest recognition to my wife, Karen, for her love and encouragement that gave me strength and confidence. I am ever grateful for her patience and the sacrifice that she has made, especially during this last year of my education. To my family and wife I dedicate this dissertation.

TABLE OF CONTENTS

page

ACKNOWLEDGMENTS iii

ABSTRACT vii

CHAPTERS

1 INTRODUCTION 1

1.1 Background 1
1.2 Light Scattering by Flakes – a Review 2
1.3 New Approach for Light Scattering by Thin Flakes 6
1.4 Conventions and Notation 8
1.5 Outline of the Dissertation 9

2 GEOMETRICAL THEORY OF DIFFRACTION 10

2.1 Edge Diffraction 13
2.2 Multiple Diffracted Fields 25
2.3 Impedance Boundary Conditions 33
2.4 Equivalent Currents 38

3 LABORATORY MICROWAVE SCATTERING MEASUREMENTS 44

3.1 Analog-to-Light Microwave Scattering Technique 44
3.2 Microwave Scattering Facility 45
  3.2.1 Modes of Operation 49
  3.2.2 Calibration 52

4 SCATTERING BY A DIELECTRIC FLAKE OF FINITE THICKNESS 54

4.1 External Scattered Field 56
4.2 Transmitted Scattered Field 64
4.3 Total Scattered Field 71

5 ASSESSMENT OF THE SCATTERING MODEL 74

5.1 Fixed Orientation 75
5.2 Average over Rotation 93
5.3 Scattering Model in the Geometrical Optics Regime 105
5.4 Comparison to DDA 109
5.5 Shape Dependence 114
5.6 Average over Rotation versus Average over Random Orientation 119
5.7 Summary 123

6 LIGHT SCATTERING PROPERTIES OF FLAKES 124

6.1 Intensity and Polarization 124
  6.1.1 Dependence on the thickness 125
  6.1.2 Dependence on the large dimensions 128
  6.1.3 Dependence on the refractive index 132
  6.1.4 Poly-dispersion 134
6.2 Spectral Properties 138
6.3 The inverse Problem 139

7 FLAKES IN COMETARY ATMOSPHERES 144

7.1 What is a Comet? 145
7.2 Cometary Dust Flakes 145
7.3 Observations of C/1995 O1 (Hale-Bopp) 147
7.4 Modeling of Cometary Flakes 148
7.5 Comparison with Observations 154
7.6 Summary 156

8 SUMMARY AND CONCLUSIONS 157

APPENDIX PRINCIPLE OF ELECTRODYNAMIC SIMILITUDE 161

LIST OF REFERENCES 165

BIOGRAPHICAL SKETCH 171

Abstract of Dissertation Presented to the Graduate School
of the University of Florida in Partial Fulfillment of the
Requirements for the Degree of Doctor of Philosophy

ELECTROMAGNETIC SCATTERING BY FLAKES OF ARBITRARY REFRACTIVE INDEX: THEORY, EXPERIMENT AND APPLICATION

By

Karl Wilhelm Tomas Waldemarsson

December 2001

Chairman: Bo Å. S. Gustafson
Major Department: Astronomy

The focus of this study is to investigate how flake-like particles may be recognized by their light scattering properties. We develop a new theoretical model for electromagnetic scattering by flakes of arbitrary refractive index within the framework of geometrical theory of diffraction. The validity of the model is determined by comparison with microwave scattering measurements. We find that our scattering model allows us to efficiently and accurately simulate the scattering by a thin flake, with a size down to a few wavelengths in extent. It is shown how our model bridges the gap between low-frequency methods, such as DDA, and high-frequency approximations such as geometrical optics, and offers a valuable alternative when a large parameter space is to be examined.

The scattering model is used to investigate the light scattering properties of a thin flake averaged over rotation. In particular, we study the dependence of the linear polarization, color and polarimetric color on the refractive index and geometrical dimensions of the flake. Results from these simulations include both polarimetric and spectral scattering characteristics, which may be used as indicators for flake-like particles. The polarization is generally positive of a bell-like shape. The location of polarization maximum is basically determined by the Brewster angle of the flake's surface. Due to that the scattering by flakes is dominated by the specular reflections off the flake's surfaces, the polarization curve may be similar to very large, randomly oriented, scatterers. For relatively transparent flakes, interference causes correlated wavelength dependence in intensity and polarization. Interference may, for smaller flakes, shift the polarization maximum to smaller or larger scattering angles. For flakes with larger dimensions, interference may cause minima in the polarization function to develop.

Furthermore, we apply the scattering model to investigate if flakes can explain light scattering features observed in cometary atmospheres. We find that silicate flakes, with some organic content and a thickness, typical of a few layers of interstellar dust grains, show scattering characteristics found for cometary dust, such as positive polarization with a maximum at medium phase angles, positive color and increasing polarimetric color with phase angle.

CHAPTER 1
INTRODUCTION

The presence of highly aspherical particles, such as flakes, may be common in different natural environments (e.g., plate-shaped ice crystals in a cirrus cloud or dust flakes in a cometary atmosphere). The objective of this work is to study the light scattering by flakes of arbitrary refractive index and investigate how flakes may be recognized by the way they scatter light. An efficient method for modeling electromagnetic scattering by a thin dielectric plate, with dimensions of a few wavelengths or larger, is developed and applied to investigate the spatial scattering properties of flakes. The scattering by flakes is also examined using analog-to-light microwave measurements, which in addition, serve to test the validity of the theoretical modeling. The scattering characteristics found for flakes are used to investigate the presence of thin flake-like particles in a cometary atmosphere.

1.1 Background

When a comet enters the inner part of the solar system the formation of flake-like dust may occur. As the volatiles in a cometary nucleus evaporate due to solar irradiation, the dust once imbedded in the ice is released. Dust particles with a sufficiently large surface-to-mass ratio may be carried away by the escaping gas and may contribute to the gaseous dusty atmosphere (the coma) around the comet nucleus. On the other hand, particles with a lower surface-to-mass ratio stay on the surface of the nucleus. As ice sublimates, dust particles may also be trapped in the interstices between the particles already accumulated on the surface. This notion of grain is the basis for the modeling of mantle formation by Rickman et al. (1990). The mantle obstructs the gas flow and shields the ices from direct sunlight, and as a result the thickness of the mantle increases slowly. The mantle may be subject to fragmentation when the underlying gas pressure exceeds the weight of the mantle. In some mantle simulations (Rickman et al., 1990), thin layers of dust are carried away by the gas as soon as the interstices clog up and the gas pressure increases. Gustafson (1990, 1994) suggested that cometary meteoroids and dust may be compacted comet material shaped as thin flakes as a result of mantle fragmentation or blow-offs.

The formation of dust flakes by a comet has also been suggested, based on the dynamics of the Geminid meteoroids during atmospheric flight and of the Geminid meteor stream in space, which indicate that they may be flakes produced during cometary activity on asteroid 3200 Phaethon (Gustafson, 1990; Gustafson et al., 2000). Furthermore, in a laboratory study, Stephens and Gustafson (1991) found that thin flakes can indeed form on surfaces of sublimating dust/ice mixtures.

1.2 Light Scattering by Flakes – a Review

Exact analytical solutions to the problem of the scattering of electromagnetic radiation have only been found for a few highly symmetrical shaped objects; for example, the sphere (Lorenz, 1898; Mie, 1908) and the infinite cylinder (Wait, 1955). These solutions are easily used for numerical computations, and the availability of efficient computer algorithms for the computation of the scattering by spheres (Bohren and Huffman, 1983) has resulted in the widespread practice of treating nonspherical particles as if they were spheres to which the Mie solution is applicable. The modeling of scattering by nonspherical particles using volume- or surface-equivalent spheres may offer a relatively good approximation for the scattering by a collection of randomly oriented particles, whose dimensions in any given direction are similar to the dimensions in other directions. This approach, however, should be taken with caution. Spherical particles can, for example, neither produce well-known optical phenomena such as halos observed for ice crystals (Greenler, 1999), nor produce the polarization observed for interstellar grains aligned by magnetic fields (Spitzer, 1978)

Examples of finite non-spherical particle shapes for which general solutions have been derived are the spheroid (Asano and Yamamoto, 1975) and the perfectly conducting disk (Meixner and Andrejewski, 1950). However, because of the complexity of these solutions, they are not practical for numerical computations. The scattering by asymmetric particles, such as flakes, is therefore often treated with numerical methods and approximations of various kinds. The smaller the particle, the smaller the effect of the particle shape. For particles much smaller than the wavelength, Rayleigh (1897) derived an approximation based on the assumptions that the incident field is approximately uniform over the region occupied by the particle and that the internal field is homogenous. In this case, the scattering is treated as if it was generated from a single dipole and the main influence on the scattering is the polarizability of the particle. The Rayleigh approximation is generally accurate for particles whose largest dimension is smaller than a tenth of the wavelength. On the other hand, scattering by particles that are much larger than the wavelength can, to some extent, be analyzed using the geometric optics approximation. This approximation is generally applicable to the scattering by particles with dimensions of the order of a few hundred wavelengths or larger. However, if interference effects are important, the dimensions may need to be much larger.

Until recently, computations of the scattering by thin flakes of moderate size, i.e., one or a few wavelengths in extent, were limited to the use of low-frequency methods such as the discrete dipole approximation (DDA), also known as the coupled dipole approximation (Purcell and Pennypacker, 1973). The DDA is based on dividing the scatterer into a number N of polarizable units that are treated as dipoles. The field exciting a dipole is a superposition of the incident field and the fields scattered by all other dipoles. A system of N linear equations for N fields and N dipoles can be written. The numerical solution of this system is used to compute the N partial fields scattered by the dipoles and consequently the total scattered field.

A method related to the DDA is the method of moments (MoM) (Harrington, 1968), which is used to solve the integral equation (Van Bladel, 1961) for the scattering by a given object. Here the object is divided into a number of small cubic cells with about 10 to 20 cells per wavelength and it is assumed that the field within each cell is constant. The field within a cell is represented by the sum of the external field and the field induced by all other cells including the cell itself. Once the internal field is obtained, the interior induced current can be found and the scattered field can be computed via the integral equation.

The advantage of DDA and MoM is their applicability to arbitrarily shaped particles. However, their increasing demand on computer memory and time with particle size, makes their use limited to particles of size comparable to the wavelength. Weil and Chu (1976) and Ksienski and Senior (1985) developed MoM solutions specialized for the scattering by thin circular disks with the large dimension comparable to the wavelength. Examples of DDA calculations for flake-like particles are presented in a recent survey by Yanamandra-Fisher and Hanner (1999), where the scattering results for flakes with an aspect ratio of 5 and a large dimension of up to 2.2 wavelengths are included.

Another numerical approach, which generally has been considered a low-frequency solution, is the T-matrix method, also known as the extended boundary condition method (Barber and Yeh, 1975; Waterman, 1965). During the last decade the method has been improved and extended (Mishchenko and Travis, 1994; Wielaard et al., 1997) and recently it was used to compute the scattering by axially symmetric particles with equivalent-sphere size parameters exceeding 100 (Mishchenko and Travis, 1998). In the T-matrix method, the incident and scattered fields are expanded into vector spherical harmonic functions. From the linearity of Maxwell's equations, it follows that the expansion coefficients of the scattered field are linearly related to the expansion coefficients of the incident field. The T (for transition) matrix is the linear transformation connecting the coefficients of the incident field to those of the scattered field. Although the T-matrix method, in principle, can be applied to any particle shape, T-matrix calculations are most efficient for objects that have rotational symmetry. The main advantage of this method is that the elements of the T-matrix are independent of the incident and scattered fields. Thus, the T-matrix only needs to be calculated once and can then be used in computations for any direction of the incident light and scattering. This is an attractive attribute when averages over orientation or particle size distributions are calculated.

In the last decade, T-matrix computations were conducted for flakes in the form of circular disks with larger aspect ratios (Kuik et al., 1994; Mishchenko et al., 1997; Zakharova and Mishchenko, 2001). Most recently, Zakharova and Mishchenko (2001) reported results for disks with aspect ratios up to 20 and surface-equivalent sphere size parameters up to 12. The scattering by flake-like particles was also studied using T-matrix calculations for oblate spheroids (Zakharova and Mishchenko, 2000). To deal with the scattering by larger flake particles, Le Vine et al. (1983, 1985) developed an approximate method for the scattering by disks with a radius much larger than the thickness, based on an extension of the Kirchhoff approximation (Jackson, 1975). The extended principle is to replace the object by a canonical form for which the fields are known and then to use these fields in the original object. In the case of the disk, the internal field is approximated with the field that would exist inside an infinite sheet of the same thickness, orientation and dielectric properties. The internal field is used to find the approximate equivalent source distributions inside the disk and in turn, the scattered field radiated by the equivalent sources, is calculated.

1.3 New Approach for Light Scattering by Thin Flakes

In this work, we develop an approximate method for the scattering by a thin dielectric plate within the framework of geometrical theory of diffraction (GTD) (Keller, 1962), with the intent of obtaining a computationally fast yet accurate method describing the scattering by thin flakes in the size range of a few wavelengths and larger, hence a method suitable to calculate averages over orientation and size distribution. The GTD extends the geometric optics approximation by including diffracted fields. The original scattering problem, which may be difficult to deal with directly, is broken up into simpler boundary value problems, referred to as canonical problems, for which asymptotic solutions can be obtained. The ultimate solution is a superposition of the contributions from each canonical problem. Thus, an important advantage of this approach is that the computational effort does not depend on size. The GTD has been used widely and successfully in a variety of engineering applications involving diffraction at edges with perfectly conducting surfaces. Although it is approximate in nature, the method works well on objects as small as a wavelength in extent (Kouyoumjian, 1975).

To date, there are no canonical GTD solutions for transparent dielectric objects, such as a wedge or a half-plane, which could be used to model dielectric flakes. Approximations have been developed (Burnside and Burgener, 1983; Rouviere et al., 1999) based on the GTD formulations for a perfectly conducting half-plane, which are modified using Fresnel's equations in order to account for the transmitted and reflected fields.

Here, we take a new approach to deal with the scattering by a dielectric flake of finite thickness. In our scattering model, the scattered light is considered a sum of two parts: the external and the transmitted scattered light. The dielectric properties of the flake are taken into account for the externally scattered light by applying an impedance boundary condition (IBC) solution for a half-plane (Volakis, 1986; Senior and Volakis, 1995) to the flake' s edges. A correction is applied to the scattered field in order to compensate for the discrepancy in the reflected field due to the approximate nature of the IBC; this step improves the model for materials with lower refractive indexes. The transmitted field is found by considering the transmitted scattered light from an aperture complementary to the flake. In comparisons with experimental measurements, a good agreement is found when the large dimension of the flake is greater than 6 wavelengths and the aspect ratio of the flake exceeds 25.

The originality of this work consists of (i) a new model for the electromagnetic scattering by a thin dielectric flake; (ii) a large collection of unique microwave scattering measurements of a flake in fixed orientation and measurements averaged over the rotation of the flake; (iii) an extensive set of computer simulations using our scattering model in order to investigate the scattering properties of flake-like particles; (iv) a study of scattering properties that may be used as indicators of flakes in a remote sensing application; (v) a study of the possibility that the light scattering by flakes may be able to explain light scattering properties observed in a cometary atmosphere.

1.4 Conventions and Notation

For consistency and to facilitate comparison with other work, some common conventions and notations are used throughout this dissertation. The size of the scattering object will usually be expressed in units of the wavelength or specified by its size parameter. The size parameter x, is defined as the ratio $2\pi a/\lambda$, where a is a measure of the particle size (e.g., the radius of a sphere) and λ is the wavelength of the light in the surrounding medium. In the case of a nonspherical particle such as the flake, a is often presented as the radius of a sphere with a surface (or volume) equal to the surface (or volume) of the flake, and the size parameter is then referred to as the surface (or volume) -equivalent sphere size parameter. The aspect ratio of a particle here corresponds to the ratio of the maximum and minimum particle dimension. The time dependence of the electromagnetic field maintained throughout the dissertation is chosen to be $\exp(i\omega t)$

and, hence, the dielectric properties are represented by the complex refractive index, $m = n - in'$. If not otherwise specified, plotted intensities are given in units of the scattering matrix using the notation in van de Hulst (1957).

1.5 Outline of the Dissertation

Chapter 2 introduces the geometrical theory of diffraction and reviews related concepts that are used in the theoretical modeling of light scattering by a flake in Chapter 4. Chapter 3 describes the microwave scattering facility and the experimental procedures used in various test measurements. Chapter 4 reviews the impedance boundary condition solution for a half-plane and derives the proposed scattering approximation for a dielectric flake. Chapter 5 examines the validity of the scattering approximation by comparing its predictions to microwave measurements and discusses the limits of this new approach. Chapter 6 presents a comprehensive study of the light scattering properties of a thin dielectric flake, and discusses scattering characteristics that may be used as indicators for flake-like particles. Chapter 7 investigates the possibility of observing flake-like particles in a cometary atmosphere and compares the light scattering properties of flakes to the observations of Comet Hale-Bopp. Chapter 8 offers a summary and conclusions.

CHAPTER 2
GEOMETRICAL THEORY OF DIFFRACTION

In this dissertation the theoretical modeling of light scattering is done within the high-frequency methodology of geometrical theory of diffraction (GTD). The GTD, which originally was introduced by Keller (1962), extends geometrical optics (GO) by taking diffraction into account. This chapter introduces the foundations of GTD and related concepts that are used in subsequent chapters.

Diffraction occurs when a finite object is inserted in the path of an illuminating field. The fundamental premise underlying GTD is that when the scattering object is large in terms of the wavelength, then diffraction, like reflection and refraction, can be treated as a local phenomenon. Diffraction depends primarily on the incident field and the geometry of the object in the immediate neighborhood about the point of diffraction (e.g., a diffracting edge).

The GTD incorporates the contribution of diffracted fields into the ray-oriented framework of GO by introducing diffracted rays. These diffracted rays are produced by incident rays, which hit points on an object that create a discontinuity in the incident GO field. A field is associated with each ray and the total field at a point is the sum of the fields of all rays at that point. The propagation of diffracted rays is determined via a generalization of Fermat's principle (Keller, 1962). From this generalization it follows that the diffracted rays, like the usual rays of geometrical optics, follow paths that make the optical distance from the source to the observation point an extremum, which usually

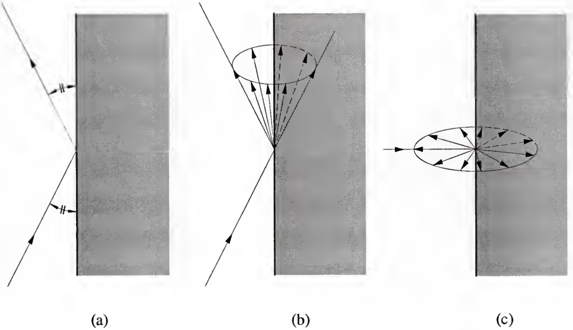

Figure 1: Illustration of diffracted rays; a) ray path with a point on the edge of a thin screen; b) cone of diffracted rays produced by an incident ray that hits the edge of a thin screen obliquely; c) plane of diffracted rays produced by a ray normally incident on the edge of a thin screen.

is a minimum. Thus, in a homogenous medium, an edge-diffracted ray consists of two straight-line paths (Figure 1(a)) that subtend equal angles with the tangent to the edge and are located on opposite sides of the plane normal to the edge at the point of diffraction. This represents the law of edge diffraction and it shows that a ray incident obliquely onto an edge gives rise to a cone of diffracted rays (Figure 1(b) and Figure 1(c)). Furthermore, the laws of GO also apply to the field along the diffracted rays, i.e., (i) the amplitude of the diffracted field varies in accordance of the conservation of energy in a tube of rays, and (ii) the phase of the field along the ray is equal to the product of the wave number of the medium and the distance from some reference point.

The initial value of the field on a diffracted ray is determined from the incident field with the aid of an appropriate diffraction coefficient. The diffraction coefficients are usually based on an asymptotic evaluation of known solutions to Maxwell's equations for simple (canonical) boundary value problems. The asymptotic solution is typically a series of inverse powers of the wave number k, of which only the first term usually is retained. At sufficiently high frequencies the asymptotic representation may be interpreted as a ray description of the diffracted field, which enables the direct extraction of the diffraction coefficients. With the diffraction coefficients and the laws of GO, the field diffracted by an edge may be written on the form

$$\mathbf{E}^d(s) = \mathbf{E}^i(Q) \cdot \overline{\mathbf{D}}(Q) \frac{e^{-jks}}{\sqrt{s}} \tag{2- 1}$$

where s is the distance along the diffracted ray, $\mathbf{E}^i(Q)$ is the incident field at the edge and $\overline{\mathbf{D}}$ is the dyadic diffraction coefficient.

As the diffraction is treated as originating from distinct regions, the scattering object can be resolved into smaller components, each locally representing a canonical problem. The final GTD solution is a superposition of the contributions from each component. Hence, an obvious benefit of GTD is that the computations are independent of the size of the diffracting body. Furthermore, since the diffraction coefficients are based on an asymptotic expansion of the wave number, k, it is also evident that the accuracy of the description offered by GTD is improved with increasing frequency. This is equivalent to GTD giving a more accurate representation of the diffracted field as the dimensions of the object are increased with respect to the wavelength of interest. It is also apparent that the farther apart the different diffracting components are, the more correct it is to treat them independently.

In Section 2.1, the diffraction coefficients for a perfectly conducting edge are presented. Both Keller's (1962) original diffraction coefficients and the uniform diffraction coefficients (Kouyoumjian and Pathak, 1974) are given and their differences are discussed. These diffraction coefficients have been widely and successfully employed in a variety of engineering applications involving diffraction at edges with perfectly conducting surfaces.

Although GTD is approximate in nature, the method works well on objects as small as a wavelength in extent (Kouyoumjian, 1975). However, when the scattering object is small and its edges are close to each other, the contribution from multiply diffracted fields may become important. This interaction between edges is further discussed is Section 2.2.

In the modeling of electromagnetic scattering from flakes with dielectric surfaces, the material properties can be taken into account by using impedance boundary conditions (IBC's). These approximate boundary conditions are derived in Section 2.3, in order to facilitate the discussion of the validity and limitations of our scattering model in Chapter 4.

The last section introduces the concept of equivalent currents, which is a technique where the edges are replaced by equivalent currents in order to model the scattering by edges of finite extent.

2.1 Edge Diffraction

When a plane wave is incident on a semi-infinite conducting plane (Figure 2), the fields represented by geometrical optics (GO) can be separated into three different field regions in the space surrounding the edge. The regions are separated by discontinuities in the GO field, referred to as the incident and reflection shadow boundary, respectively

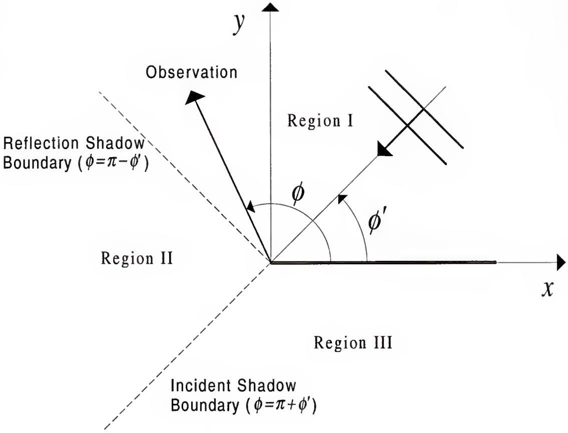

Figure 2: Plane wave incident on a conducting half-plane. Regions I, II and III are separated by the reflection shadow boundary, incident shadow boundary and the half-plane.

(Figure 2). With the angle of diffraction ϕ and the angle of incidence ϕ' defined in Figure 2, the three regions are described as follows: Region I: $0 < \phi < \pi-\phi'$; Region II: $\pi-\phi' < \phi < \pi+\phi'$; Region III: $\pi+\phi' < \phi < n\pi$. These regions are illustrated in Figure 3a and Figure 4a, which show the amplitude and the real part, respectively, of the GO field, when a unit amplitude, perpendicular polarized plane wave is incident at 45 degrees upon a half-plane. In Region I both the incident and the reflected GO fields contribute and the resulting interference can be seen in Figure 4a. In Region II only the incident GO field contributes and no GO field is present in Region III. To remove the discontinuities along the shadow and reflection boundary, the diffracted field needs to be taken into account.

The remainder of this section presents the GTD treatment of the diffracted field by a perfectly conducting edge, and compares the original diffraction coefficients developed by Keller (1962) with the uniform diffraction coefficients, subsequently derived by Kouyoumjian and Pathak (1974).

The classic electromagnetic boundary conditions for a perfect conductor involve the unit vector normal to the interface, but at a surface singularity such as an edge no unique normal can be defined. Thus instead of analytical expressions, asymptotic solutions need to be used. In case of the scattering by an edge, the asymptotic solution for the canonical scattering problem of a wedge (Figure 5) can be used. The GTD solution for a wedge is formalized by taking the asymptotic expression and deducing diffraction coefficients D, which relate the diffracted field E^d to the incident field E^i at the diffracting edge Q (Figure 5). When the illuminating field E^i is a plane wave incident normal the edge the diffracted field E^d can be written as

$$E^d(\rho,\phi)= E^i(Q)D(\rho,\phi,\phi',n)\frac{e^{-jk\rho}}{\sqrt{\rho}} \qquad (2\text{-}\ 2)$$

where ρ and ϕ are the polar coordinates of the observation point, ϕ' is the angle of incidence (Figure 5) and k is the wave number. Furthermore, $e^{-jk\rho}$ is the phase factor and $1/\sqrt{\rho}$ is the spatial attenuation factor. The included angle of the wedge is characterized by the parameter n. As the plane wave is normally incident to the edge and the wedge at this point is considered to be infinite in extent this is essentially a two-dimensional scattering problem and the diffracted field is described by a cylindrical wave.

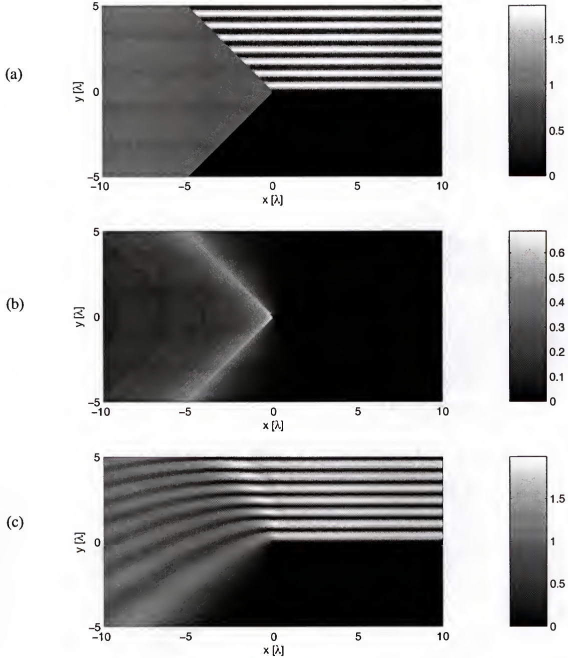

Figure 3: Amplitude of the geometrical optics field (a), the diffracted field (b), and the total field (c). It can be seen that when the geometrical optics field and diffracted field are combined, the amplitude of the total field has a smooth transition as the shadow and reflection boundaries are crossed.

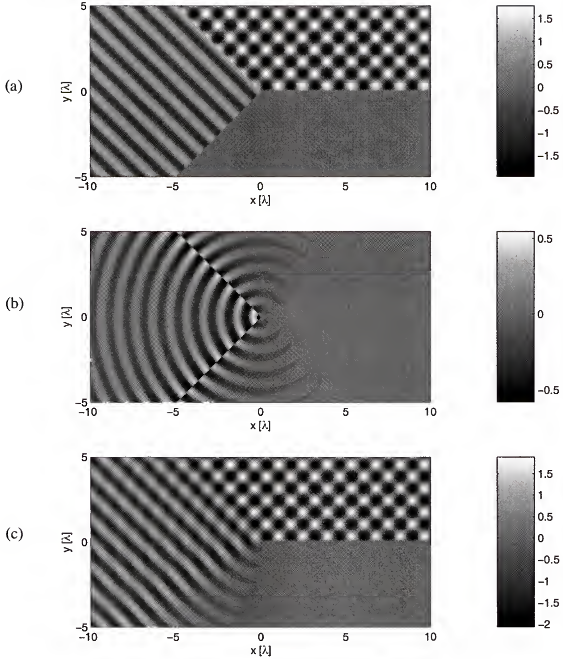

Figure 4: Real part of the geometrical optics field (a), the diffracted field (b), and the total field (b). It can be seen that when the geometrical optics field and diffracted field are combined, the real part of the total field has a smooth transition as the shadow and reflection boundaries are crossed.

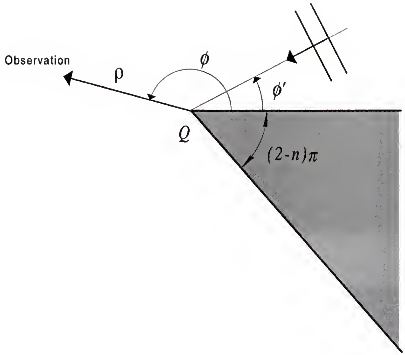

Figure 5: Plane wave incident on a wedge.

Here follows a brief outline for the derivation of the diffraction coefficients for a wedge. For a more detailed description the reader is referred to Balanis (1989) and Kouyoumjian and Pathak (1974). An analytical solution for the scattering by a perfectly conducting wedge may be obtained on the form of an infinite eigenfunction series in terms of $k\rho$, by the method of Green's functions. However due to the slow convergence of the Bessel and Hankel functions involved in the eigenfunction series, a high-frequency asymptotic expansion in inverse powers of $k\rho$ is advantageous. In order to achieve this, the Bessel and Hankel functions are replaced by their integral representations and the series are then summed leaving the integral representations. Ultimately the integrals are asymptotically evaluated. It is in the asymptotic evaluation wherein lies the difference between Keller's diffraction coefficients and the uniform ones. Whereas Keller used the conventional method of steepest descent (Balanis, 1989) to derive an asymptotic expression, Kouyoumjian and Pathak, (1974) employed the Pauli-Clemmow modified method of steepest descent (Felsen and Marcuvitz, 1973). The main difference between the two methods is that the solution provided by the Pauli-Clemmow modified method of steepest descent has an additional discontinuous function that compensates for the singularity present along the corresponding shadow and reflection boundary when the conventional steepest descent method is used. The additional function is referred to as the transition function and it is proportional to the Fresnel integral. The development of the uniform diffraction coefficients is generally referred to as the uniform theory of diffraction (UTD).

After the asymptotic evaluation of the eigenfunction series describing the scattering by the perfectly conducting wedge, four distinct parts may be identified. The first two terms can be identified with the incident and reflected GO fields. The other two terms may be written on the form of equation (2- 2) and may be viewed as the incident and reflected diffracted fields, respectively. This denomination of the diffracted field comes from that the term representing the incident diffracted field is more dominant near the shadow boundary, whereas the term representing the reflected diffracted field is more dominant near the reflection boundary (Balanis, 1989).

If the observation point is not close to a shadow or reflection boundary and $\phi \neq 0$ or $n\pi$, Keller's original diffraction coefficients (Keller, 1962) can be used. With the incident field being a plane wave these coefficients are written as

$$D_{\perp,//}(\phi,\phi',n)=\frac{e^{-j\pi/4}\frac{1}{n}sin\left(\frac{\pi}{n}\right)}{\sqrt{2\pi k}} \times\left[\frac{1}{cos\left(\frac{\pi}{n}\right)-cos\left(\frac{\phi-\phi'}{n}\right)}\pm\frac{1}{cos\left(\frac{\pi}{n}\right)-cos\left(\frac{\phi+\phi'}{n}\right)}\right] \tag{2- 3}$$

where the minus sign is used for perpendicular polarization and the plus sign for parallel polarization. Here, the first term within the brackets is the part associated with the incident diffracted field while the second term is the part associated with reflected diffracted field. However, as the incident or shadow boundary is approached, this expression for the diffraction coefficients becomes singular. To avoid this problem, Kouyoumjian and Pathak's (1974) uniform diffraction coefficients, which are valid at all points away from the edge, should be used. The expressions for the uniform diffraction coefficients are

$$\begin{aligned} D_{\perp,//}(\rho,\phi,\phi',n)&=\frac{e^{-j\pi/4}}{2n\sqrt{2\pi k}} \\ &\times\left[\left\{cot\left(\frac{\pi+(\phi-\phi')}{2n}\right)F\left[kLg^{+}(\phi-\phi')\right]+cot\left(\frac{\pi-(\phi-\phi')}{2n}\right)F\left[kLg^{-}(\phi-\phi')\right]\right\}\right. \\ &\left.\pm\left\{cot\left(\frac{\pi+(\phi+\phi')}{2n}\right)F\left[kLg^{+}(\phi+\phi')\right]+cot\left(\frac{\pi-(\phi+\phi')}{2n}\right)F\left[kLg^{-}(\phi+\phi')\right]\right\}\right] \end{aligned} \tag{2- 4}$$

where again the minus sign is used for perpendicular polarization and the plus sign for parallel polarization. The function *F(X)* is the transition function and it involves a Fresnel integral,

$$F(X)=2j\left|\sqrt{X}\right|e^{jX}\int_{\sqrt{X}}^{\infty}e^{-j\tau^{2}}d\tau \tag{2- 5}$$

Asymptotic expressions for the transition function *F(X)* are for small *X*

$$F(X)=\left[\sqrt{\pi X}-2Xe^{j\pi/4}-\frac{2}{3}X^2e^{-j\pi/4}\right]e^{j(\pi/4+X)} \qquad X<0.3 \qquad (2\text{-}\ 6)$$

and for large *X*

$$F(X)=\left[1+j\frac{1}{2X}-\frac{3}{4}\frac{1}{X^2}-j\frac{15}{8}\frac{1}{X^3}+\frac{75}{16}\frac{1}{X^4}\right] \qquad X>5.5 \qquad (2\text{-}\ 7)$$

Throughout this dissertation we will use an algorithm for the transition function, which applies these asymptotic expressions when suitable, and for intermediate values (0.3 < *X* < 5.5) a linear interpolation scheme from Balanis (1989) is used. In Figure 6, the magnitude and phase of the transition function are plotted. It can be seen that

$$\left.\begin{array}{l}|F(X)|\leq 1\\ 0\leq \text{Phase of } F(X)\leq 45\,\text{deg.}\end{array}\right\} \quad 0.001\leq X\leq 10$$

$$F(X)\cong 1 \qquad X>10 \qquad (2\text{-}\ 8)$$

If the argument *X* of the transition function is greater than 10, it can be replaced by unity and the uniform diffraction coefficients reduce to Keller's original diffraction coefficients in equation (2- 3).

In the argument of the transition function $X=kLg^{\pm}(\phi\pm\phi')$, *k* is the wave number, *L* is the so-called distance parameter (further discussed below), and $g^{\pm}$ is a measure of the angular separation between the field point and a shadow or reflection boundary. The expression for $g^{\pm}$ is

$$g^{\pm}(\phi\pm\phi')=2\cos\left(\frac{2n\pi N^{\pm}-(\phi\pm\phi')}{2}\right) \qquad (2\text{-}\ 9)$$

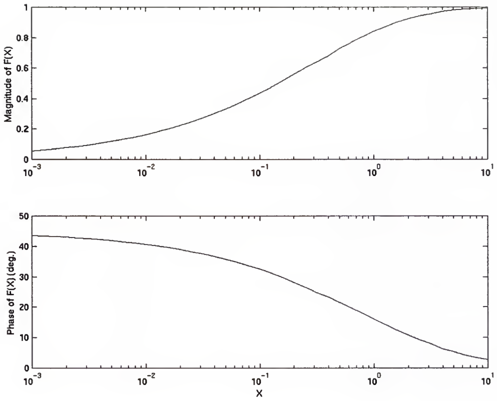

Figure 6: The magnitude and phase of transition function *F*(*X*).

where $N^{\pm}$ are the integers which most closely satisfy the equations

$$\begin{aligned} 2n\pi N^{+} - (\phi \pm \phi') &= \pi \\ 2n\pi N^{-} - (\phi \pm \phi') &= -\pi \end{aligned} \tag{2- 10}$$

The distance parameter *L* depends on the type of illumination. For plane wave illumination, $L = \rho$, which represents the distance from the edge to the observation point (Figure 5). According to the principle of reciprocity, equation (2- 4) also can be used for a cylindrical wave incident upon the same wedge and the observation made at very large distance, in the far field. In this case, however, $L = \rho'$ which represents the distance from the edge to the source of the cylindrical wave. If both the source and observation point are located at finite distances from the edge, represented by ρ and ρ', respectively, then L takes the form

$$L = \frac{\rho\rho'}{\rho+\rho'} \begin{cases} \overset{\rho'\to\infty}{\cong \rho} \\ \overset{\rho\to\infty}{\cong \rho'} \end{cases} \tag{2- 11}$$

At a shadow or reflection boundary one of the cotangent functions in the expression for D, given in equation (2- 4), becomes singular, while the other three remain bounded. However, even though the cotangent becomes singular, its product with the transition function is bounded.

For a unit amplitude, perpendicularly polarized plane wave incident at $\phi' = 45$ degrees onto a conducting half-plane, the real part and the amplitude of diffracted fields are shown in Figure 3b and Figure 4b, respectively. Here the diffracted field has been calculated employing the uniform diffraction coefficients. The amplitude along the shadow and reflection boundaries is 0.5, and in Figure 4b it is seen how the diffracted field is a cylindrical wave originating at the edge and that the phase undergoes a 180 degrees phase reversal as the boundaries are crossed. The discontinuities of the diffracted field compensate for the discontinuities in the GO field. When added together, the total field has a smooth transition as the shadow and reflection boundaries are crossed (Figure 3c and Figure 4c). The addition of the diffracted fields does, however, not only remove the discontinuities of the GO field, but the GO field is modified in all space. In particular, it can be seen that there is a scattered field present in the shadow region.

As an example, the intensity of the scattered light by a half-plane illuminated by a plane wave (Figure 7) is calculated using the uniform diffraction coefficients. The result is compared to microwave measurements of the scattering by a 0.15 λ thin brass sheet

(Figure 8). Except at scattering angles about –90 degrees, where the holder of the brass sheet obstructs the scattered microwaves, a good agreement between the UTD calculations and experiment is found.

Grazing incidence, where $\phi' = 0$ or $\phi' = n\pi$, must be considered separately. In this case $D_\perp = 0$, as the perpendicular polarization vanish along the surface, and the expression for $D_{/\!/}$ is multiplied by ½. The need for the factor ½ may be seen by considering grazing incidence to be the limiting situation, where the incidence and reflected fields merge, so that one half the total field propagating along the face of the wedge toward the edge is the incident field and the other half is the reflected field.

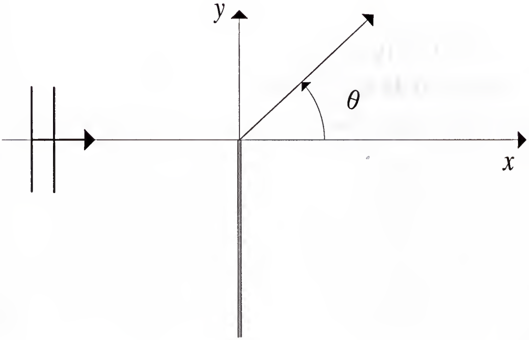

Figure 7: Plane wave normally incident on a half-plane. Angle θ denotes the scattering angle.

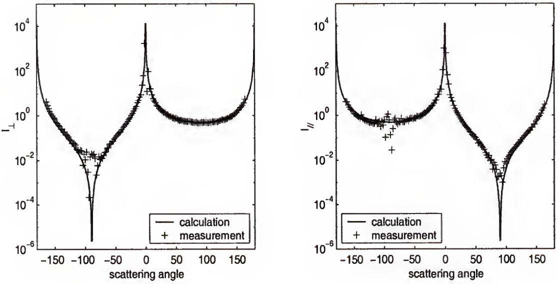

(a) (b)

Figure 8: Microwave measurements (crosses) compared with UTD calculations (solid line) of the light diffracted by a half-plane when illuminated by a plane wave at normal incidence; a) perpendicular polarization; a) parallel polarization.

2.2 Multiple Diffracted Fields

When an object consists of multiple edges, as most objects do in practice (e.g., a rectangular slab) a coupling between the edges will take place (Balanis, 1989). This interaction is more important if the separation between the edges is small. In order to illustrate multiple diffraction we refer to Figure 9, where a structure with two edges is illuminated by a plane wave. In Figure 9 the diffraction described by a, b and c correspond to first, second and third order diffraction at wedge 1. The first order of diffracted light by wedge 1 (Figure 9a) is the light diffracted as the incident plane wave illuminate wedge 1. The second order diffraction by wedge 1, is the light diffracted as the first order of diffracted light from wedge 2 illuminates wedge 1 (Figure 9b). In turn, third and higher order diffractions by wedge 1 (Figure 9c) are due to the illumination by second and higher order diffractions, respectively, from wedge 2. Second and higher order diffractions are usually all referred to as higher order diffractions.

The procedure for calculating second and higher order diffractions is the same as for first order diffraction. It is evident, however, that accounting for higher order of diffractions can become very laborious. In this thesis the computation of multiple diffractions is carried out using a technique known as the self-consistent method (Twersky, 1962), which takes all orders of multiple diffractions into account. Using the description of this method in Balanis (1989) we outline the method below.

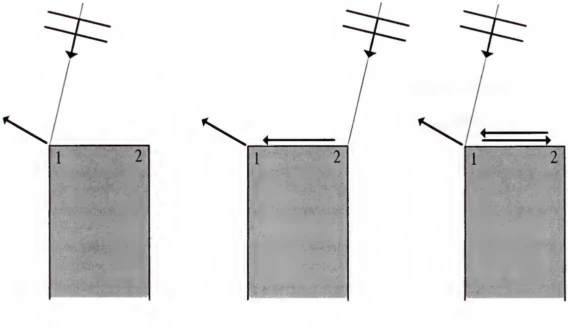

(a) (b) (c)

Figure 9: Illustration of multiple diffractions. Figures a, b and c show first, second and third order diffraction, respectively, at wedge 1.

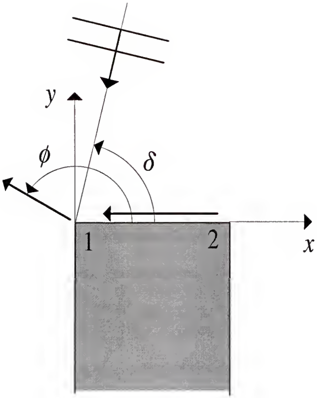

Figure 10: Illustration of the self-consistent method for multiple diffractions.

The self-consistent method treats each diffracting edge as excited by the incoming wave plus the total (initially unknown) field diffracted by its adjacent edges. Thus, the diffracted light by wedge 1 of the structure pictured in Figure 10, is written as a sum of (i) the field diffracted due to the illuminating plane wave radiation E_0, and (ii) the light diffracted due to all orders of diffracted light incident from wedge 2, E_2. Hence, the total diffracted field from wedge 1, E_1 can be written as

$$\begin{aligned} E_1(\rho_1,\phi) &= E_0(Q_1)\left[D_{10}(L_{10},\phi,\delta)\frac{e^{-jk\rho_1}}{\sqrt{\rho_1}}\right] \\ &+ E_2\left(\rho_2 = d,\phi = \frac{3\pi}{2}\right)\left[\frac{1}{2}D_{12}(L_{12},\phi,0)\frac{e^{-jk\rho_1}}{\sqrt{\rho_1}}\right] \end{aligned} \qquad (2\text{- }12)$$

where δ and ϕ are the angle of incidence and angle of diffraction as defined in Figure 10. As the expressions for perpendicular and parallel polarization are identical the subscripts $\perp$ and // have been dropped. Here the first subscript refers to the diffracting edge (1 or 2) and the second subscript refers to the incident field (0, 1 or 2 representing the original incident wave and the diffracted field from wedge 1 and 2, respectively). Further, the expressions for the diffraction coefficient D are found in Section 2.1. Analogously, the total diffracted field from wedge 2, E_2 can be written as

$$\begin{aligned} E_2(\rho_2,\phi) = {} & E_0(Q_2)\left[D_{20}\left(L_{20}, \phi+\frac{\pi}{2}, \delta+\frac{\pi}{2} \right) \frac{e^{-jk\rho_2}}{\sqrt{\rho_2}} \right] \\ & + E_1(\rho_1 = d, \phi = 0)\left[\frac{1}{2} D_{21}\left(L_{21}, \phi+\frac{\pi}{2}, \frac{3\pi}{2} \right) \frac{e^{-jk\rho_2}}{\sqrt{\rho_2}} \right] \end{aligned} \tag{2- 13}$$

In equations (2- 12) and (2- 13), $E_1\,(\rho_1 = d\,, \phi = 0)$ and $E_2\,(\rho_2 = d,\ \phi = 3\pi/2)$ are unknown. However, they can be found through the following procedure. At the position of wedge 2 the total diffracted field by wedge 1, $E_1\,(\rho_1 = d,\ \phi = 0)$, can be obtained from equation (2- 12), and written a

$$\begin{aligned} E_1(\rho_1 = d, \phi = 0) = {} & E_0(Q_1)\left[D_{10}(L_{10}, 0, \delta) \frac{e^{-jkd}}{\sqrt{d}} \right] \\ & + E_2\left(\rho_2 = d, \phi = \frac{3\pi}{2} \right)\left[\frac{1}{2} D_{12}(L_{12}, 0, 0) \frac{e^{-jkd}}{\sqrt{d}} \right] \end{aligned} \tag{2- 14}$$

and at the position of wedge 1 the total diffracted field by wedge 2, $E_2\,(\rho_2 = d,\ \phi = 3\pi/2)$, as given by equation (2- 13), can be reduced to

$$\begin{aligned} E_2\left(\rho_2 = d, \phi = \frac{3\pi}{2} \right) = {} & E_0(Q_2)\left[D_{20}\left(L_{20}, \frac{3\pi}{2}, \delta+\frac{\pi}{2} \right) \frac{e^{-jkd}}{\sqrt{d}} \right] \\ & + E_1(\rho_1 = d, \phi = 0)\left[\frac{1}{2} D_{21}\left(L_{21}, \frac{3\pi}{2}, \frac{3\pi}{2} \right) \frac{e^{-jkd}}{\sqrt{d}} \right] \end{aligned} \tag{2- 15}$$

In a simplified form, equations (2- 14) and (2- 15) can be rewritten as

$$\begin{aligned} E_1(\rho_1 = d, \phi = 0) &= E_0(Q_1)T_{10} + E_2\left(\rho_2 = d, \phi = \frac{3\pi}{2}\right)R_{12} \\ E_2\left(\rho_2 = d, \phi = \frac{3\pi}{2}\right) &= E_0(Q_2)T_{20} + E_1(\rho_1 = d, \phi = 0)R_{21} \end{aligned} \qquad (2\text{- }16)$$

where

$$\begin{aligned} T_{10} &= \left[D_{10}(L_{10}, 0, \delta)\frac{e^{-jkd}}{\sqrt{d}} \right] \\ R_{12} &= \left[\frac{1}{2}D_{12}(L_{12}, 0, 0)\frac{e^{-jkd}}{\sqrt{d}} \right] \\ T_{20} &= \left[D_{20}\left(L_{20}, \frac{3\pi}{2}, \delta + \frac{\pi}{2} \right)\frac{e^{-jkd}}{\sqrt{d}} \right] \\ R_{21} &= \left[\frac{1}{2}D_{21}\left(L_{21}, \frac{3\pi}{2}, \frac{3\pi}{2} \right)\frac{e^{-jkd}}{\sqrt{d}} \right] \end{aligned} \qquad (2\text{- }17)$$

which in turn can be written in matrix form as

$$\begin{pmatrix} 1 & -R_{12} \\ -R_{21} & 1 \end{pmatrix} \begin{pmatrix} E_1(\rho_1 = d, \phi = 0) \\ E_2(\rho_2 = d, \phi = 3\pi/2) \end{pmatrix} = \begin{pmatrix} E_0(Q_1)T_{10} \\ E_0(Q_2)T_{20} \end{pmatrix} \qquad (2\text{- }18)$$

Subsequently, the system of linear equations in (2- 18) can be solved for E_1 ($\rho_1 = d, \phi = 0$) and E_2 ($\rho_2 = d, \phi = 3\pi/2$) using standard matrix inversion procedures. That is,

$$\begin{pmatrix} E_1(\rho_1 = d, \phi = 0) \\ E_2(\rho_2 = d, \phi = 3\pi/2) \end{pmatrix} = \begin{pmatrix} 1 & -R_{12} \\ -R_{21} & 1 \end{pmatrix}^{-1} \begin{pmatrix} E_0(Q_1)T_{10} \\ E_0(Q_2)T_{20} \end{pmatrix} \qquad (2\text{- }19)$$

For a problem with a larger number of edges it is straightforward to extend and apply the self-consistent method, however, the system of equations to be solved will increase,- the number of equations will equal the number of possible interactions between different edges. For example, in the case of a strip that may be described by two infinitely thin edges, there are four ways the edges can interact.

To illustrate the effect of taking the coupling between the two edges of a perfectly conducting thin strip into account, we let a plane wave, polarized parallel to the scattering plane, be incident on a 5.5 λ wide strip at a 45° angle to its normal, as shown in Figure 11. The result is shown in Figure 12, where it can be seen how the scattering is mainly affected in the direction tangent to the surface of the strip, i.e., at 45 and -135 degrees scattering angle. When the light is polarized perpendicular to the scattering plane there will be no coupling between the edges of a convex perfectly conducting structure, since the field with this polarization vanish along the surface. Thus, only the case where the incident wave has parallel polarization is shown.

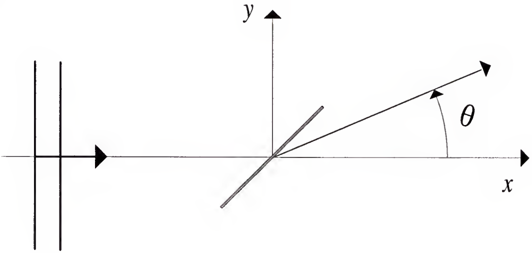

Figure 11: Plane wave incident on a strip at 45° to the normal of its surface. Angle θ is the scattering angle.

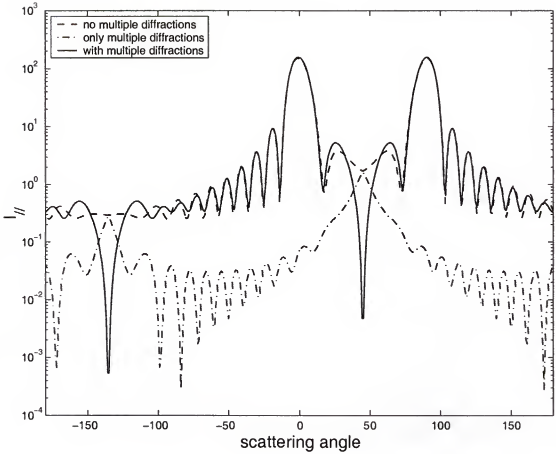

Figure 12: Intensity of the diffracted field by a plane wave, polarized parallel to the scattering plane, incident on a 5.5 λ wide and infinitesimally thin strip. The dashed line shows the intensity when the multiple diffracted fields (dashed-dotted line) are excluded, and solid line shows the intensity when multiple diffractions are taken into account.

In Figure 13 a UTD calculation including multiple diffractions is compared with microwave measurements of the scattering by 5.5 λ wide, 5.5 λ long and 0.15 λ thin brass plate. In the UTD calculation the plate is assumed to be infinitesimally thin. Again the radiation is incident at a 45° angle, as the configuration in Figure 11 shows, and the finite length of the plate is taken into account using the method of equivalent currents, discussed in Section 2.4.

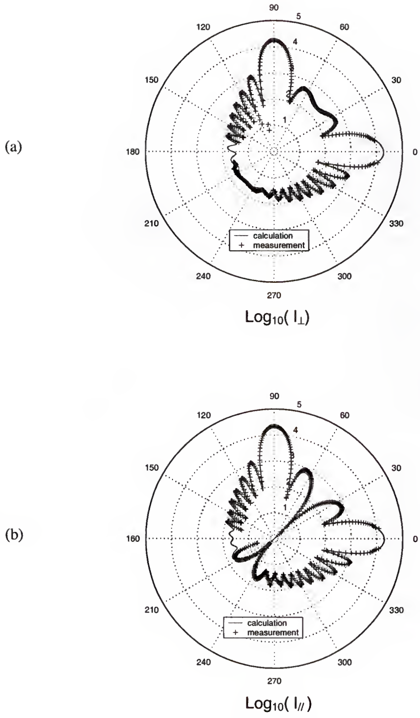

Figure 13: Comparison between UTD calculations (solid line) and microwave measurements (crosses) of the scattering by a 5.5 λ by 5.5 λ and 0.15 λ thick brass plate. In the UTD calculations the plate is assumed to be infinitesimally thin and perfectly conducting; a) perpendicular polarization; b) parallel polarization.

2.3 Impedance Boundary Conditions

At the interface of a perfect conductor the homogeneous Dirichlet and Neumann boundary conditions apply (i.e., the tangential component of the electric field and the normal derivative of the electric field normal to the interface, respectively, vanish at the boundary). Homogeneous boundary conditions allow for asymptotic solutions to be derived for scattering problems such as the perfectly conducting wedge discussed previously in this chapter. If, however, the interface is not perfectly conducting, the boundary value problem becomes more complex, and simplifications in form of approximate boundary conditions are often necessary to make the problem tractable and allow for practical solutions to be developed. Common approximate boundary conditions at the surface of a material of large refractive index are the impedance boundary conditions (IBC's) (Senior, 1960; Senior and Volakis, 1995). The IBCs relate the tangential components of the external electric and magnetic fields by the use of a surface impedance, which is a function of the electromagnetic properties of the material. Hence, as the boundary conditions only involve the exterior fields the IBC's allow for solving explicitly for the scattered fields exterior to the object. Using the derivation by Senior (1960), the IBC's are reviewed below.

Let a dielectric material occupy the half space $y < 0$ (Figure 14). The permittivity and permeability of the material are ε and μ respectively, and thus the complex refractive index m can be written

$$m = \sqrt{\frac{\varepsilon\mu}{\varepsilon_0\mu_0}} \tag{2- 20}$$

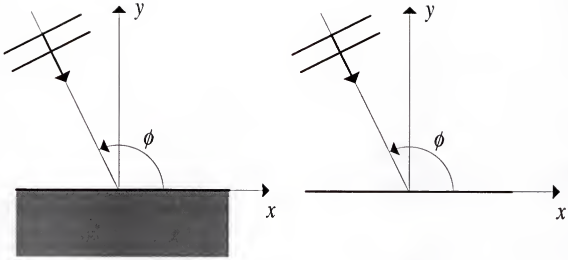

(a) (b)

Figure 14: Dielectric interface (a) and corresponding impedance surface (b).

and the impedance η associated with the surface is

$$\eta = \frac{\mu}{\mu_0 m} \tag{2- 21}$$

The region $y > 0$ is free space in which the source of the electromagnetic field is placed. The field in the half space $y > 0$ is denoted **(E, H)** and in the dielectric medium the field is represented by **(E′, H′)**. Inside the material, the y component of the electric field can be described through the wave equation,

$$\frac{\partial^2 E'_y}{\partial x^2} + \frac{\partial^2 E'_y}{\partial y^2} + \frac{\partial^2 E'_y}{\partial z^2} + m^2 k_0^2 E'_y = 0 \tag{2- 22}$$

where k_0 is the wave propagation constant in free space. If $|m| >> 1$, then E'_y varies rapidly in the y direction, leading to a large value of $\partial^2 E'_y / \partial y^2$ and by comparison the other two derivatives in equation (2- 22) are small. Thus, to the leading order in $|m|$,

$$\frac{\partial^2 E'_y}{\partial y^2} + m^2 k_0^2 E'_y = 0 \tag{2- 23}$$

and the solution that satisfy the radiation condition, i.e., that the field vanish at $y = -\infty$, is

$$E'_y(y) = E'_{y0} e^{jk_0 m y} \tag{2- 24}$$

whose derivative with respect to y is

$$\frac{\partial E'_y}{\partial y} = jk_0 m E'_{y0} e^{jmk_0 y} = jk_0 m E'_y \tag{2- 25}$$

At the interface $y = 0$, the exact boundary conditions are

$$E_y = \frac{\varepsilon}{\varepsilon_0} E'_y \tag{2- 26}$$

and

$$\frac{\partial E_y}{\partial y} = \frac{\partial E'_y}{\partial y} \tag{2- 27}$$

Hence, with boundary condition (2- 26) equation (2- 25) can be expressed

$$\frac{\partial E'_y}{\partial y} = jk_0 m \frac{\varepsilon_0}{\varepsilon} E_y = jk_0 \eta E_y \tag{2- 28}$$

at $y = 0$. Furthermore, using boundary condition (2- 27), equation (2- 28) can be written as

$$\frac{\partial E_y}{\partial y} - jk_0 \eta E_y = 0 \tag{2- 29}$$

A similar analysis can be carried out for the normal component of the magnetic field. However, from the duality of electromagnetic fields, the following relation for the magnetic field at the interface can be written down directly

$$\frac{\partial H_y}{\partial y} - jk_0 \frac{1}{\eta} H_y = 0 \tag{2- 30}$$

These first order IBCs can be written in the more commonly used form by applying Maxwell's equations, which leads to

$$\frac{\partial E_x}{\partial x} - \eta\left(\frac{\partial H_z}{\partial x} - \frac{\partial H_x}{\partial z}\right) + \frac{\partial E_z}{\partial z} = 0 \tag{2- 31}$$

so that

$$\frac{\partial}{\partial x}(E_x - \eta H_z) + \frac{\partial}{\partial z}(E_z + \eta H_x) = 0 \tag{2- 32}$$

Similarly, equation (2- 30) can be written

$$\frac{\partial}{\partial z}(E_x - \eta H_z) - \frac{\partial}{\partial z}(E_z + \eta H_x) = 0 \tag{2- 33}$$

and by successively eliminating E_x - ηH_z and E_z + ηH_x between these two equations we arrive at

$$\frac{\partial^2 \Phi}{\partial x^2} + \frac{\partial^2 \Phi}{\partial y^2} = 0 \tag{2- 34}$$

where $\Phi = E_x - \eta H_z$ or $\Phi = E_z + \eta H_x$. The only solution not exponentially large at $x = \pm\infty$ or $z = \pm\infty$ is $\Phi = 0$, from which follows that

$$\begin{aligned} E_x &= \eta H_z \\ E_z &= -\eta H_x \end{aligned} \tag{2- 35}$$

In this form the conditions state that the tangential electric and magnetic fields are related via the impedance η of the surface, as seen by the fields in free space. Note that the impedance of a perfectly conducting surface is zero.

The IBCs in equation (2- 35) can be combined and expressed in vector form, which in turn can be generalized in such a way that it does not explicitly involve the coordinate system. If **n** is the normal vector whose positive direction is outwards with regard to the medium, equation (2- 35) can be rewritten as

$$\mathbf{n}\times\mathbf{E}=\eta\mathbf{n}\times\left(\mathbf{n}\times\mathbf{H}\right) \tag{2- 36}$$

This expression is commonly referred to as the Leontovich boundary condition (Leontovich, 1948).

Using impedance boundary conditions, Maliuzhinets (1959) found a normal incidence solution for a wedge with arbitrary included angle. In our modeling of scattering by thin dielectric slab in Chapter 4 we use a uniform theory of diffraction solution for the scattering by an impedance half-plane by Senior and Volakis (1995)

In order assess the applicability of the IBCs (which are derived assuming $|m|>>1$) to the scattering by an object with a rather low refractive index, we carried out microwave measurements of the scattering by two different dielectric cubes, with refractive indices of 1.62 – *i*0.003 (acrylic) and 2.52 – *i*0.03 (BK7 glass) respectively. These tests were performed with objects of square cross sections, in order to be able to block the transmitted radiation in the forward direction by attaching thin absorbers on the front sides, as shown in Figure 15. In this way, the radiation diffracted by the surfaces in the forward and specular direction could be isolated fairly well. Measurements were performed using commercial microwave absorbers. However, the best results were obtained when aluminum foil was used. In Figure 16 and Figure 17 the results of the experiment are compared to calculations based on an IBC solution by Syed and Volakis (1995). Although the fit is better for the case when the field is polarized perpendicular to

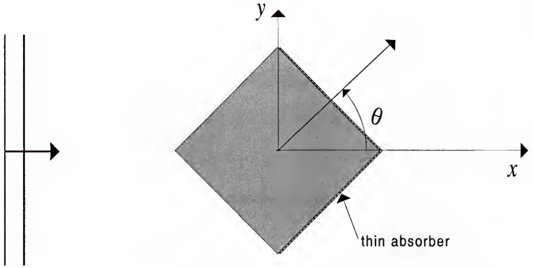

Figure 15: Plane wave incident on a dielectric cube with thin absorbers on the two sides facing the forward direction.

the scattering plane, we see that the intensity of the diffraction in the specular direction agree over all well for both polarizations. For comparison the result from calculations in which the surfaces are assumed to be perfect conductors are also shown (dashed curves).

2.4 Equivalent Currents

In previous sections we were only concerned with diffraction from wedges of infinite length, which can be viewed as a two-dimensional problem due to its independence on the coordinate along the edge. The concept of equivalent currents is a technique, which is used to model the diffraction from a wedge of finite length. The diffracting wedge is with this procedure replaced by a line source in which the equivalent current is adjusted so that the field radiated is equal to the diffracted field from the wedge. If the illumination is polarized perpendicular to the scattering plane the wedge is replaced by an electric line source of equivalent electric current I^e. On the other hand, if

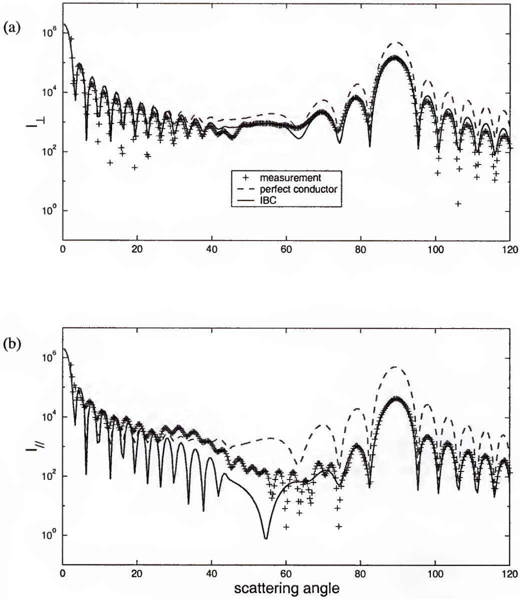

Figure 16: Scattering by a cube with 12.7 λ wide sides. The microwave measurements (crosses) are for a cube made of BK7 glass with aluminum foil on the two sides facing the forward direction (Figure 15) blocking radiation from being transmitted in the forward direction. The solid line shows calculations based on an IBC solution (Syed and Volakis, 1995), with m=2.52 –i0.03. The dashed line shows the result when the surfaces are assumed to be perfectly conducting. a) perpendicular polarization; b) parallel polarization.

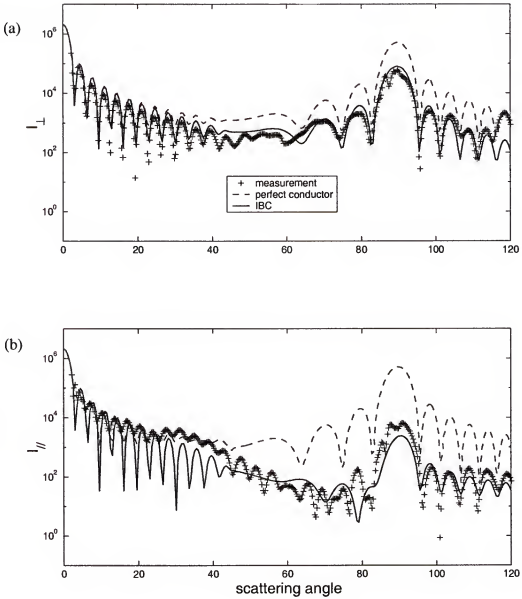

Figure 17: Scattering by a cube with 12.7 λ wide sides. The microwave measurements (crosses) are for a cube made of acrylic with aluminum foil on the two sides facing the forward direction (Figure 15) blocking radiation from being transmitted in the forward direction. The solid line shows calculations based on an IBC solution (Syed and Volakis, 1995), with m=1.62 –i0.003. The dashed line shows the result when the surfaces are assumed to be perfectly conducting. a) perpendicular polarization; b) parallel polarization.

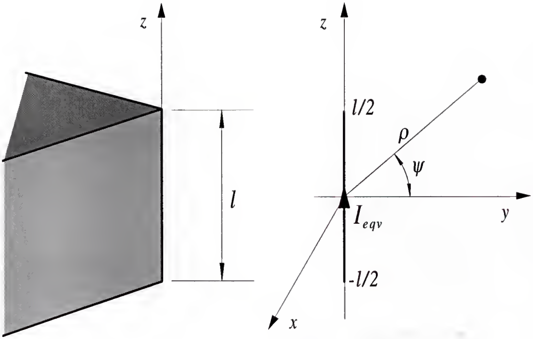

(a) (b)

Figure 18: Diffracting edge (a) and its equivalent current (b).

the illuminating radiation is polarized parallel to the scattering plane the wedge needs to be replaced by a magnetic line source of magnetic current I^m.

The electric field radiated by a two-dimensional electric line source placed along the *z*-axis with a constant current I_z^e is given by Balanis (1989) as

$$E_z = \frac{k^2 I_z^e}{4\omega\varepsilon} H_0^{(2)}(k\rho) \overset{k\rho \to \text{large}}{\cong} -I_z^e \frac{\eta k}{2} \sqrt{\frac{j}{2\pi k}} \frac{e^{-jk\rho}}{\sqrt{\rho}} \tag{2-37}$$

where $H_0^{(2)}(k\rho)$ is the Hankel function of the second kind of zero order. The argument of the Hankel function is the product of the wave number *k* and the distance ρ from the line current. The approximate form is obtained by replacing the Hankel function by it asymptotic formula for large arguments, and is valid in the far field. Using the duality theorem the equivalent expression for the magnetic field radiated by a two-dimensional magnetic line source placed along the *z*-axis with a constant current I_z^m can be obtained as

$$H_z = \frac{k^2 I_z^m}{4\omega\mu} H_0^{(2)}(k\rho) \overset{k\rho \to \text{large}}{\cong} -I_z^m \frac{k}{2\eta}\sqrt{\frac{j}{2\pi k}} \frac{e^{-jk\rho}}{\sqrt{\rho}} \tag{2- 38}$$

The equivalent electric and magnetic currents are determined by equating the expressions (2- 37) and (2- 38), respectively, to the expressions for the field diffracted by a wedge when the incident field has electric and magnetic polarization, respectively. Using the equations (2- 37) and (2- 38) we can write

$$\begin{aligned} E_z^i(Q) D_\perp(\rho,\phi,\phi',n) \frac{e^{-jk\rho}}{\sqrt{\rho}} &= -I_z^e \frac{\eta k}{2}\sqrt{\frac{j}{2\pi k}} \frac{e^{-jk\rho}}{\sqrt{\rho}} \\ H_z^i(Q) D_{//}(\rho,\phi,\phi',n) \frac{e^{-jk\rho}}{\sqrt{\rho}} &= -I_z^m \frac{k}{2\eta}\sqrt{\frac{j}{2\pi k}} \frac{e^{-jk\rho}}{\sqrt{\rho}} \end{aligned} \tag{2- 39}$$

where $E^i_z(Q)$ is the incident electric field (perpendicular polarization) and $H^i_z(Q)$ is the incident magnetic field (parallel polarization) at the diffracting edge. Further, the diffraction coefficients $D_\perp$ and $D_{//}$ are defined in Section 2.1. Solving for I_z^e and I_z^m respectively, leads to

$$\begin{aligned} I_z^e &= \frac{\sqrt{8\pi k}}{\eta k} e^{-j\pi/4} E_z^i(Q) D_\perp(\rho,\phi,\phi',n) \\ I_z^m &= \frac{\eta\sqrt{8\pi k}}{k} e^{-j\pi/4} H_z^i(Q) D_{//}(\rho,\phi,\phi',n) \end{aligned} \tag{2- 40}$$

Considering a wedge with finite length *l*, its equivalent current will also be of finite length *l* (Figure 18). The far-zone electric and magnetic field radiated by the equivalent electric and magnetic line source respectively, of length l, can be found from the expression for the scattering by a finite length dipole (Balanis, 1982) and written

$$\begin{aligned} E_\phi &= j\eta \frac{ke^{-jk\rho}}{4\pi\rho} \cos\psi \int_{-l/2}^{l/2} I_z^e(z') e^{jkz'\sin\psi} dz' \\ H_\phi &= j \frac{ke^{-jk\rho}}{4\pi\eta\rho} \cos\psi \int_{-l/2}^{l/2} I_z^m(z') e^{jkz'\sin\psi} dz' \end{aligned} \tag{2- 41}$$

For a constant equivalent current the integrals in equation (2- 41) reduce to the sinc function, and with equation (2- 40) the far-zone electric and magnetic fields can be written as

$$\begin{aligned} E_\phi &= j \frac{e^{-j\pi/4}}{\sqrt{2\pi}} l\sqrt{k} \cos\psi \frac{\sin(kl\sin\psi)}{kl\sin\psi} E_z^i D_\perp \frac{e^{-jk\rho}}{\rho} \\ H_\phi &= j \frac{e^{-j\pi/4}}{\sqrt{2\pi}} l\sqrt{k} \cos\psi \frac{\sin(kl\sin\psi)}{kl\sin\psi} H_z^i D_{//} \frac{e^{-jk\rho}}{\rho} \end{aligned} \tag{2- 42}$$

When the scattering plane is normal to the scattering edge, $\psi = 0$ and using the forms used in Section 2.1 equation (2- 42) reduces to

$$\mathbf{E}^d(\rho,\phi) = j \frac{e^{-j\pi/4}}{\sqrt{2\pi}} l\sqrt{k} \mathbf{E}^i(Q) \overline{\mathbf{D}}(\rho,\phi,\phi',n) \frac{e^{-jk\rho}}{\rho} \tag{2- 43}$$

where

$$\overline{\mathbf{D}} = \begin{bmatrix} D_\perp & 0 \\ 0 & D_{//} \end{bmatrix}$$

The expression in equation (2- 43) is applied in our scattering model in order to take the finite length of the flake into account.

CHAPTER 3
LABORATORY MICROWAVE SCATTERING MEASUREMENTS

In order to test our scattering approximation, we have experimentally determined the scattering from a number of test objects using the microwave scattering facility at the University of Florida. This chapter introduces the analog-to-light microwave scattering technique and describes the scattering facility as well as the procedures followed in the laboratory measurements.

3.1 Analog-to-Light Microwave Scattering Technique

Experimental measurements of the scattered electromagnetic radiation from a known target illuminated by a known source are important when testing a new scattering model and its range of validity. In our experimental investigation we use the analog-to-light microwave scattering technique. This technique has the great benefit that studying the scattered light by single particles, of any shape and orientation, is relatively easy compared to, for example, laser scattering experiments. The difficulty of characterizing the scattering body on the scale of the wavelength make scattering experiments using visual light demanding. If, however, we take advantage of the fact that in the scattering problem, the dimensions are only encountered as a ratio to the wavelength, we can scale the problem as long as we keep this ratio constant and the material properties are retained. This is known as the *principle of electromagnetic similitude*, which is illustrated using Maxwell's equations in the appendix, following Stratton (1941). Thus, by using microwaves, the light scattering experiment is scaled by a factor 10^4 to 10^5, and the scattering object can be machined and controlled to a much higher accuracy relative to the wavelength.

3.2 Microwave Scattering Facility

The microwave scattering facility is part of the Laboratory for Astrophysics at the University of Florida (Gustafson, 1996). Here, the idealized conditions of electromagnetic scattering that are commonly assumed in theoretical modeling are pursued. The incident light is monochromatic and has a flat wave front to simulate the source of illumination at infinity. The recorded scattered light is that seen by a distant observer, i.e. the *far field*. The facility is a broadband scattering laboratory, which uses the w-band from 75 GHz to 110 GHz (or equivalently 2.7 mm to 4 mm wavelength). This range corresponds to the visual spectrum shifted by a factor of approximately 10^4 toward longer wavelengths.

The transmitting antenna (the source of illumination), seen to the right in the schematic drawings of the microwave facility in Figure 19 and Figure 20, is fixed, whereas the receiving antenna (the detector), mounted on a mobile scattering arm, sweeps an arc in the horizontal plane about the scattering object. The scattering object is positioned, e.g. on a rigid platform, as seen in Figure 20, midway between the two antennas at the intersection of the pointing vectors of the incident beam and the detected scattered light, respectively. The angle between the directions of propagation of the incident light and of the scattered light is the scattering angle. The receiving antenna can be positioned at any scattering angle from 0 degrees (forward scattering) to 168 degrees, prevented to reach higher angles due to the physical dimensions of the two antennas.

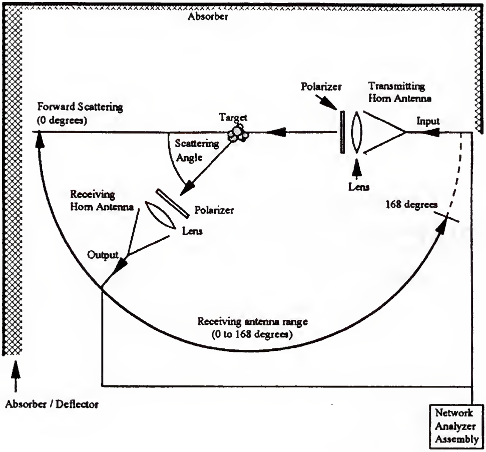
Absorber
Polarizer
Transmitting Horn Antenna
Forward Scattering (0 degrees)
Target
Input
Scattering Angle
Lens
Receiving Horn Antenna
Polarizer
Lens
168 degrees
Output
Receiving antenna range (0 to 168 degrees)
Absorber / Deflector
Network Analyzer Assembly

Figure 19: Schematic drawing of the microwave scattering facility seen from above (Gustafson, 1996). The target and the transmitting and receiving antennas are in the same plane – defining the scattering plane in the laboratory. The transmitting antenna is fixed while the receiving antenna is mounted on a mobile scattering arm. Both antenna assemblies are identical with conical horns fitted with collimating Fresnel lenses and grid polarizing filters. The walls of the scattering chamber are coated with microwave absorbing material and obliquely mounted absorbers deflect the reflection of the forward beam.

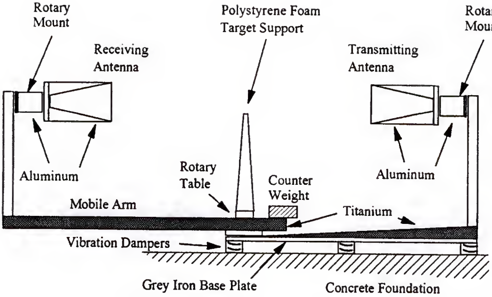

Figure 20: Schematic drawing of the microwave laboratory seen from the side (Gustafson, 1996). The target can be placed on a support made of polystyrene foam, which is mounted on a high precision rotary table. The transmitting and the mobile receiving antenna are both mounted on titanium beams that are fixed at the location of the rotation axis of the target mount. The plane of linear polarization is controlled by rotary mounts that turn the complete horn antenna assembly including collimating optics and polarizer.

The antenna assemblies are identical, each consisting of a conical horn, a collimating Fresnel lens and a grid polarizing filter. Although the antennas are only 135 cm from the scattering object, the Fresnel lens produces a nearly flat wave front over a 20 to 25 cm diameter spherical volume surrounding the scattering object. Thus, the illumination is as if it originated from a distant source. The identical Fresnel lens on the receiving antenna increases the sensitivity to radiation propagating in a single direction, as light intercepted by a distant observer. This approximates the idealized conditions of a far field measurement in the laboratory. At the same time, the angular resolution is

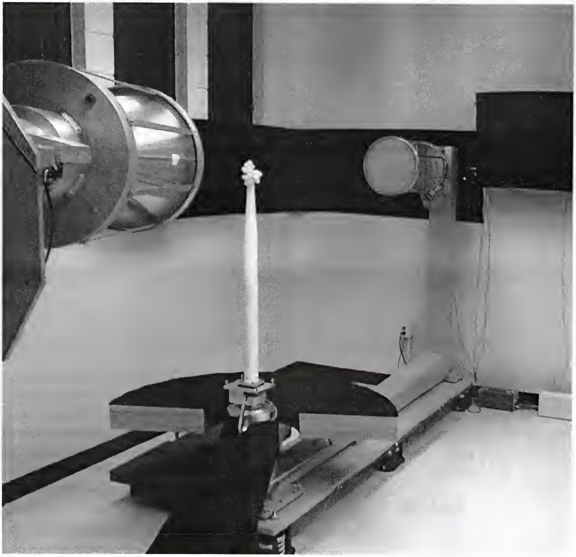

Figure 21: Photograph showing the microwave scattering facility. View is from behind the mobile receiving antenna, seen in the foreground, with a multi-sphere target on the support platform in the center and the transmitting antenna in the background.

increased compared to a configuration using a direction insensitive detector. Furthermore, each antenna assembly can be rotated around its symmetry axis, so that the direction of the polarization of transmitted and received radiation can be independently controlled. A more extensive description of the laboratory is given by Gustafson (1996).

3.2.1 Modes of Operation

In this dissertation the microwave laboratory has been used in two different modes of operation; (i) fixed orientation measurement - the scattering object is in a fixed orientation while the scattered radiation is measured as a function of scattering angle (defined in Figure 19); (ii) average over rotation - the object is continuously rotated while measurements are taken in such a way, that the recorded scattering properties are effectively averaged over rotation. The average over rotation is also referred to as the rotational average. When the fixed orientation measurements are carried out, the scattering object is placed on a rigid support (Figure 20 and Figure 21). In this mode, each measurement is followed by a separate measurement of the background scattering, which is due to the scattering by the support and reflections from the laboratory walls etc. In the data reduction, the *background measurement* is subtracted from the original measurement - here referred to as *the target measurement*. In Figure 22, this procedure is illustrated for a Bk7 glass sphere. The support is usually a cylindrical piece of tapered polystyrene foam, because this material has a low refractive index due to its low density. The scattering by the support is reduced because of its low refractive index.

When the average over rotation is measured, the background needs to be determined before the target measurement in order to be able to subtract the value of the background continuously during the actual measurement. In this mode it is essential that the data reduction is done parallel to the averaging, because the quantity that is being averaged, is the intensity. This latter type of measurement lacks the high level of position control offered by the former. In addition, the background measurement is only approximate, as the supporting nylon strings are not included. However, the increased efficiency in collecting the data required to determine the average accurately, still

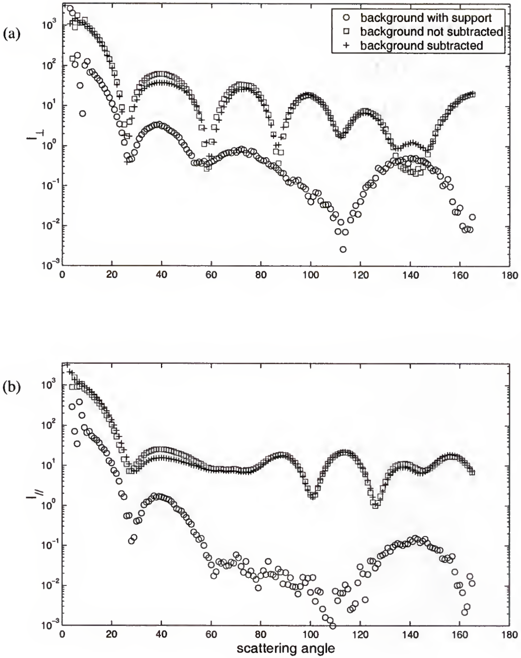

Figure 22: An example of the target (squares) and background (circles) measurements for a Bk7 glass sphere on a polystyrene foam support are shown together with the reduced result after the background has been vector subtracted (crosses). a) perpendicular polarization; b) parallel polarization.

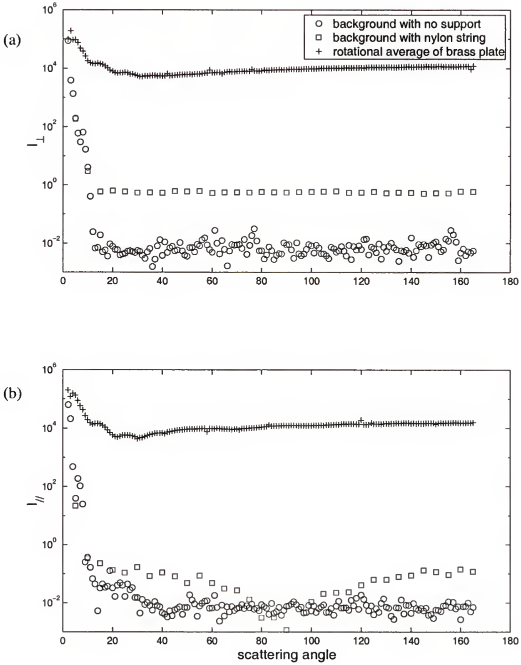

Figure 23: The scattering by a 25 by 50 mm thin brass plate (crosses) compared to the background with no support (circles) and the scattering by a vertically orientated nylon string (squares) used for mounting targets in this type of measurement. a) perpendicular polarization; b) parallel polarization.

motivates this approach. Figure 23 shows the background level without any support in the beam and the scattering by a nylon string compared to an example of an average over rotation measurement. It is shown that the background measurement is of most importance in the forward direction (zero degree scattering angle) and the scattering by the nylon string is several magnitudes lower than the scattering by the rotating object. Hence, in this type of measurement the nylon string does not greatly affect the scattering by the rotating object it supports.

3.2.2 Calibration

Calibration is generally achieved by measuring the scattering by a sphere made of high optical quality, such as Bk7 glass and comparing the measurement to calculations using Mie-theory. An example of such a comparison is shown in Figure 24. Through this procedure a set of calibration constants are determined, one for each frequency and polarization. A calibration measurement requires a relatively small amount of time and is acquired every time the equipment is restarted. The calibration also allows the user to check that everything is working correctly before a long set of measurement is begun.

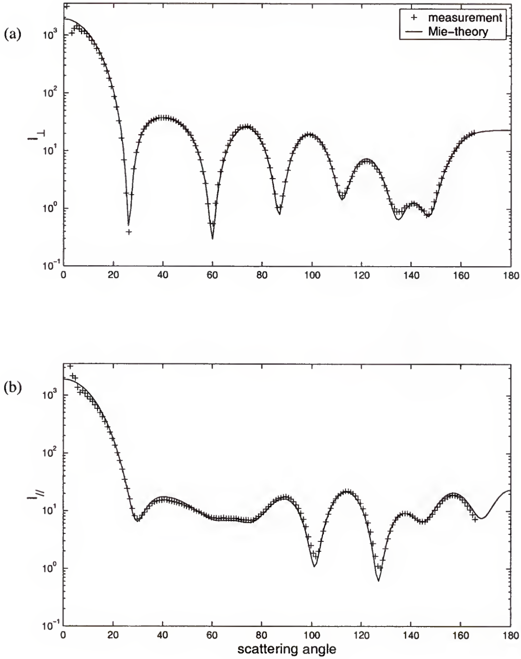

Figure 24: Comparison between measured (crosses) and calculated (solid line) polarized scattered intensity perpendicular (a) and parallel (b) to the scattering plane. The scattering is for a BK7 glass (m=2.516 –i0.02) sphere with the diameter 2.5 λ, i.e. with a size parameter 7.85.

CHAPTER 4
SCATTERING BY A DIELECTRIC FLAKE OF FINITE THICKNESS

Rigorous asymptotic diffraction methods have been derived only for perfectly conducting and non-penetrable impedance wedges and half-planes. In this chapter, a new scattering approximation for a thin dielectric flat flake of finite thickness and rectangular shape (Figure 25) is developed within the premise of GTD. Previous approximations for dielectric flakes (Burnside and Burgener, 1983; Rouviere et al., 1999) were based on modifications of the uniform GTD formulation for a perfectly conducting half-plane.

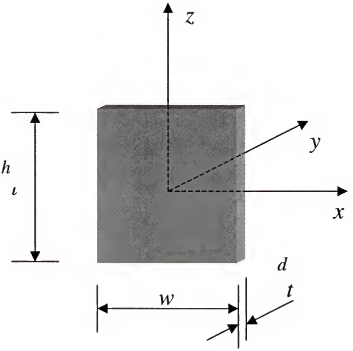

Figure 25: Geometry of the dielectric flake for which a scattering approximation is developed. With the light incident in the y-direction and x-y plane corresponding to the scattering plane, w, h and d represent the width, height and thickness of the flake, respectively.

Our approximate scattering model is based on the diffraction by an impedance half-plane and considers the scattered light as a sum of two parts, (i) the external scattered light and (ii) the transmitted scattered light. These parts are treated separately and ultimately added together with the proper phase relation. Hence, the total electric field of the scattered light is written

$$\mathbf{E}_{total} = \mathbf{E}_{external} + \mathbf{E}_{transmitted} \tag{4- 1}$$

The thickness, *d*, of the flake is neglected except to relate the phase of the external and transmitted scattered field. We start by considering the two-dimensional problem of the scattering by a dielectric slab of infinite height, *h*, but finite width, *w*, and thickness, *d*.

In order to find $\mathbf{E}_{external}$ for a dielectric slab, the parallel edges are treated as if they were infinitesimally thin with no transmission. In this case, as a first estimate, an impedance boundary condition (IBC) solution for a half-plane can be applied. However, due to the approximate nature of the IBC, the accuracy of this solution decreases with lower refractive index. To compensate for the inexactness inherent to the IBC's, we introduce a couple of heuristic modifications to the result of the impedance model. First, an *effective refractive index* is introduced in order to improve the diffraction pattern when radiation is incident close to the Brewster angle. Second, a correction factor is applied which adjusts the amplitude of the external scattered light in the direction of the specular reflection. This correction factor is based on the difference between the reflection coefficient given by the impedance boundary conditions and the reflection coefficient based on the exact boundary conditions and thus obtained with the Fresnel's equations.

The transmitted field $\mathbf{E}_{transmitted}$ is found by considering it similar to the field of the transmitted light, diffracted through a slit that is complementary to the slab. There will be transmitted light not only in the forward direction, but also in the direction of specular reflection, due to the light undergoing internal reflections. To account for the internal reflections, a set of *effective reflection and transmission coefficients* are derived. These coefficients account for the dielectric properties of the slab and determine the amplitude and phase (with respect to the external field) of the transmitted field.

Finally, the finite height of the rectangular flake is taken into account by applying the method of equivalent currents in the manner described in Section 2.4.

4.1 External Scattered Field

Our modeling of the external scattered light is based on a uniform theory of diffraction solution for the scattering by an impedance half-plane (Volakis, 1986; Senior and Volakis, 1995). The diffraction coefficients of this solution reduce to the UTD diffraction coefficients for the perfectly conducting half-plane, presented in Section 2.1.

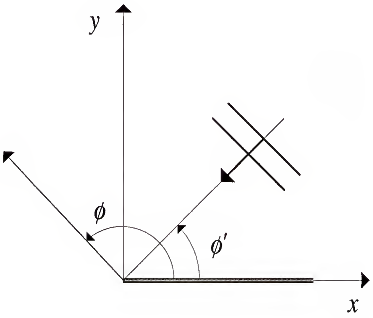

Figure 26: Plane wave incident normal to the edge of a half-plane.

Within GTD the diffracted field $\mathbf{E}^d$ in the space around the impedance half-plane (Figure 26) can be expressed in the following way

$$\mathbf{E}^d = \mathbf{E}^i \cdot \overline{\mathbf{D}} \cdot \frac{e^{-jk\rho}}{\sqrt{\rho}} \tag{4- 2}$$

where $\mathbf{E}^i$ is the incident field, ρ is the distance to the observation point, and $\overline{\mathbf{D}}$ is the dyadic diffraction coefficient with the form

$$\overline{\mathbf{D}} = \begin{bmatrix} D_\perp & 0 \\ 0 & D_{//} \end{bmatrix} \tag{4- 3}$$

For a plane wave incident normal to a half-plane with impedance η, the elements of $\overline{\mathbf{D}}$ are defined by Senior and Volakis (1995) as

$$\begin{aligned} D_\perp(\phi,\phi',\eta) = -\frac{e^{-j\pi/4}}{2\sqrt{2\pi k}}\Bigg[& C_1(\phi,\phi',\eta) sec\left(\frac{\phi-\phi'}{2}\right) F\left(2ks\, cos^2\frac{\phi-\phi'}{2}\right) \\ & + C_2(\phi,\phi',\eta) sec\left(\frac{\phi+\phi'}{2}\right) F\left(2ks\, cos^2\frac{\phi+\phi'}{2}\right)\Bigg] \end{aligned} \tag{4- 4}$$

$$D_{//}(\phi,\phi',\eta) = D_\perp\left(\phi,\phi',\frac{1}{\eta}\right)$$

where

$$\begin{aligned} C_1(\phi,\phi',\eta) &= \frac{2\eta\, sin\,\phi/2\, sin\,\phi'/2+1}{2\, sin\,\phi/2\, sin\,\phi'/2+1} \cdot K_+(cos\,\phi,\eta) K_+(cos\,\phi',\eta) \\ C_2(\phi,\phi',\eta) &= \frac{2\eta\, sin\,\phi/2\, sin\,\phi'/2-1}{2\, sin\,\phi/2\, sin\,\phi'/2+1} \cdot K_+(cos\,\phi,\eta) K_+(cos\,\phi',\eta) \end{aligned} \tag{4- 5}$$

The angles ϕ' and ϕ defines the direction of the incident and diffracted radiation according to Figure 26. Furthermore, F is the transition function (given in Section 2.1) and K_+ is the upper Wiener-Hopf split function defined as

$$K_+(\cos\phi,\eta)=\frac{4}{\sqrt{\eta}}\sin\frac{\phi}{2}\left\{\frac{\psi_\pi(3\pi/2-\phi-\xi)\psi_\pi(\pi/2-\phi+\xi)}{(\psi_\pi(\pi/2))^2}\right\}^2 \cdot\left\{\left[1+\sqrt{2}\cos\left(\frac{\pi/2-\phi+\xi}{2}\right)\right]\left[1+\sqrt{2}\cos\left(\frac{3\pi/2-\phi-\xi}{2}\right)\right]\right\}^{-1} \tag{4-6}$$

where

$$\sin\xi=\frac{1}{\eta} \tag{4-7}$$

Finally, $\psi_\pi(\alpha)$ is the Maliuzhinets function for a half-plane (Maliuzhinets, 1958), which is defined as follows

$$\psi_\pi(\alpha)=\exp\left\{\frac{1}{8\pi}\int_0^\alpha\frac{\pi\sin u-2\sqrt{2}\pi\sin u/2+2u}{\cos u}du\right\} \tag{4-8}$$

In this integral form, however, the Maliuzhinets function is a great deterrent in calculating the diffraction coefficients. In our computations, we instead employ the integral and large argument approximation developed by Herman et al. (1987).

Although employing this IBC solution to describe the external scattering by a dielectric flake is an improvement compared to using the UTD formalism for a perfect conductor, the approach still has a shortcoming. The IBC's are derived under the assumption that $|m| >> 1$, and thus their accuracy decreases with a lower refractive index. This was also noted in Section 2.3, where it was shown that while the IBC solution agreed relatively well with experiment when the scatterer had a refractive index $m = 2.52 - i0.03$, the agreement was quite poor when the scattering object had a lower refractive index $m = 1.62 - i0.003$, with the largest discrepancy being the difference in intensity levels of the scattered light in the direction of specular reflection. This difference can be further understood by comparing the reflection coefficients derived using the IBC's with

Fresnel's reflection coefficients, which are based on the exact boundary conditions. Figure 27 and Figure 28 compare the reflection coefficients for both perpendicular and parallel polarized light when incident on a surface with $m = 2.52$ and $m = 1.62$, respectively. It can be seen that when the light is incident either normal or grazing to the surface, the two sets of reflection coefficients agree. This occurs because at normal and grazing incidence, the expressions given by the IBC's are exact. For angles in between, it can be seen that the reflection coefficients based on the IBC's differ more from the Fresnel coefficients in the case when the refractive index is smaller. In particular for parallel polarization, the Brewster angle is not exactly simulated by the IBC's and the error is hence infinite at the Brewster angle.

Under the assumption that the diffraction in the direction of the specular reflection is proportional to the reflection coefficient, the most direct manner to adjust the diffracted field, in the theoretical calculations, appeared to be by multiplying the diffracted field by the ratio between the Fresnel and IBC reflection coefficient, r_{Fres}/r_{IBC}. This correction was carried out in the case of the acrylic cube, discussed in Section 2.3, and the comparison between this modified IBC solution and microwave measurement is shown in Figure 29. The agreement between the intensity levels in the direction of specular reflection is improved compared to Figure 16 in Section 2.3. However, this type of correction does not work when the light is incident at or near the angle where $r_{//,IBC} = 0$, because the correction factor, in this case, becomes singular in the same way as the error in $r_{//,IBC}$ is infinite at the Brewster angle.

Instead, we chose to approach this problem by introducing an *effective refractive index*, m_e, and the corresponding *effective impedance* η_e for the surface, which brings the

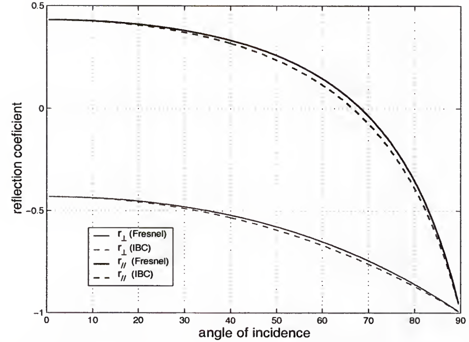

Figure 27: Comparison of the reflection coefficients for a plane wave incident on a planar surface with $m = 2.52$, using IBC's and Fresnel's equations.

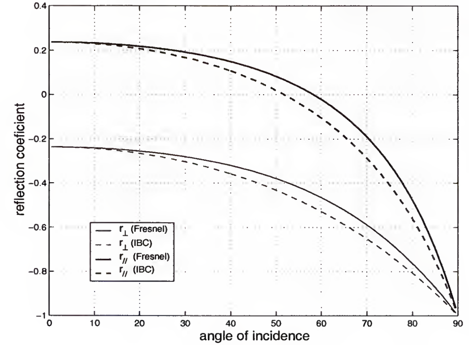

Figure 28: Comparison of the reflection coefficients for a plane wave incident on a planar surface with $m = 1.62$, using IBC's and Fresnel's equations.

Brewster angle of the IBC's to the identical angle at which the Fresnel reflection coefficient for parallel polarized light vanishes. This approach also ensures a better agreement for the shape of the diffraction pattern when the light is incident at an angle near the Brewster angle. To derive the expression for the effective refractive index, we first write down the equation for the reflection coefficient for the parallel polarization based on the IBC's. As a function of the refractive index m and the angle of incidence θ_i with regard to the normal of the surface, the reflection coefficient, $r_{//,IBC}$, is given by

$$r_{//,IBC} = \frac{1 - m\cos(\theta_i)}{1 + m\cos(\theta_i)} \tag{4- 9}$$

With the Brewster θ_B angle defined as

$$\theta_B = \arctan(m) \tag{4- 10}$$

the effective refractive index, m_e, is obtained by setting equation (4- 9) to zero at $\theta_i = \theta_B$, hence

$$\frac{1}{m_e} = \cos(\arctan(m)) \tag{4- 11}$$

When the effective refractive index defined above is used in the IBC solution for the impedance half-plane, the shape of the diffraction pattern is improved and the ratio r_{Fres}/r_{IBC} is well defined for all angles. Figure 30 shows examples of the angular dependence of r_{Fres}/r_{IBC} when a plane wave is incident onto a surface with a refractive index m = 1.3, 1.6, 2.5, and 5. It can be seen that the ratio r_{Fres}/r_{IBC} approaches unity as refractive index increases. This is expected, since the larger the refractive index, the better the IBC's model the exact boundary conditions.

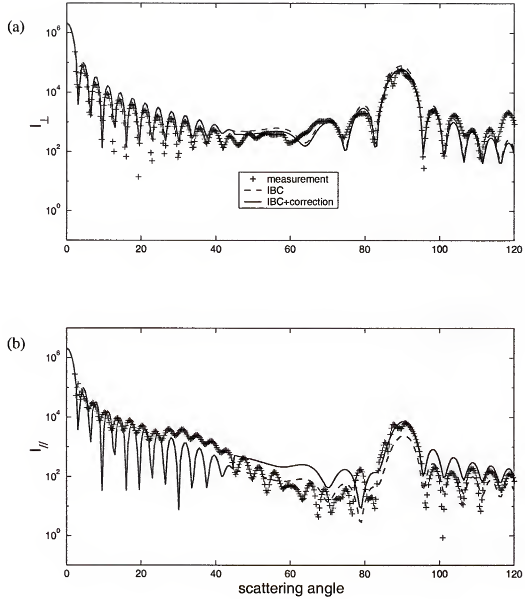

Figure 29: Scattering by a cube with 12.7 λ wide sides. The microwave measurements (crosses) are for a cube made of acrylic with aluminum foil on the two sides facing the forward direction (compare Figure 14 in Section 2.3) blocking radiation from being transmitted in the forward direction. The dashed line shows calculations based on an IBC solution (Syed and Volakis, 1995), with m=1.62 –i0.003. The solid line shows the result when the adjustment of multiplying the IBC with the ratio r_{Fres}/r_{IBC} in the direction of specular reflection (compare Figure 16 in Section 2.3). a) perpendicular polarization; b) parallel polarization.

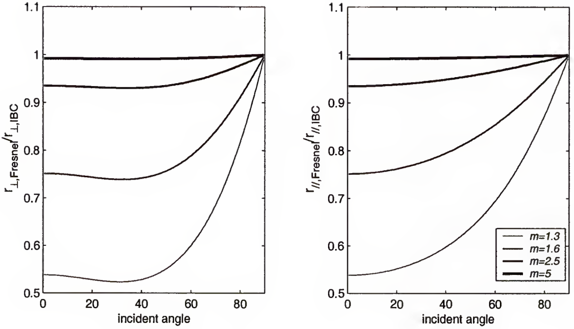

(a) (b)

Figure 30: The ratio of the reflection coefficients based on Fresnel's equations and the IBC. The influence of the refractive index is illustrated by comparing refractive indices m = 1.3, 1.6, 2.5, and 5. The ratio approaches unity for all incidence angles as the refractive index increases, since the IBC's then more closely correspond to the exact boundary conditions. a) perpendicular polarization; b) parallel polarization.

The final expression for the diffraction coefficients for the external scattering by a dielectric half-plane using our heuristic approach can now be written down as

$$D_{\perp,//}(m)=\frac{r_{\perp,//,Fres}}{r_{\perp,//,IBC}}D_{\perp,//}(m_e) \tag{4- 12}$$

where the expression for $D_{\perp,//}(m_e)$ is given by equation (4- 4) in which η is replaced by the effective impedance η_e, given by

$$\eta_e=\frac{1}{m_e} \tag{4- 13}$$

The electric field of the external scattering by a dielectric slab can now be obtained by summing the fields diffracted externally by each edge q of the slab,

$$\mathbf{E}_{external}^{slab} = \sum_{q=1}^{2} \mathbf{E}_q^d = \sum_{q=1}^{2} \mathbf{E}_q^i \overline{\mathbf{D}}_q \frac{e^{-jk\rho_q}}{\sqrt{\rho}} \qquad (4\text{- }14)$$

where $\overline{\mathbf{D}}_q$ is the dyadic diffraction coefficient based on equation (4- 12) and ρ_q is the distance between the observation point and diffracting edge q. In Figure 31, the above given solution for the external scattering by a dielectric slab is compared with microwave measurements of the scattering by a thin Bk7 glass flake. The finite length of the dielectric flake is taken into account by using the method of equivalent currents, reviewed in Section 2.4. Not taking the transmitted light into account in the theoretical solution seems to mainly affect the intensity of the scattered light. The shape of the diffraction pattern, referring to the frequency of the maxima and minima corresponding to constructive and destructive interference, respectively, is for the most part similar. Thus, a good approximation of the transmitted light, may be possible to achieve by treating it as the light diffracted through an aperture with the same dimensions as the slab. This is seen particularly in the forward direction, i.e. zero scattering angle.

4.2 Transmitted Scattered Field

From the comparison made in the previous section (Figure 31) it was realized that it may be possible to acquire an approximation for the transmitted part of the scattered light by treating it as the light diffracted through an aperture with the same dimensions as the slab. In order to obtain an expression for the scattered light that is transmitted through the dielectric slab, we first treat the slab as if its material properties were the same as

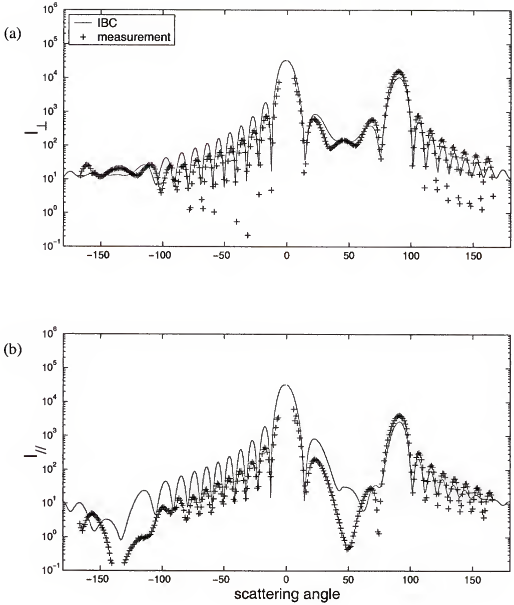

Figure 31: Comparison between microwave measurement (crosses) of the scattering by a 0.15 λ thin Bk7 glass flake with large dimensions 6.35 λ by 6.35 λ and the modified IBC solution (solid line), which does not take the transmitted light into account. Note the diffraction peaks in the forward direction (zero degree scattering angle) and direction of specular reflection (here at 90 degree scattering angle). a) perpendicular polarization; b) parallel polarization.

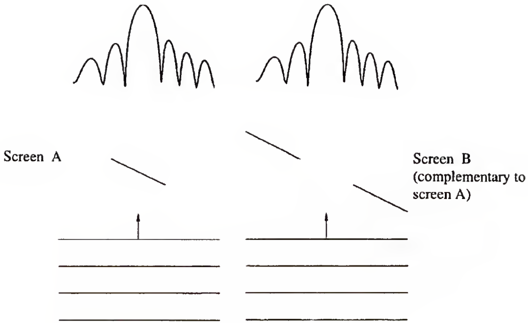

Figure 32: Illustration of the similar diffraction patterns when plane waves are incident on complementary screens.

those of free space. Further, we assume that the transmitted light through such a slab can be viewed as the light diffracted through a slit, which is geometrically complementary to the slab (Figure 32).

There is no rigorous equivalence principle for complementary screens made of dielectric material, such as the Babinet's principle for perfectly conducting thin complementary screens (Booker, 1946). However, in order to here obtain an approximate expression for the diffracted radiation transmitted through the slab, we chose to employ the scalar form of Babinet's principle relating the diffraction by complementary opaque thin screens (Born and Wolf, 1980) and write down the relation between the diffracted light transmitted through the slit complementary to the slab and the external diffracted light by the original slab as

$$\mathbf{E}_{slab} + \mathbf{E}_{slit} = \mathbf{E}_{incident} \tag{4- 15}$$

This way, the diffraction coefficients for the light transmitted through the slit in the forward direction can be written as

$$\mathbf{D}'_{transmitted} = \mathbf{D}_{external} \cdot e^{-i\pi} \tag{4- 16}$$

By the forward direction it is meant all directions into the half-space in front of the slab limited by the plane tangent to the surface of the slab or its complementary screen; all other directions are referred to as the backward direction (Figure 33).

Using this approximation, the external diffracted light from the original slab and the diffracted light transmitted through a slab, with refractive index of free space, have the same diffraction patterns away from the incident direction and they cancel each other when they are added.

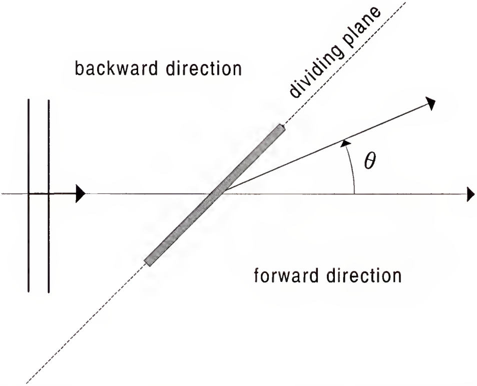

Figure 33: Plane tangent to the surface of the slab dividing the scattering directions into the two half spaces referred to as forward and backward direction, respectively.

In order to take the thickness and the dielectric properties of the slab into account we develop expressions for the *effective reflection* (r_{eff}) and *effective transmission* (t_{eff}) *coefficients* with the proper phase relation. With these coefficients the total diffraction coefficient for the scattered field by a dielectric slab can be written on the following form

$$\begin{aligned} \mathbf{D}_{total} &= \mathbf{D}_{external} + t_{eff} \cdot \mathbf{D}'_{transmitted} && \text{(forward direction)} \\ \mathbf{D}_{total} &= r_{eff} \cdot \mathbf{D}_{external} && \text{(backward direction)} \end{aligned} \tag{4- 17}$$

To analyze reflections and transmissions of a uniform plane wave incident on the slab at an arbitrary angle, we will reintroduce the plane of incidence, which is defined as the plane formed by a unit vector normal to the reflecting interface and the vector in the in direction of incidence. At each interface of the slab, the reflection and transmission coefficients $r_\perp$, $r_{//}$, $t_\perp$, and $t_{//}$, corresponding to light with its electric field vector perpendicular and parallel to the plane of incidence, are found using the Fresnel's equations. Here, we will let $r_{1(\perp,//)}$ and $r_{2(\perp,//)}$ represent the reflection coefficients for external and internal reflection, respectively, whereas $t_{1(\perp,//)}$ and $t_{2(\perp,//)}$ will represent the transmission coefficients into and out of the slab, respectively. The phase of the reflected and transmitted fields also depends on the optical path length. In order to account for differences in path length and the associated phase shifts we introduce the distances δ_1, δ_2 and δ_3, which are shown in Figure 34, and define the following phase shifts

$$\begin{aligned} \Delta_1 &= e^{-jk'\delta_1} \\ \Delta_2 &= e^{jk\delta_2} \\ \Delta_3 &= e^{jk\delta_3} \end{aligned} \tag{4- 18}$$

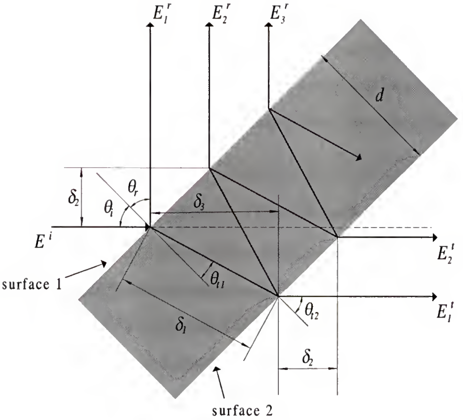

Figure 34: Illustration of the differences in optical path lengths for the light transmitted through a slab of thickness *d*.

where

$$\begin{aligned}\delta_1 &= d/\cos\theta_{t1}\\ \delta_2 &= 2\delta_1 \sin\theta_{t1} \sin\theta_i\\ \delta_3 &= \delta_1 \cos(\theta_i - \theta_{t1})\end{aligned} \qquad (4\text{-}19)$$

and the angles θ_r, θ_{t1}, and θ_{t12}, defined in Figure 34, are related to the incident angle θ_i via Snell's laws of reflection and refraction. Furthermore, d is the thickness of the slab and k and k' are the respective propagation constants in free space and in the dielectric material. The first phase shift, Δ_1, is the phase delay accompanying the field during a single transit through the slab. The phase shift Δ_2 accounts for the difference in path length for different rays leaving the slab. Finally, the phase shift Δ_3 is needed to relate the phase of the rays transmitted through the slab on the far side (surface 2 in Figure 34) to the front surface (surface 1 in Figure 34).

We can now write down the expression for the total reflection and transmission, r_{tot} and t_{tot}, respectively as

$$\begin{aligned} r_{tot} &= r_1 + r_t = r_1 + t_1 t_2 \sum_{n=2}^{N} r_2^{2n-3} \Delta_1^{2n-2} \Delta_2^{n-1} \\ t_{tot} &= \left(t_1 t_2 \Delta_1 + t_1 t_2 \sum_{n=2}^{N} r_2^{2n-2} \Delta_1^{2n-1} \Delta_2^{n-1} \right) \Delta_3 \end{aligned} \qquad (4\text{-}20)$$

where r_t is the part of the reflection coefficient that correspond to light transmitted in the direction of reflection after internal reflection(s). The integer (N-1) corresponds to the number of internal reflections that take place. If the width of the slab is infinite, N→ ∞. How many internal reflections that should be taken into account depends on how the surfaces, which form the edges of the slab, should be treated. Here we consider that the surface of the edges is flat and perpendicular to the front and back surface. In this case a fraction of the light will leak out, but the internal reflections will continue with the same angle of reflection, until all light is transmitted or absorbed, thus N→ ∞.

As already mentioned in the previous section, the diffraction coefficient is proportional to the reflection coefficient, r_1, in the direction of specular reflection. In order to derive an expression for the effective reflection coefficient, which includes the contribution from internal reflections, we write the diffraction coefficient for the externally diffracted field $D_{external}$ in the following form

$$D_{external} = r_1 \cdot f_d \qquad (4\text{-}21)$$

where f_d is a function that only contains information about the shape of the diffraction pattern. Next, the diffraction coefficient for the light, which after multiple internal reflections, is transmitted in the direction of reflection, $D''_{transmitted}$, can be expressed as

$$D''_{transmitted} = r_t \cdot f_d \tag{4- 22}$$

With the aim of writing down the diffraction coefficient for the scattered field in the backward direction in the form given in equation (4- 17), and using equations (4- 21) and (4- 22), the expression for the effective reflection coefficient, r_{eff}, is developed in the following way

$$\begin{aligned} D_{total} &= D_{external} + D''_{transmitted} = D_{external} + r_t \cdot f_d = D_{external} + r_t \cdot \frac{D_{external}}{r_1} \\ &= \left(1 + \frac{r_t}{r_1}\right) D_{external} = r_{eff} \cdot D_{external} \end{aligned} \tag{4- 23}$$

where the effective reflection coefficient r_{eff} hence is defined by

$$r_{eff} = \left(1 + \frac{r_t}{r_1}\right) \tag{4- 24}$$

On the other hand, the diffraction coefficient for the total diffracted light in the forward direction can now be expressed as

$$D_{total} = D_{external} + D_{transmitted} = D_{external} + t_{eff} D'_{transmitted} \tag{4- 25}$$

where the effective transmission coefficient t_{eff} is equal to t_{tot}.

4.3 Total Scattered Field

To write down the total scattered field by a thin dielectric slab we only need to replace the dyadic diffraction coefficient in equation (4- 14). That is,

$$\mathbf{E}_{total}^{slab} = \sum_{q=1}^{2} \mathbf{E}_{total,q}^{d} = \sum_{q=1}^{2} \mathbf{E}_{q}^{i} \overline{\mathbf{D}}_{total,q} \frac{e^{-jk\rho_q}}{\sqrt{\rho}} \qquad (4\text{-}26)$$

where $\overline{\mathbf{D}}_{total}$ includes the new diffraction coefficients developed above for each half space of forward and backward directions. By applying the results of the method of equivalent currents in Section 2.4, the explicit formulation of the scattering by a flake of finite height *h* can ultimately be written as

$$\begin{aligned} \mathbf{E}_{total}^{plate} &= j\frac{e^{-j\pi/4}}{\sqrt{2\pi}} h\sqrt{\frac{k}{\rho}} \cos\psi \frac{\sin(kl\sin\psi)}{kl\sin\psi} \mathbf{E}_{total}^{plate} \\ &= j\frac{e^{-j\pi/4}}{\sqrt{2\pi}} h\sqrt{k} \cos\psi \frac{\sin(kl\sin\psi)}{kl\sin\psi} \sum_{q=1}^{2} \mathbf{E}_{q}^{i} \overline{\mathbf{D}}_{total,q} \frac{e^{-jk\rho_q}}{\rho} \end{aligned} \qquad (4\text{-}27)$$

where ψ describes the angle between the direction of the observation point and the scattering plane. In Figure 35 the scattering by a dielectric flake predicted by our model is compared with the same measurement that was demonstrated in Figure 31 (in which the measurement was shown in comparison with the calculation of external scattered field). Here the transmitted scattering is included in the calculation and the overall agreement between model and experiment is good except in the directions along the surface of the flake (here 45 and -135 degrees scattering angle), where the theoretical model possesses a discontinuity. This discontinuity, however, is an expected trait of our model due to the manner in which the transmitted part of the scattering is taken into account.

Further evaluation our scattering model is made in Chapter 5, where predictions by the model are compared with laboratory microwave measurements of different flakes in various orientations.

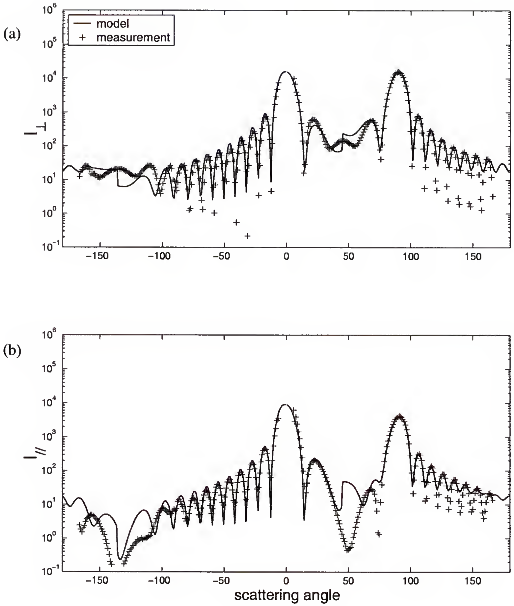

Figure 35: Comparison between microwave measurement (crosses) of the scattering by a 0.15 λ thin Bk7 glass flake with large dimensions 6.35 λ by 6.35 λ and our heuristic solution (solid line). An overall agreement is found except in the directions along the surface of the flake. The discontinuity at these angles (here 45 and -135 degrees scattering angle), are due to how the transmitted part of the scattering is taken into account in the model. a) perpendicular polarization; b) parallel polarization.

CHAPTER 5

ASSESSMENT OF THE SCATTERING MODEL

The new electromagnetic scattering model developed for dielectric flakes in the previous chapter is an approximate one and it thus remains essential to examine the extent of its validity. This is the topic of this chapter, wherein results derived from the model are compared to experimental data collected in controlled laboratory scattering measurements.

In the first part of this chapter (Sections 5.1 – 5.4), we assess our model for the scattering by flakes with regard to the assumptions made in the model (i.e. scattering by a thin rectangular flake oriented in such a way that two of its edges are kept perpendicular to the scattering plane). The range of the model is tested both in the case of scattering by flakes in fixed orientation (Section 5.1) and in the case of scattering averaged over the rotation of the flake (Section 5.2). We show that the prediction by the model approaches the one offered by the geometric optics approximation as the large dimensions (width and height) of the flake are increased (Section 5.3). In connection with these tests, we also present a comparison of some of the experimental scattering data to DDA calculations (Section 5.4).

The flakes used in the various tests are made of either Bk7 glass or acrylic, which at the laboratory range of wavelengths (2.7-4.0 mm) have the refractive index $m = 2.52 - i0.030$ and $m = 1.62 - i0.003$, respectively. Bk7 glass is a standard optical material of high quality known for its homogeneity. Whereas Bk7 glass has a rather high refractive index, acrylic has a refractive index in the range commonly found in natural materials. Acrylic is specifically used as an analog material for silicate in microwave scattering experiments. The acrylic material, from which the test flakes for our experiments were machined, appears to be very homogeneous and most of the flakes were made from the same stock.

In the latter part of the chapter, we evaluate the possibility of using our model to describe the scattering by flakes in general, specifically with regard to other shapes (Section 5.5) and random orientation (Section 5.6). Section 5.7 gives a summary of the assessment.

5.1 Fixed Orientation

In this section, theoretical predictions from our scattering model are compared with microwave measurements for a flake in a fixed orientation. The physical parameters of the test flakes are listed in Table 1. A number of different orientations and a range of flake dimensions have been used for the comparisons (Figure 36 through Figure 49). In Figure 36 through Figure 41, the flake is made of Bk7 glass. In Figure 44 through Figure 49, the flake is made of acrylic. The flake, orientation and wavelength used for a particular comparison are indicated in the figure caption. The orientation of the flake with regard to the incident light is illustrated in Figure 10 (Chapter 2).

In Figure 36 and Figure 37, the result of the scattering omitting the transmission is also plotted, so as to illustrate the effect of the transmitted part in the total scattered light. In Figure 36 and Figure 37, which show the scattering by flakes of various thickness, different effects of interference can be seen. Particularly in the forward direction, the

Table 1: Data for the flakes used in the test simulations, in which the light scattering by a flake in certain fixed orientations is compared.

Flake	Figure	Refractive Index m	Large Dimensions width×height [λ (4mm)]	Thickness [λ (4mm)]	Aspect Ratio	Size Parameter* X
1	35–40	2.52 –i0.030	6.35×6.35	0.043	148	3.25
2	35–38	2.52 –i0.030	6.35×6.35	0.144	44	10.9
3	35-38	2.52 –i0.030	6.35×6.35	0.218	29	16.5
4	41	2.52 –i0.030	3.18×6.35	0.144	22	7.69
5	42	2.52 –i0.030	12.7×12.7	0.246	52	37.1
6	43-48	1.62 –i0.003	6.35×6.35	0.125	51	9.43
7	43-48	1.62 –i0.003	6.35×6.35	0.250	25	18.9
8	43-48	1.62 –i0.003	6.35×6.35	0.377	17	28.5
9	49	1.62 –i0.003	12.7×12.7	0.378	34	57.1

* Surface-equivalent sphere size parameter

result of destructive and constructive interference can be seen in Figure 36a,c and Figure 37a,c respectively.

The model and the experimental scattering data generally agree in and near the forward direction (zero degree scattering angle) and in and near the direction of specular reflection. This appears to be true, both for large flakes (Flakes 5 and 9 in Table 1) with a width of 12.7 λ (Figure 43 and Figure 50) and for a small flake (Flake 4 in Table 1) with a width of 3.18 λ (Figure 42). Due to the nature of the approximation there is a discontinuity in the directions along the surface of the flake. The largest disagreement is also found near these discontinuities. Nevertheless, the intensity levels in the directions along the surface of the flake are low and therefore only minimally affect the prediction. Because of the low level of intensity, the discrepancy is of less importance when the scattered intensity is averaged over the orientation of the flake, as shown in the next section.

As expected, the scattering prediction is more accurate for the Bk7 glass flakes because they have a higher refractive index, and thus, the approximation inherent to the IBC's is more accurate (Section 2.3). It also appears that the agreement between calculations and experimental data improves the thinner the flake is (Figure 40 and Figure 41).

An intrinsic predicament in treating the scattering as a sum of the external and transmitted scattered light is that at some specific angle, dependent on the refractive index and thickness of the flake, complete or close to complete destructive interference may occur in the model. In either case the result of the theoretical model will predict no or very little scattered light in the backward direction (defined in Section 4.2). Certainly, this situation is not realistic. In fact, this situation corresponds to little light being reflected from the surface, while there is still some diffraction from sources neglected in our model (e.g., light diffracted form the faces of the edges) that in this case become important. This diffraction smoothes the scattering as a function of the scattering angle, as seen in the experimental data. An example of the difficulty due to near complete destructive interference is shown in Figure 47c, where it can be seen that the scattered light in the backward direction almost vanishes in the prediction by our model. When averaging the scattered light over rotation of the flake, the effect of interference will be seen in the averaged scattering properties as a function of scattering angle, but the effect will not be as dramatic as in the case of scattering by a flake in fixed orientation. This will be shown in Section 5.2 and further discussed in Chapter 6.

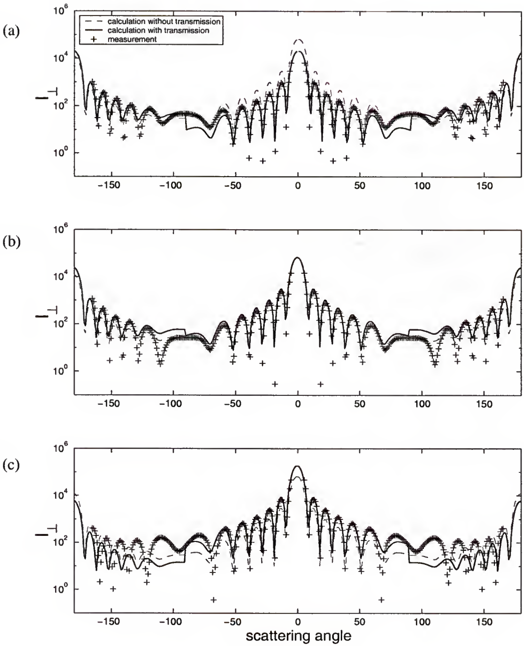

Figure 36: Comparison of the scattering model (solid line) with microwave data (crosses). Plots a – c show the scattering by Bk7 glass flakes 1-3 described in Table 1. The light is incident normal to the surface of the flake. The radiation has a wavelength of 4 mm and is polarized perpendicular to the scattering plane. The dashed line shows the result when the transmitted light is not taken into account. The discontinuity in the solid line is discussed in Section 5.1.

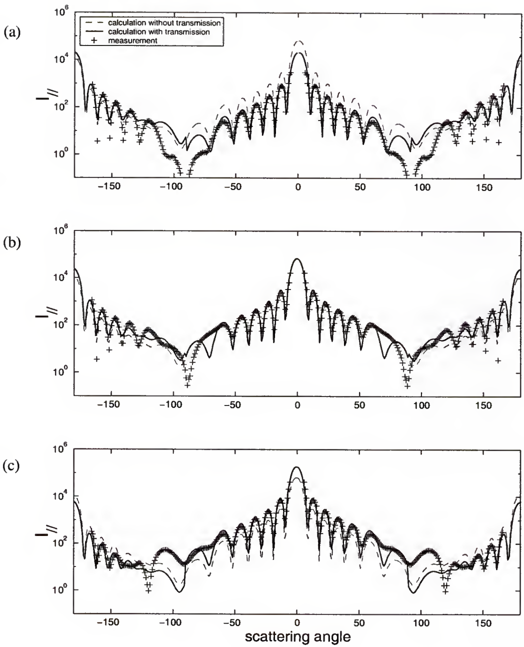

Figure 37: Same as Figure 36 except that here the radiation is polarized parallel to the scattering plane. The scattering model (solid line) is compared with microwave data (crosses). Plots a – c show the scattering by Bk7 glass flakes 1-3 described in Table 1. The light is incident normal to the surface of the flake. The radiation has a wavelength of 4 mm. The dashed line shows the result when the transmitted light is not taken into account. The discontinuity in the solid line is discussed in Section 5.1.

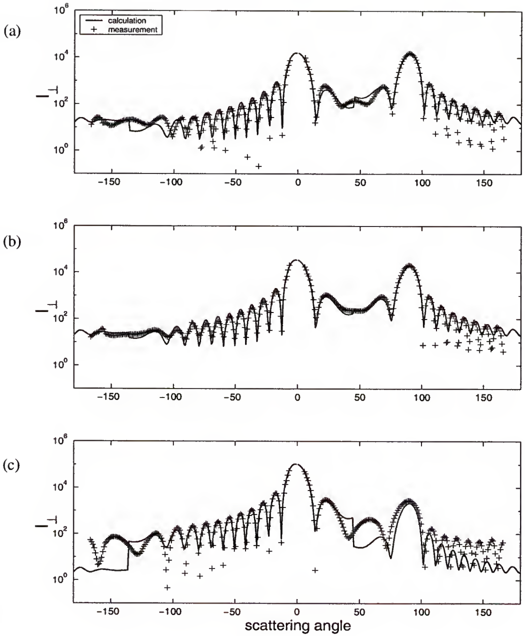

Figure 38: Comparison of the scattering model (solid line) with microwave data (crosses). Plots a – c show the scattering by Bk7 glass flakes 1-3 described in Table 1. The light is incident at 45 degrees to the normal of the flake's surface. The radiation has a wavelength of 4 mm and is polarized perpendicular to the scattering plane. The dashed line shows the result when the transmitted light is not taken into account. The discontinuity in the solid line is discussed in Section 5.1.

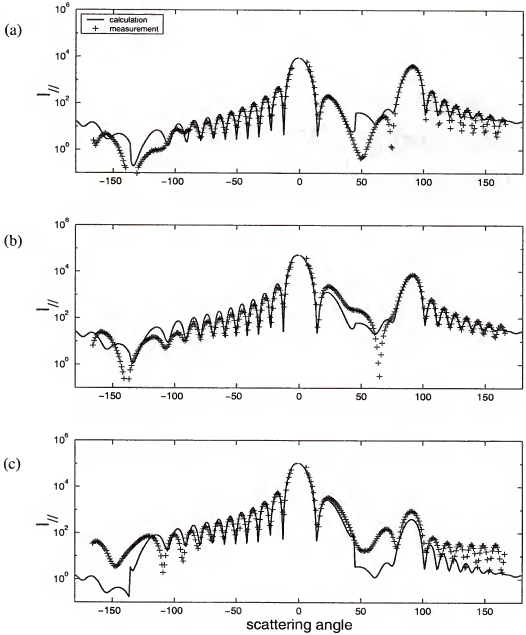

Figure 39: Same as Figure 38 except that the radiation is polarized parallel to the scattering plane. The scattering model (solid line) is compared with microwave data (crosses). Plots a – c show the scattering by Bk7 glass flakes 1-3 described in Table 1. The light is incident at 45 degrees to the normal of the flake's surface. The radiation has a wavelength of 4 mm. The dashed line shows the result when the transmitted light is not taken into account. The discontinuity in the solid line is discussed in Section 5.1.

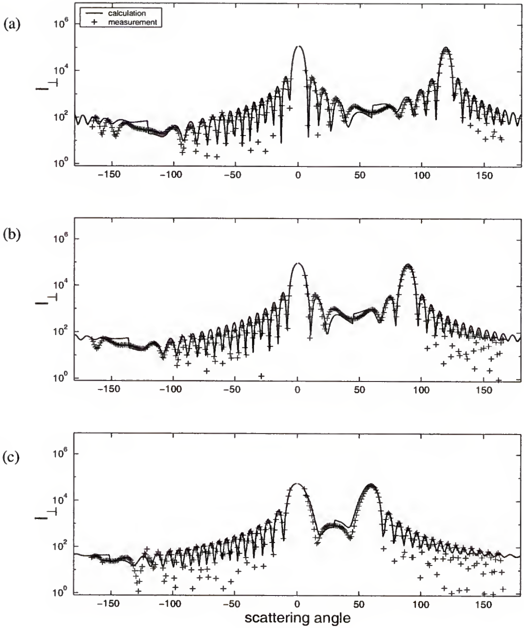

Figure 40: Comparison of the scattering model (solid line) with microwave data (crosses). Plots a – c show the scattering by Bk7 glass flake 1 (described in Table 1) with the light incident at 30, 45 and 60 degrees to the normal of the flake's surface. The radiation has a wavelength of 2.7 mm and is polarized perpendicular to the scattering plane. The discontinuity in the solid line is discussed in Section 5.1.

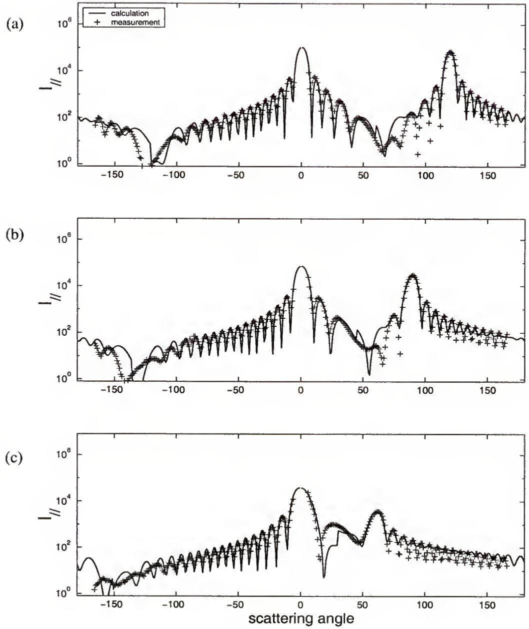

Figure 41: Same as Figure 40 except that the radiation is polarized parallel to the scattering plane. The scattering model (solid line) is compared with microwave data (crosses). Plots a – c show the scattering by Bk7 glass flake 1 (described in Table 1) with the light incident at 30, 45 and 60 degrees to the normal of the flake's surface. The radiation has a wavelength of 2.7 mm. The discontinuity in the solid line is discussed in Section 5.1.

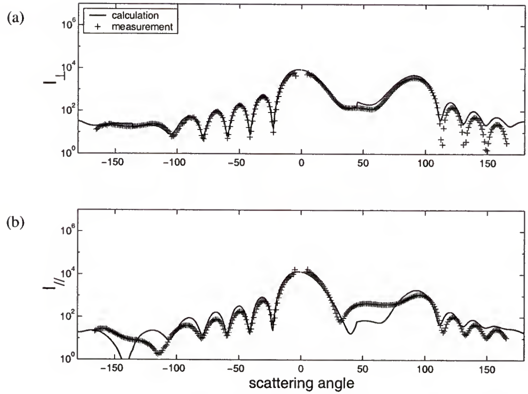

Figure 42: Comparison of the scattering model (solid line) with microwave data (crosses) for Bk7 glass flake 4 (described in Table 1) with the light incident at 45 degrees to the normal of the flake's surface. The radiation has a wavelength of 4 mm and is polarized perpendicular (a) and parallel (b) to the scattering plane. The discontinuity in the solid line is discussed in Section 5.1.

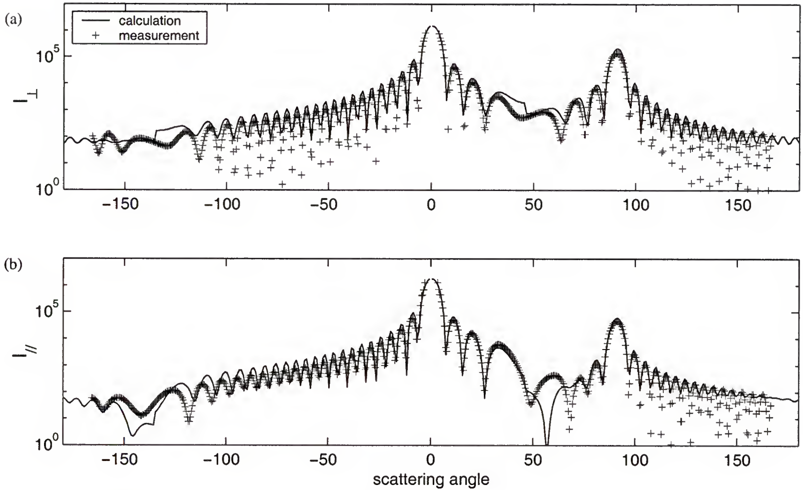

Figure 43: Comparison of the scattering model (solid line) with microwave data (crosses) for Bk7 glass flake 5 (described in Table 1) with the light incident at 45 degrees to the normal of the flake's surface. The radiation has a wavelength of 4 mm and is polarized perpendicular (a) and parallel (b) to the scattering plane. The discontinuity in the solid line is discussed in Section 5.1.

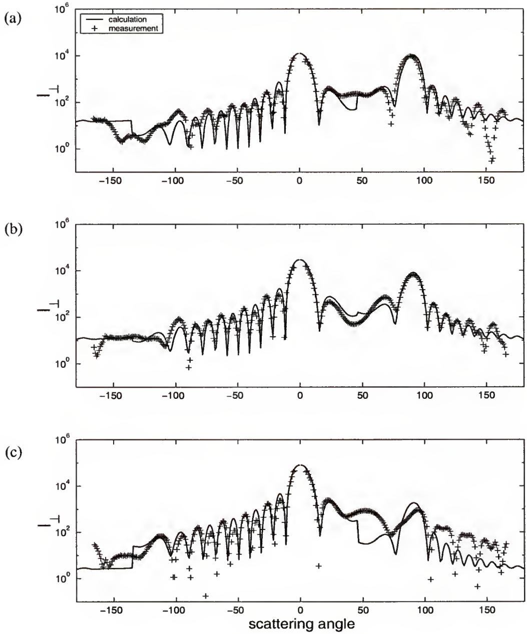

Figure 44: Comparison of the scattering model (solid line) with microwave data (crosses). Plots a – c show the scattering by acrylic flakes 6-8 described in Table 1. The light is incident at 45 degrees to the normal of the flake's surface. The radiation has a wavelength of 4 mm and is polarized perpendicular to the scattering plane. The discontinuity in the solid line is discussed in Section 5.1.

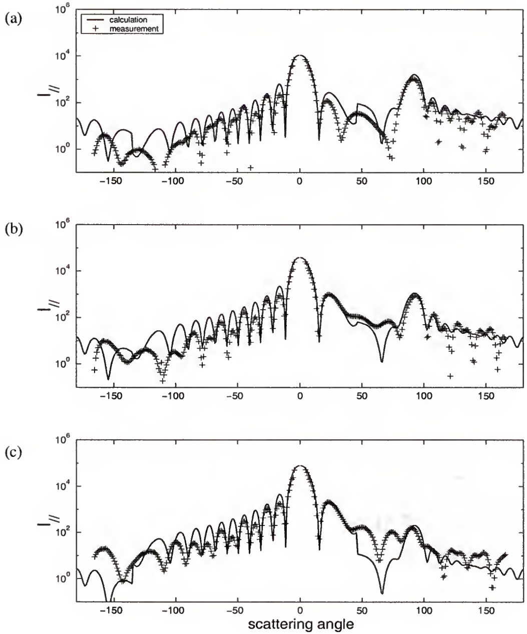

Figure 45: Same as Figure 44 except that the radiation is polarized parallel to the scattering plane. The scattering model (solid line) is compared with microwave data (crosses). Plots a – c show the scattering by acrylic flakes 6-8 described in Table 1. The light is incident at 45 degrees to the normal of the flake's surface. The radiation has a wavelength of 4 mm. The discontinuity in the solid line is discussed in Section 5.1.

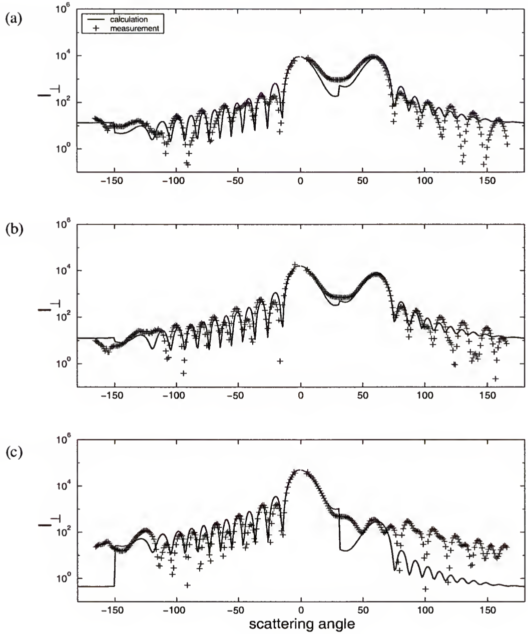

Figure 46: Comparison of the scattering model (solid line) with microwave data (crosses). Plots a – c show the scattering by acrylic flakes 6-8 described in Table 1. The light is incident at 30 degrees to the normal of the flake's surface. The radiation has a wavelength of 4 mm and is polarized perpendicular to the scattering plane. The discontinuity in the solid line is discussed in Section 5.1.

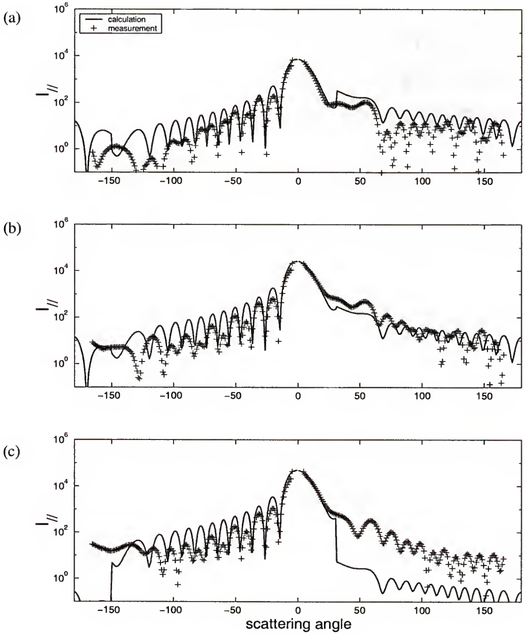

Figure 47: Same as Figure 46 except that the radiation is polarized parallel to the scattering plane. The scattering model (solid line) is compared with microwave data (crosses). Plots a – c show the scattering by acrylic flakes 6-8 described in Table 1. The light is incident at 30 degrees to the normal of the flake's surface. The radiation has a wavelength of 4 mm. The discontinuity in the solid line is discussed in Section 5.1.

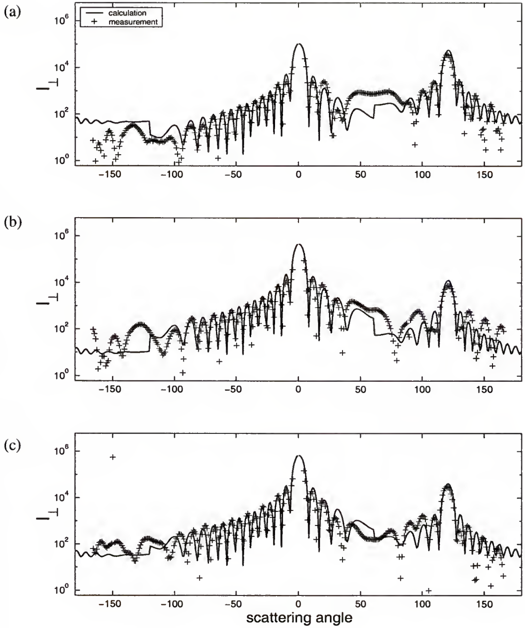

Figure 48: Comparison of the scattering model (solid line) with microwave data (crosses). Plots a – c show the scattering by acrylic flakes 6-8 in Table 1. The light is incident at 60 degrees to the normal of the flake's surface. The radiation has a wavelength of 2.7 mm and is polarized perpendicular to the scattering plane. The discontinuity in the solid line is discussed in Section 5.1.

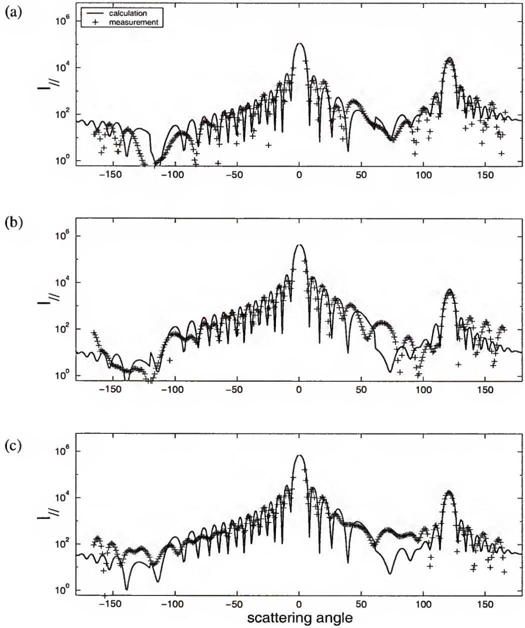

Figure 49: Same as Figure 48 except that the radiation is polarized parallel to the scattering plane. The scattering model (solid line) is compared with microwave data (crosses). Plots a – c show the scattering by acrylic flakes 6-8 in Table 1. The light is incident at 60 degrees to the normal of the flake's surface. The radiation has a wavelength of 2.7 mm. The discontinuity in the solid line is discussed in Section 5.1.

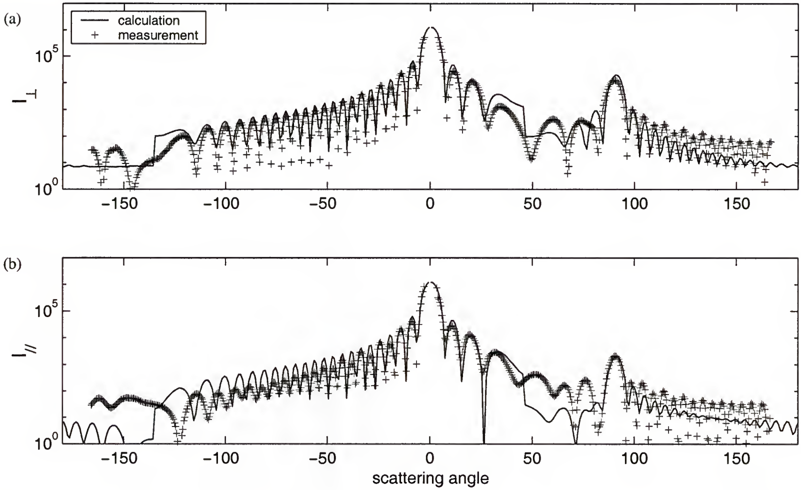

Figure 50: Comparison of the scattering model (solid line) with microwave data (crosses) for Bk7 glass flake 1 (described in Table 1) with the light incident at 45 degrees to the normal of the flake's surface. The radiation has a wavelength of 2.7 mm and is polarized perpendicular (a) and parallel (b) to the scattering plane. The discontinuity in the solid line is discussed in Section 5.1.

5.2 Average over Rotation

The previous section showed examples of how theoretical predictions using our scattering model compare to experimental data for a number of different flakes in various fixed orientations. To test the model over a wide range of orientations, this section will present comparisons between calculated and measured scattering properties averaged over the rotation of a test flake. For each test case, shown in Figure 51 through Figure 60, the compared scattering properties are (i) the total intensity, (ii) the polarization at two different wavelengths, (iii) the color $(I_{red} - I_{blue})/(I_{red} + I_{blue})$, and (iv) the polarimetric color $(P_{red} - P_{blue})$. Color and polarimetric color are measures of the relative difference in intensity and polarization of the scattered light at a longer and a shorter wavelength, here referred to as red and blue, respectively. Color and polarimetric color are measures that are commonly used as diagnostic tools for investigating light scattering properties of small particles (Kolokolova et al., 1997). Here, we use color and polarimetric color (together with intensity and polarization) as diagnostic tools to evaluate our scattering model. Again, tests were carried out with both Bk7 glass and acrylic flakes. The dimensions vary between 0.043 λ and 0.246 λ in thickness and between 3.18 λ and 25.4 λ in width. The reference of the flake used in a particular comparison is indicated in the figure caption and more details about the physical properties of the flake are found in Table 2.

Although there are structures in the measurements that are not reproduced in the modeling, the overall agreement is remarkably good in most of the test cases. Relative measures such as polarization, color and polarimetric color show the right trends in all test cases, even in the case of flake 14 with a width of 3.18 λ (Figure 55). As expected, the accuracy of the model worsens for smaller aspect ratios, as exemplified by flake 12, which has an aspect ratio of 17 (Figure 58). However, the correct trends are still visible in the prediction by the model. We conclude that our model, in general, offers a good approximation of the scattering by a flake when the large dimensions of the flake are greater than 6 λ and the aspect ratio exceeds 25.

Surprisingly, the largest discrepancy in polarization (seen more clearly in polarimetric color plots) is found for scattering by the thinnest flakes of both Bk7 glass and acrylic, i.e. flake 13 and flake 19 (Figure 54 and Figure 60). The mechanism for this, which apparently becomes important when the flake becomes very thin in terms of the wavelength, is not yet understood. The structure seen in the polarization in the experimental scattering data of flake 19 is confirmed by a comparison with DDA calculations in Section 5.4.

Table 2: Data for the flakes used in the test simulations, modeling the light scattering averaged over the rotation of the flake.

Flake	Figure	Refractive Index m	Large Dimensions width×height [λ (4mm)]	Thickness [λ (4mm)]	Aspect Ratio	Size Parameter* x
10	50	$2.52 - i0.030$	12.7×12.7	0.246	52	37.1
11	51	$2.52 - i0.030$	6.35×6.35	0.218	29	16.5
12	52	$2.52 - i0.030$	6.35×6.35	0.144	44	10.9
13	53	$2.52 - i0.030$	6.35×6.35	0.043	148	3.25
14	54	$2.52 - i0.030$	3.18×6.35	0.144	22	7.69
15	55	$1.62 - i0.003$	25.4×12.7	0.381	67	40.7
16	56	$1.62 - i0.003$	12.7×12.7	0.378	34	57.1
17	57	$1.62 - i0.003$	6.35×12.7	0.377	17	40.3
18	58	$1.62 - i0.003$	6.35×12.7	0.250	25	26.7
19	59	$1.62 - i0.003$	6.35×12.7	0.125	51	13.3

* Surface-equivalent sphere size parameter

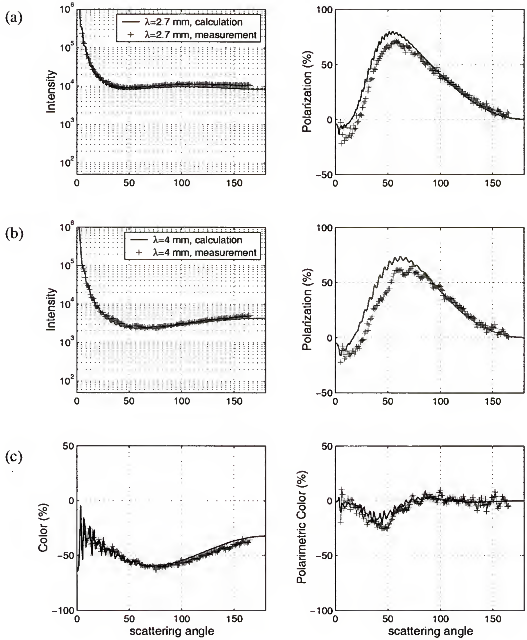

Figure 51: Comparison between theoretical calculations using our scattering model (solid line) and microwave data (crosses). The scattering is averaged over rotation for Bk7 glass flake 10 described in Table 2. a) total intensity and polarization with wavelength 2.7 mm; b) total intensity and polarization with wavelength 4 mm; c) corresponding color and polarimetric color.

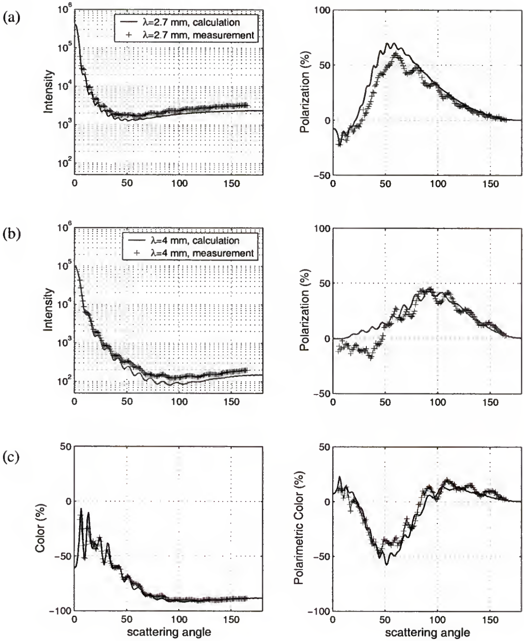

Figure 52: Comparison between theoretical calculations using our scattering model (solid line) and microwave data (crosses). Scattering properties averaged over rotation for Bk7 glass flake 11 described in Table 2. a) total intensity and polarization with wavelength 2.7 mm; b) total intensity and polarization with wavelength 4 mm; c) corresponding color and polarimetric color.

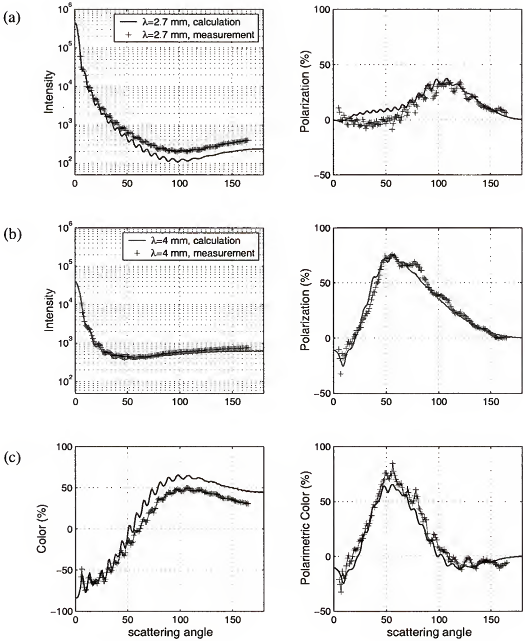

Figure 53: Comparison between theoretical calculations using our scattering model (solid line) and microwave data (crosses). The scattering is averaged over rotation for Bk7 glass flake 12 described in Table 2. a) total intensity and polarization with wavelength 2.7 mm; b) total intensity and polarization with wavelength 4 mm; c) corresponding color and polarimetric color.

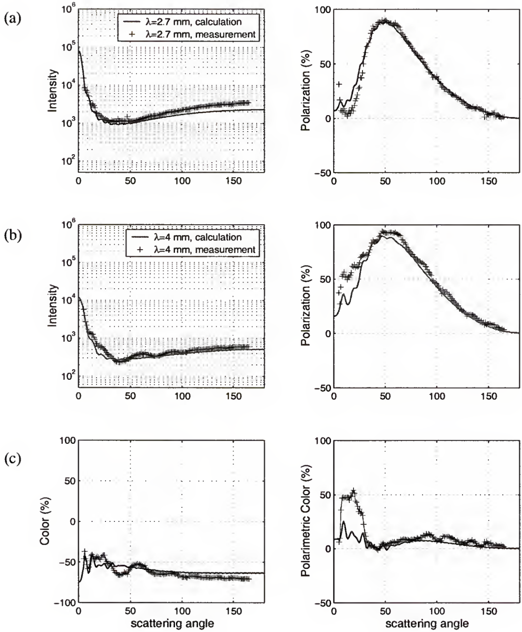

Figure 54: Comparison between theoretical calculations using our scattering model (solid line) and microwave data (crosses). The scattering is averaged over rotation for Bk7 glass flake 13 described in Table 2. a) total intensity and polarization with wavelength 2.7 mm; b) total intensity and polarization with wavelength 4 mm; c) corresponding color and polarimetric color.

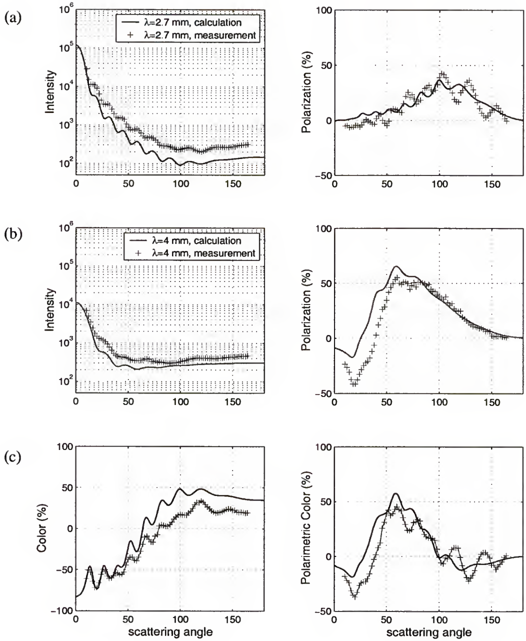

Figure 55: Comparison between theoretical calculations using our scattering model (solid line) and microwave data (crosses). The scattering is averaged over rotation for Bk7 glass flake 14 described in Table 2. a) total intensity and polarization with wavelength 2.7 mm; b) total intensity and polarization with wavelength 4 mm; c) corresponding color and polarimetric color.

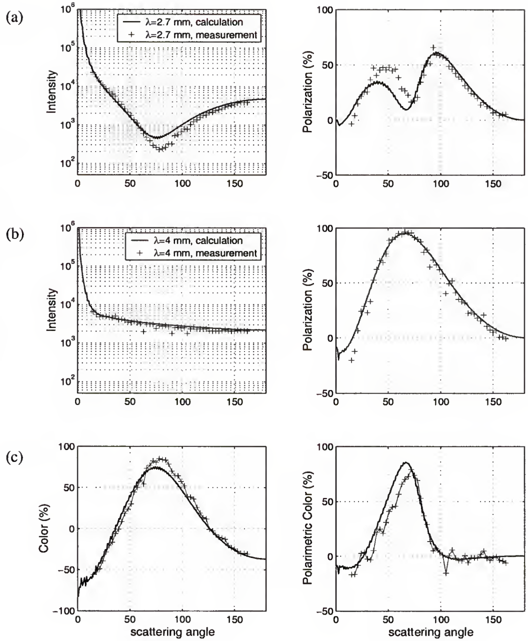

Figure 56: Comparison between theoretical calculations using our scattering model (solid line) and microwave data (crosses). The scattering is averaged over rotation for acrylic flake 15 described in Table 2. a) total intensity and polarization with wavelength 2.7 mm; b) total intensity and polarization with wavelength 4 mm; c) corresponding color and polarimetric color.

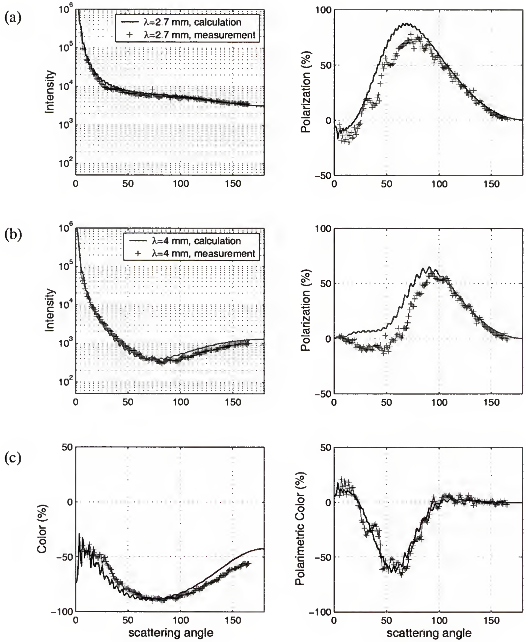

Figure 57: Comparison between theoretical calculations using our scattering model (solid line) and microwave data (crosses). The scattering is averaged over rotation for acrylic flake 16 described in Table 2. a) total intensity and polarization with wavelength 2.7 mm; b) total intensity and polarization with wavelength 4 mm; c) corresponding color and polarimetric color.

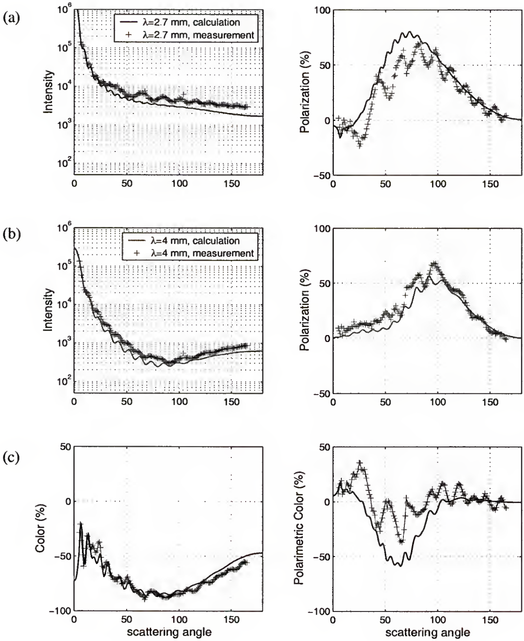

Figure 58: Comparison between theoretical calculations using our scattering model (solid line) and microwave data (crosses). The scattering is averaged over rotation for acrylic flake 17 described in Table 2. a) total intensity and polarization with wavelength 2.7 mm; b) total intensity and polarization with wavelength 4 mm; c) corresponding color and polarimetric color.

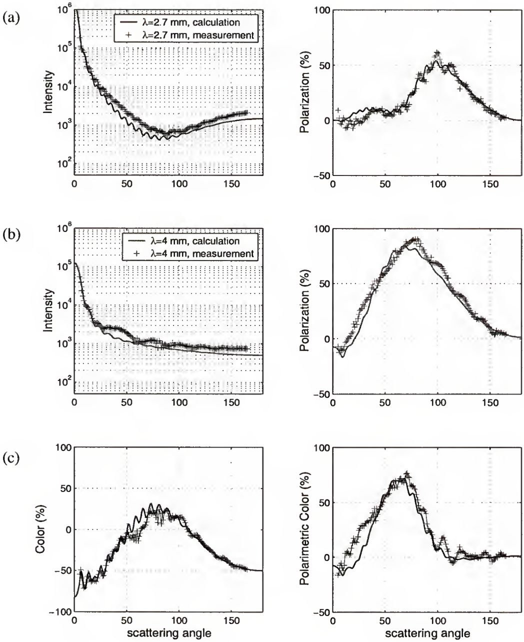

Figure 59: Comparison between theoretical calculations using our scattering model (solid line) and microwave data (crosses). The scattering is averaged over rotation for acrylic flake 18 described in Table 2. a) total intensity and polarization with wavelength 2.7 mm; b) total intensity and polarization with wavelength 4 mm; c) corresponding color and polarimetric color.

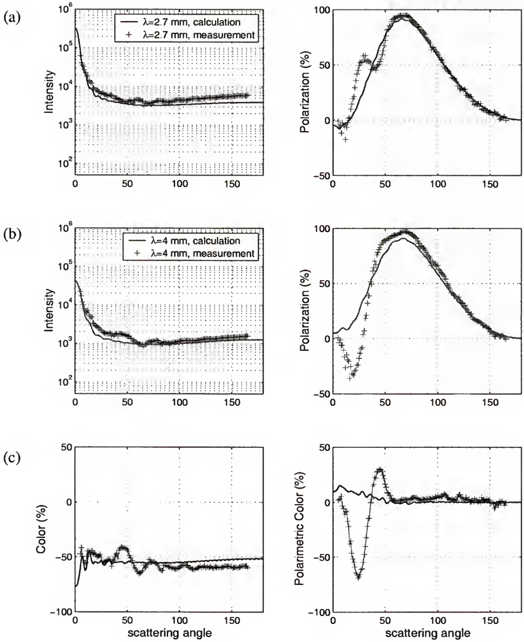

Figure 60: Comparison between theoretical calculations using our scattering model (solid line) and microwave data (crosses). The scattering is averaged over rotation for acrylic flake 19 described in Table 2. a) total intensity and polarization with wavelength 2.7 mm; b) total intensity and polarization with wavelength 4 mm; c) corresponding color and polarimetric color.

5.3 Scattering Model in the Geometrical Optics Regime

In this section, our scattering model is compared to geometrical optics (GO). It is expected that the scattering by a flake much larger than the wavelength in extent will be described relatively well by the GO approach, and the larger the flake, the better the GO description will be. Our scattering model is developed within the premise of GTD and, as an extension of the GO, the method is expected to be more accurate the larger the scatterer is.

With our scattering model we are able to simulate the scattering by flakes as small as a few wavelengths in size as well as large flakes in the GO regime. A set of theoretical predictions of the polarization averaged over rotation, for a square flake with increasing large dimensions and constant thickness, are calculated and plotted in Figure 61 through Figure 63. At the small end, comparison is made to microwave measurements and at the large end, comparison is made to the geometrical optics solution. These comparisons illustrate how our model, as expected, approaches the geometric optics approximation for larger flakes. It is interesting to see how a characteristic minimum in the linear polarization curve develops in Figure 62 and Figure 63 as the large dimensions of the flake are increased. This minimum is due to interference effects, which consequently make the contribution from diffraction important also for large flakes. An example of this type of minimum in the polarization curve can be seen in Figure 55 in Section 5.2. Because of the higher absorption in the Bk7 glass flake, the interference effects are not as pronounced (Figure 61) as in the case of the relatively transparent acrylic flakes. Interference effects are further discussed and investigated in Chapter 6.

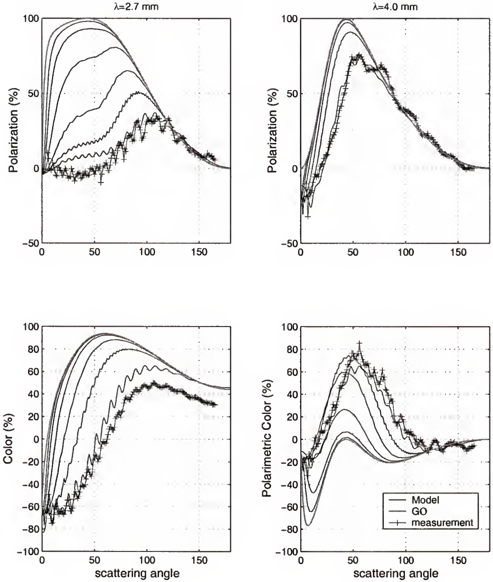

Figure 61: Set of graphs illustrating how the polarization at two different wavelengths (2.7 mm and 4 mm), color and polarimetric color change as the flakes are made wider and eventually approach the geometric optics approximation. The different solid lines show the result of the scattering model for flakes with respective widths of 6.35, 30, 120, 600, 3000 and 12000 λ. The gray line is the geometric optics approximation and the crosses the microwave data for a 6.35 λ wide flake. In this case the flake is 0.144 λ thick and made of Bk7 glass ($m = 2.52 - i0.03$).

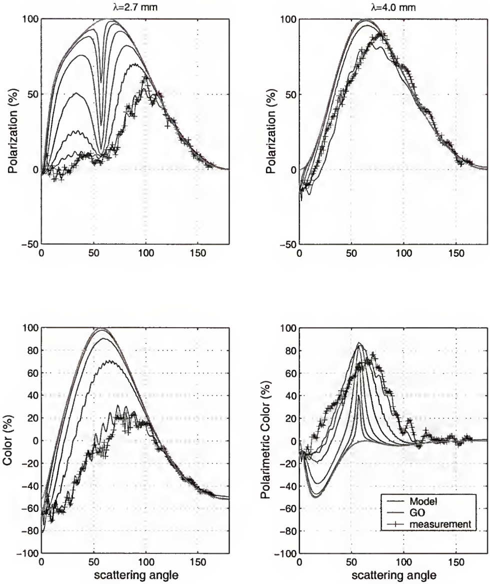

Figure 62: Set of graphs illustrating how the polarization at two different wavelengths (2.7 mm and 4 mm), color and polarimetric color change as the flakes are made wider and eventually approach the geometric optics approximation. The different solid lines show the result of the scattering model for flakes with respective widths of 6.35, 30, 120, 600, 3000 and 12000 λ. The gray line is the geometric optics approximation and the crosses the microwave data for a 6.35 λ wide flake. In this case the flake is 0.25 λ thick and made of acrylic ($m = 1.62 - i0.003$).

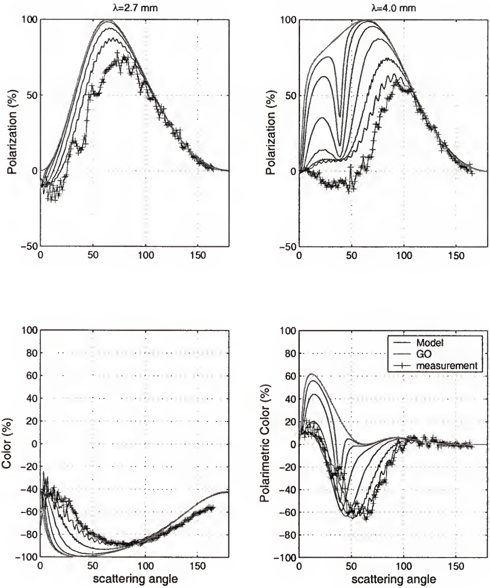

Figure 63: Set of graphs illustrating how the polarization at two different wavelengths (2.7 mm and 4 mm), color and polarimetric color change as the flake is made wider and eventually approach the geometric optics approximation. The different solid lines show the result of the scattering model for flakes with respective widths of 6.35, 30, 120, 600 3000 and 12000 λ. The gray line is the geometric optics approximation and the crosses the microwave data for a 6.35 λ wide flake. In this case the flake is 0.378 λ thick and made of acrylic ($m = 1.62 - i0.003$).

5.4 Comparison to DDA

In this section, the discrete dipole approximation (DDA) method is employed to numerically simulate a few of the test measurements of the scattering by the acrylic flakes presented in the previous sections. The purpose of this comparison is twofold. First, it serves as an additional check of the microwave measurements, in particular that the averaging over rotation is carried out correctly in the laboratory. Second, it is of interest to compare the computing time required for the DDA calculations to the time necessary to calculate the same scattering properties using our scattering model.

The DDA, also referred to as the coupled dipole approximation (Purcell and Pennypacker, 1973), is a flexible numerical method for calculating the scattering of electromagnetic waves by objects with arbitrary geometrical shape. The method was developed further by Draine (1988), Draine and Goodman (1993), and recently reviewed by Draine and Flatau (1994) and Draine (1999). The DDA technique allows an arbitrarily shaped particle to be represented by an array of a certain number of interacting dipoles on a cubic lattice grid. Each dipole radiates a field in response to the incident field and to the fields radiated by all other dipoles in the array. The DDA computations presented here have been carried out using the DDSCAT.5a10 code provided by Draine and Flatau. The details of the code can be found in the User Guide by Draine and Flatau (2000).

Figure 64 through Figure 66 show that the microwave data and DDA calculations for the flakes 1-3 listed in Table 3 (same as flakes 17-19 in Section 5.2) are in excellent agreement. The structures in the polarization, color and polarimetric color curves are reproduced relatively well. We thus conclude that the laboratory measurements averaged over the rotation of the flake are accurate. The CPU time required for the computations on an Alpha Station equipped with 2 CPU (each 1300 MIPS) and a total of 4 Gb RAM is given in hours in Table 3. Attempts were also made to calculate the scattering by flake 11 in the previous Section 5.2, which has the dimensions 12.7 $\lambda \times 12.7 \lambda \times 0.378 \lambda$. However, the estimated computer time that would be required was about 1200 hours, and the computations were stopped. In contrast, the theoretical predictions by our scattering model for the same flakes (presented in Section 5.2 as Figure 58 through Figure 60) required each 0.5 hours of CPU time on a 450 MHz Pentium III desktop computer.

Table 3: Data for the DDA simulations of acrylic flakes with different thickness. A value of $|m|kd$ of less than 0.5 is a validity criterion which ensures accurate DDA calculations (Draine and Flatau, 2000). This criterion makes certain the lattice spacing d is small compared to the wavelength within the material. (*k* is the free space wave number)

Flake/ Figure	Refractive Index m	Large Dimension width×height [λ (4mm)]	Thickness [λ (4mm)]	$\|m\|kd$ λ (4 mm)/ λ (2.7 mm)	CPU Time (h) λ (4 mm)/ λ (2.7mm)
1/ 63	1.62 – i0.003	6.35×6.35	0.377	0.384/ 0.569	57/ 118
2/ 64	1.62 – i0.003	6.35×6.35	0.250	0.363/ 0.538	30/ 81
3/ 65	1.62 – i0.003	6.35×6.35	0.125	0.253 0.376	39/ 140

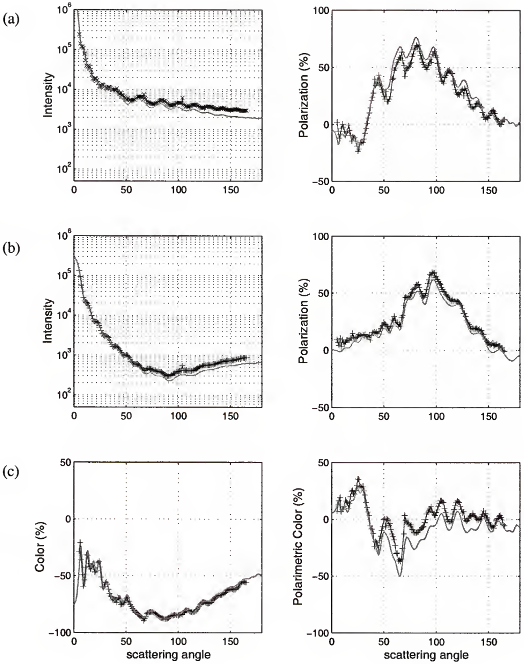

Figure 64: Microwave measurements (crosses) compared with DDA calculations (solid line); a) total intensity and polarization with wavelength 2.7 mm; b) total intensity and polarization with wavelength 4 mm; c) corresponding color and polarimetric color.

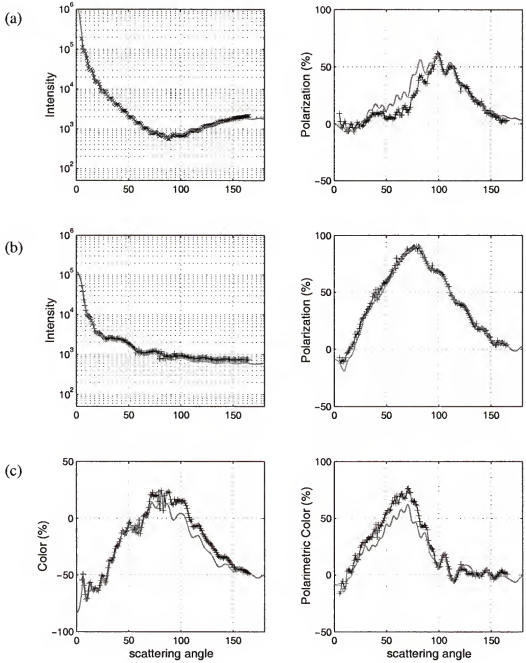

Figure 65: Microwave measurements (crosses) compared with DDA calculations (solid line); a) total intensity and polarization with wavelength 2.7 mm; b) total intensity and polarization with wavelength 4 mm; c) corresponding color and polarimetric color.

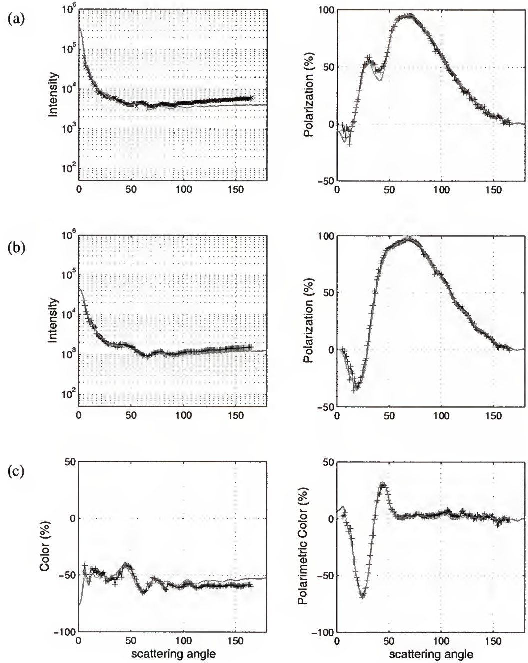

Figure 66: Microwave measurements (crosses) compared with DDA calculations (solid line); a) total intensity and polarization with wavelength 2.7 mm; b) total intensity and polarization with wavelength 4 mm; c) corresponding color and polarimetric color.

5.5 Shape Dependence

In this section, we examine how the shape of the flake affects its scattering properties when the overall size of the flake is in the order of a few wavelengths. The theoretical predictions by our scattering model are compared to microwave measurements of the scattering by thin circular disks, with the objective to find out if, or to what extent, we may use our scattering model to deduce scattering properties of flakes of various shapes.

In the geometric optics approximation, when diffraction is neglected, the shape of the flake will only have an influence on the intensity of the scattered light. The intensity is then basically proportional to the square of the cross section area (the large surface area). However, when flakes are small and diffraction contributes a significant amount to the scattered light, the shape will matter. Ksienski and Senior (1985) found that the shape of small (compared to the wavelength), thin dielectric flakes becomes important when either the thickness of the flake or the permittivity is increased. Furthermore, scattering by flakes of concave shape may appear different from the scattering by convex shaped flakes. For example, a "Figure-eight"-shaped flake formed by connecting two identical circular disks may show scattering properties more similar to the scattering by the individual disks than to the scattering of convex shaped flake with the same surface area. An analogous result is found in the case of porous aggregates, whose scattering properties to a large degree may be similar to the scattering properties of the constituent particles (Gustafson and Kolokolova, 1999).

In Figure 67 through Figure 69, the results of our scattering model are compared to a set of microwave measurements of the scattering by thin circular flakes with increasing diameter as described in Table 4. Our scattering model, which is based on the scattering by a rectangular flake, is only adjusted by a weight factor, determined by the difference in cross section area between the circular and rectangular flake. In all three cases, the model predicts the general trends of the scattering properties. Moreover, as expected, the models ability to describe the properties of the scattered light appears to improve with increasing dimensions (compare polarization, color and polarimetric color in Figure 67 through Figure 69).

We conclude that our model may be used to infer general trends in light scattering properties of circular flakes with a diameter larger than 6 wavelengths. Also, despite the limited number of shapes investigated, we believe that the model, with some caution, can be used to describe the scattering properties of flakes with other convex shapes.

Table 4: Data for the circular disks used in the test simulations, modeling the scattered light averaged over the rotation of the flake.

Circular Flake	Figure	Refractive Index *m*	Diameter [λ (4mm)]	Thickness [λ (4mm)]	Aspect Ratio	Size Parameter* *x*
1	66	1.62 –*i*0.003	6.35	0.380	17	15.7
2	67	1.62 –*i*0.003	12.7	0.380	33	31.5
3	68	1.62 –*i*0.003	25.4	0.380	67	58.1

* Surface-equivalent sphere size parameter

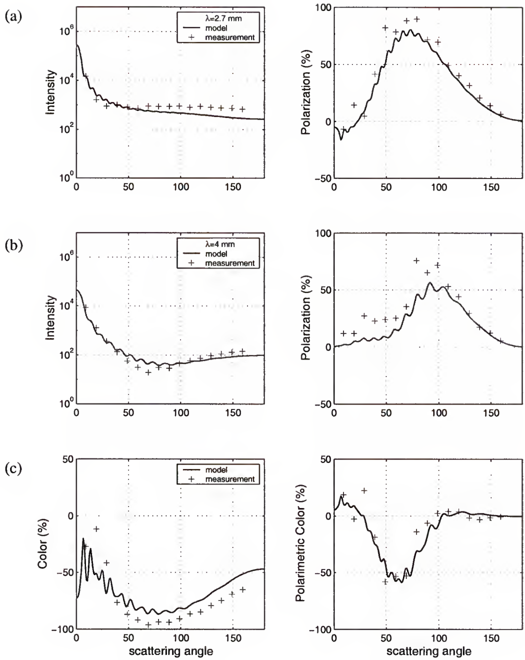

Figure 67: Comparison between theoretical calculations using our scattering model (solid line) and microwave data (crosses). Scattering properties averaged over rotation for circular flake 1 described in Table 4. a) total intensity and polarization with wavelength 2.7 mm; b) total intensity and polarization with wavelength 4 mm; c) corresponding color and polarimetric color.

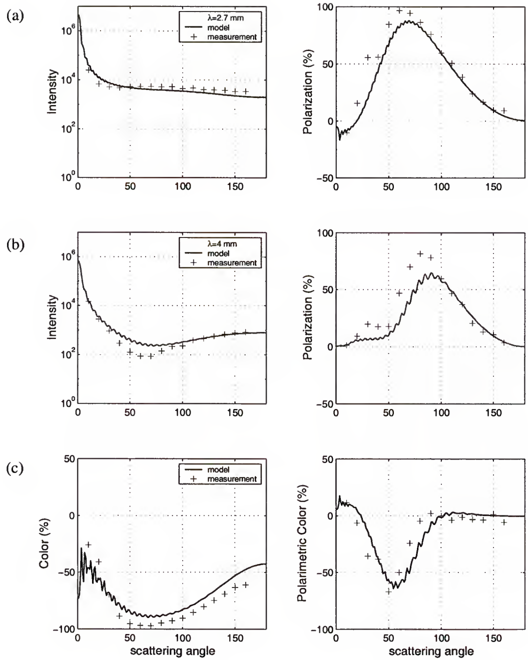

Figure 68: Comparison between theoretical calculations using our scattering model (solid line) and microwave data (crosses). Scattering properties averaged over rotation for circular flake 2 described in Table 4. a) total intensity and polarization with wavelength 2.7 mm; b) total intensity and polarization with wavelength 4 mm; c) corresponding color and polarimetric color.

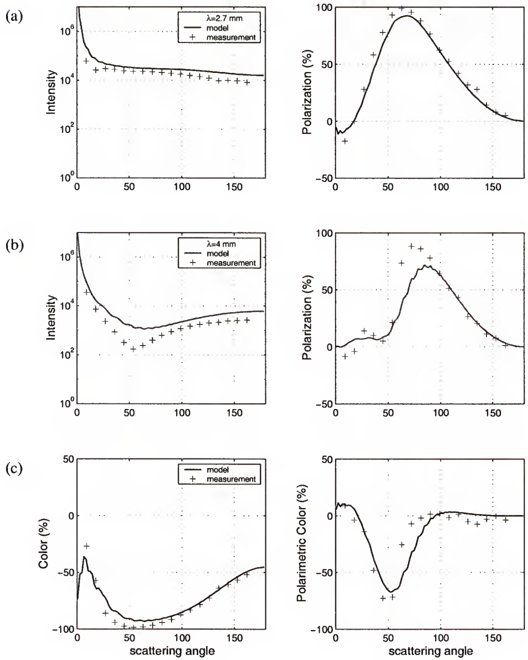

Figure 69: Comparison between theoretical calculations using our scattering model (solid line) and microwave data (crosses). Scattering properties averaged over rotation for circular flake 3 described in Table 4. a) total intensity and polarization with wavelength 2.7 mm; b) total intensity and polarization with wavelength 4 mm; c) corresponding color and polarimetric color.

5.6 Average over Rotation versus Average over Random Orientation

In a dust cloud where the particles have no preferred orientation (e.g., due to magnetic fields) the particles are often assumed to be randomly oriented. To simulate the light scattering properties for such a collection of particles, the scattered light is generally averaged over a uniform distribution of orientations. In this section, an experimental study by Waldemarsson and Gustafson (2000) is extended and used to discuss the possibility of deducing light scattering characteristics of randomly oriented flakes, by looking at the scattered light averaged over the rotation of the flake, given by our scattering model.

With the objective of investigating the light scattering properties of randomly oriented silicate flakes at visual wavelengths, Waldemarsson and Gustafson (2000) carried out a systematic study of the scattering by a circular flake using analog-to-light microwave measurements. With a refractive index, $m = 1.62 - i0.003$, acrylic was used as an analog material for the silicate flake. Machined with a diameter of 12.7 λ and a thickness of 0.38 λ, the circular acrylic flake was used to simulate the scattering by a silicate flake with an 8 μm diameter and a 0.25 μm thickness in the visual region. The scattering was averaged over a relatively uniform distribution of orientations in order to simulate randomness. In this section, the study has been extended to include more orientations. The simulation of the light scattering by a randomly oriented circular flake was carried out in the laboratory in the following manner. The scattering averaged over rotation (also referred to as the rotational average) was measured as described in Chapter

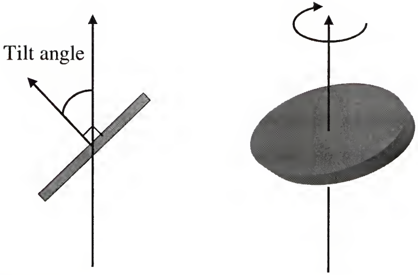

Figure 70: Illustration of the tilt angle and rotation about the spin axis.

3. The tilt angle, which is the angle between the normal to the surface of the flake and the spin axis (Figure 70), was varied in increments of 10 degrees in the range between 10 and 80 degrees. Between 80 and 90 degrees tilt angle, the variation increment was reduced to 2 degrees to account for the rapid intensity change near the 90 degrees tilt angle, as this average includes the specular reflection. Each rotational average was properly weighted according to the step size and tilt angle. The measurements between 80 and 90 degrees tilt angle, with the variation increment of 2 degrees, are the ones here added to the first set of measurements reported by Waldemarsson and Gustafson (2000). However, these additional measurements, only marginally influence the averaged scattering properties.

In order to analyze the dependence on the kind of distribution of orientations used in a particular average, the measurements are divided up in three different distributions of orientations and the data is further reduced in two wavelength intervals, 2.7-3 mm and 3.5-4 mm, corresponding to blue and red at visual wavelengths. Figure 71 shows the intensity and polarization of the scattered light averaged (i) over a uniform distribution of orientations, (ii) over rotation including only tilt angle 90 degrees (i.e., the rotational average which includes the specular reflection), and (iii) averaged over tilt angles 10 to 80 degrees, hence excluding the contribution from the specular reflection. One can see, that the average simulating the scattering by randomly oriented flakes is dominated by the contribution from the specular reflection. The intensity and polarization levels are lower, but the spectral and polarimetric dependencies on scattering angle are found, for the most part, to be similar to those of the average over rotation. That is, the scattered light in the blue waveband has a higher intensity than in the red, thus indicating blue color. For scattering angles smaller than 90 degrees, the polarimetric color is blue (i.e., the polarization is greater in the blue waveband than in the red). It is further found that if the specular reflections are excluded in the average, the scattering characteristics are much different. Of course, the intensity levels are much lower and although the color is still blue for most scattering angles, this dependence is much weaker and the polarimetric color at smaller scattering angles has changed to red.

We conclude that the scattering averaged the over rotation of the flake, if the specular reflection is included, may give an indication of the relative scattering properties, such as polarization, color and polarimetric color, of randomly oriented flakes. The example above also illustrates, that randomly orientated flakes and flakes that are aligned in some preferred orientation(s), might be distinguishable based on their different scattering properties.

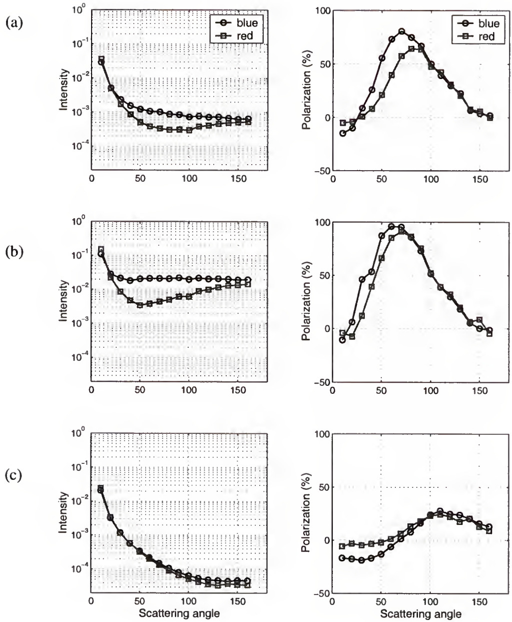

Figure 71: Comparison of the angular dependence of the intensity and polarization of the scattered light by a thin flake with a 12.7 λ diameter, a 0.38 λ thickness and refractive index $m = 1.62 - i0.003$, averaged over three different distributions of orientations. a) average over a uniform distribution of orientations simulating randomness; b) average over rotation with the tilt angle kept at 90 degrees; c) averaged over rotation excluding the contribution from specular reflection. Squares and circles represent data for red and blue wavebands, respectively. The solid lines are only connecting the data points as a visual aid.

5.7 Summary

To investigate the extent of validity of our approximate model for the scattering by thin dielectric flakes, a number of comparisons with laboratory microwave measurements were made. The predictions of our scattering model are in good agreement with the experimental data, when the large dimensions of the flake are greater than 6 λ and the aspect ratio exceeds 25. This is true, both in the case of the scattering by a flake in fixed orientation, and in the case when the scattering was averaged over the rotation. It was shown, that as the dimensions of the flake are increased, the result of our scattering model approaches the geometric optics approximation. If interference is taken into account, it is shown that diffraction can be important also for relatively large flakes. In particular, a deep characteristic minimum (or set of minima, depending on thickness) may develop as the large dimensions of the flake are increased. When the experimental data was compared to the results of the DDA calculations, it was shown that the fine structure seen in the measurements were reproduced by the DDA calculations. Thus, we are assured that the average over rotation is measured correctly in the laboratory.

To assess if our model can be used to deduce light scattering properties of flakes in general, we examined the dependence on the shape as well as on the distribution of orientations. We found that, albeit with some caution, the model may be used to infer scattering properties, not only for rectangular flakes, but also in the case of other convex shapes, as long as proper weight is taken to account for the cross section area of the flake. With regard to the distribution of orientations, we found that the properties of the scattered light averaged over rotation computed with our model, offer a good approximation of the scattering properties of randomly oriented flakes

CHAPTER 6
LIGHT SCATTERING PROPERTIES OF FLAKES

In this chapter, our scattering model for flakes is applied to investigate the properties of the light scattered by flakes. In Chapter 5, the scattering model was found to be in good agreement with microwave scattering experiments as long as the large dimensions (width and height) of the flake are larger than 6 wavelengths and the aspect ratio of the flake is at least 25, i.e. the large dimensions of the flake are at least 25 times its thickness. It was also shown that when the larger dimensions of the flake are increased, the shape of the flake has less influence on the scattering, and our scattering model approaches the geometric optics approximation.

Throughout this chapter we look at the dependence of the rotational average of the scattering on the scattering angle. The rotational average is the average of the scattered light as the flake is rotated in such a way that the normal to its surface is in the scattering plane. This rotational average was used to assess our scattering model in Chapter 5, and it was also found to give a good approximation of the light scattering properties of randomly oriented flakes. The scattering by randomly oriented flakes is of interest when studying a large collection of non-aligned flakes.

6.1 Intensity and Polarization

In this section we explore how the angular dependence of the intensity and linear polarization vary as a function of thickness, large dimensions (width and height) and refractive index of the flake. We also examine the case of having poly-disperse flakes, in particular in regard of the thickness, which will be shown being the dimension that influence the scattering the most. In order to study poly-dispersion we take an average over a thickness distribution, corresponding to the scattered light from a collection of particles with a varying thickness.

6.1.1 Dependence on the thickness

In Figure 72, the rotational average of the intensity and polarization of the scattered light by a transparent square flake (with a side of 120 wavelengths and refractive index $m = 1.62$) is plotted as a function of scattering angle and thickness. As expected, the intensity is peaked in the forward direction and when the flake is thin, the polarization is found to be positive with a the maximum determined by the Brewster angle, for which the reflected field of the parallel polarization has a minimum. As the thickness of the flake is increased, a periodic structure in both intensity and polarization, as a function of thickness, is found. Examples of profiles of the intensity and polarization for a certain thickness can be seen in Figures 50 – 59 in Section 5.2. The periodic structure of minima, in an otherwise rather flat intensity at larger scattering angles, is a consequence of destructive interference between the field reflected off the external surface and the field that is transmitted after internal reflections. A consequence of the reduction in intensity is that the contribution of the diffracted field becomes more important. While the reflected field components of perpendicular and parallel polarization are equally reduced by the destructive interference, the diffracted fields are not affected. Thus, since the diffracted fields of perpendicular and parallel polarization are of the same order of magnitude, the polarization of the scattered light is reduced, thereby producing the cyclic structure of minima seen in the linear polarization (Figure 72). Hence, as an indirect effect of the destructive interference, a minimum or a number of minima may develop in the angular polarization function. It may also appear as if the maximum in polarization is shifted away from the scattering angle corresponding to the Brewster angle. Examples of this have been shown in the comparison with microwave scattering data in Section 5.2.

The largest effect of destructive interference occurs when the phase shift due to the difference in optical path length between the externally and internally reflected fields is an integer number of 2π. The thickness of the flake, d, when this is the case, can be found from equations (4- 18) to (4- 20) in Chapter 4, and expressed as

$$d = q \cdot \frac{\lambda}{2m}\left(\frac{\cos\theta_{t1}}{1-\sin^2\theta_{t1}}\right) = q \cdot \frac{\lambda_m}{2}\left(\frac{\cos\theta_{t1}}{1-\sin^2\theta_{t1}}\right) \tag{6- 1}$$

where q is a positive integer, θ_{t1} is the angle of refraction (Figure 33 in Chapter 4) and λ_m is the wavelength within the flake.

In Figure 73, the thickness, d, of the flake given by equation (6- 1) is plotted (white lines) together with the contours of the intensity and polarization from Figure 72. It is here shown that the periodic variation of the intensity and polarization are correlated and coincide with the thickness expressed in equation (6- 1). Note that, in Figure 73, the dependence on thickness is shown in units of the wavelength inside the flake, λ_m, in order to illustrate how, at 180 degrees scattering angle, a minimum in intensity occurs every multiple of $\lambda_m/2$.

As the flake is made thinner the intensity of the scattering will drop (Figure 74). Naturally, the limit of zero thickness is equivalent to having no flake present. In terms of externally and internally reflected field components, at the limit of zero thickness, the difference in phase between the fields is zero. Hence, due to the inherent 180 degrees phase difference between the external and internal reflection coefficients, the components

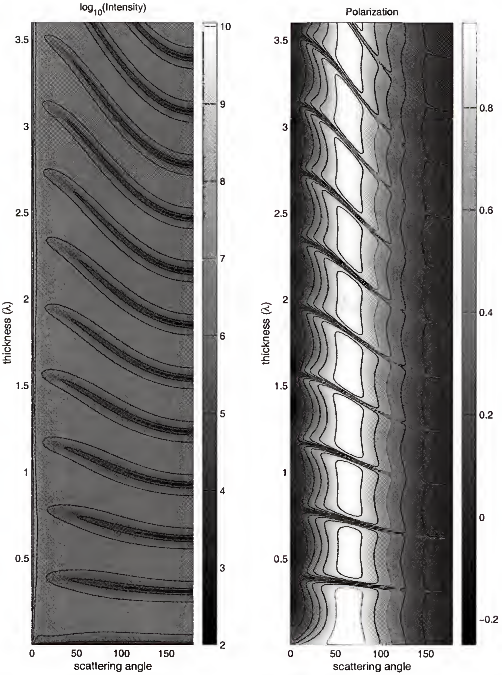

(a) (b)

Figure 72: Simulation of the rotational average of the light scattered by a square flake (with a side of 120 λ and refractive index m =1.62) as a function of scattering angle and thickness. a) intensity and b) polarization.

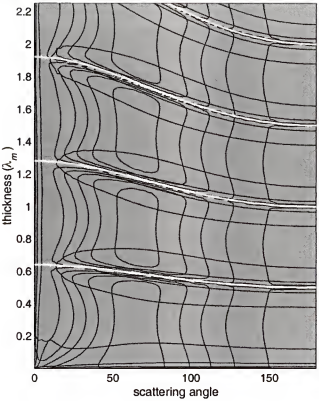

Figure 73: Contours of intensity and polarization from Figure 72 plotted on top of each other together with the thickness (given in equation 6-1) at which destructive interference occurs (white lines). The thickness is here given in units of the wavelength within the flake, λ_m, so as to illustrate how a minimum in intensity occurs every multiple of $\lambda_m/2$ at 180 degrees scattering angle.

will cancel each other when taking all internal reflections into account. Furthermore, in Figure 74, it also shown that the polarization maximum remains at the scattering angle corresponding to the Brewster angle.

6.1.2 Dependence on the large dimensions

The dependence of the scattering on the large dimensions (the width and height) of the flake is illustrated in Figure 75, where the intensity and polarization have been plotted as a function of thickness for a number of flakes with increasing large

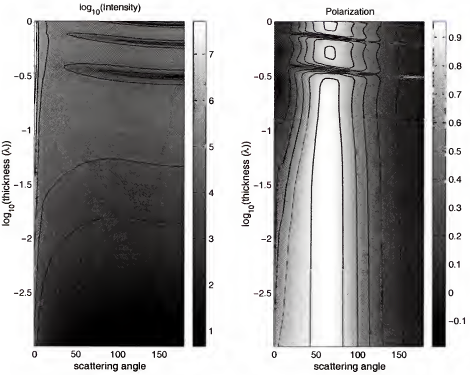

(a) (b)

Figure 74: Simulation of the light scattered by a square flake (with a side of 30 λ and m = 1.62) as a function of scattering angle and thickness (here shown in logarithmic scale) to illustrate how the intensity is reduced as the thickness approaches zero. a) intensity and b) polarization.

dimensions. In Figure 75a-e the flakes are squares with respective sides of 6.35 λ, 12.7 λ, 30 λ, 120 λ and 600 λ. For comparison, Figure 75f shows the result of geometric optics, which corresponds to a flake of infinite extent. The larger the large dimensions of the flake are, the less important the contribution from the diffracted fields become. In addition, because the intensity in the forward direction becomes more peaked, the region of scattering angles where the scattering is affected by diffraction decreases with increasing large dimensions. Consequently, the effect of destructive interference is seen at smaller scattering angles and the region of reduced polarization is smaller when the flake is larger.

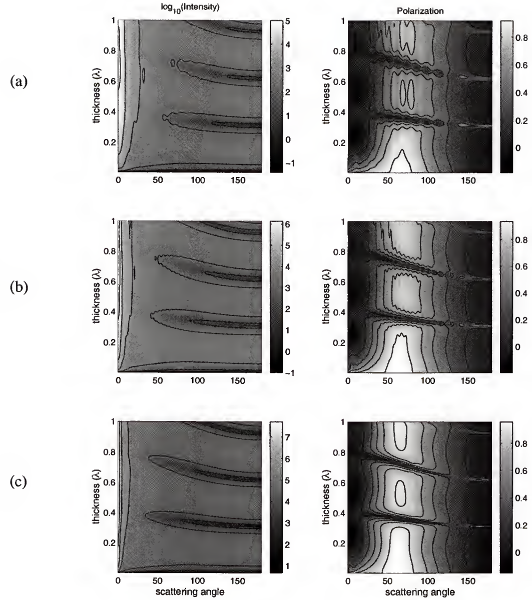

Figure 75: Simulations of the intensity (left column) and polarization (right column) of the light scattered by a square flake ($m = 1.62$) as a function of scattering angle and thickness. From a) to e) the flakes are squares with sides of 6.35 λ, 12.7 λ, 30 λ, 120 λ, and 600 λ, respectively. For comparison, f) shows the result of geometrical optics, corresponding to a flake of infinite extent. In the intensity plots one can see (i) how the intensity is more peaked in the forward direction (zero degree scattering angle) the larger the flake is and (ii) the larger the flake, the less important the contribution from diffraction in the forward direction. Thus, the effect of destructive interference is shown for smaller scattering angles. In the polarization plots, the periodic regions of low polarization are reduced in extent as the size of the flake is increased.

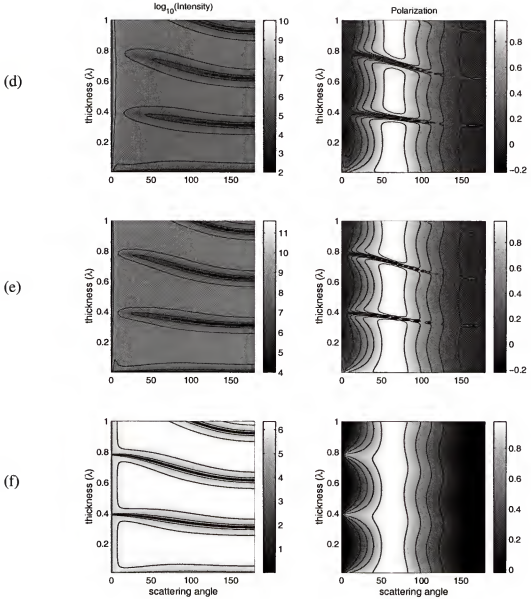

Figure 75 – continued.

6.1.3 Dependence on the refractive index

A change in the real part of the refractive index, *m*, affects the phase difference between the externally and internally reflected and transmitted fields in the same way a change in thickness of the flake does. In both cases the optical path length (the product of distance the light travels and refractive index) inside the flake is changed. Hence, the dependence on refractive index resembles the dependence on thickness. However, with a change in refractive index, the reflection and transmission coefficients are also affected.

Figure 76a and b show the intensity and polarization of the light scattered by a square flake (of thickness 0.25 λ and with the side 6.35 λ and 120 λ, respectively) as a function of refractive index (real part). For comparison, the results of geometrical optics, corresponding to a flake of the same thickness but with large dimensions infinite in extent, are displayed in Figure 76c. Because our scattering model is based on an impedance boundary condition solution, our model is not expected to yield accurate results as the refractive index approaches unity, and our approximation has only been tested for a refractive index of 1.62 on the low end. However, we note that, as seen in Figure 76a and b, the location of maximum polarization, P_{max}, is approaching 90 degrees as the refractive index approaches unity in a similar manner to the results of geometrical optics (Figure 76c).

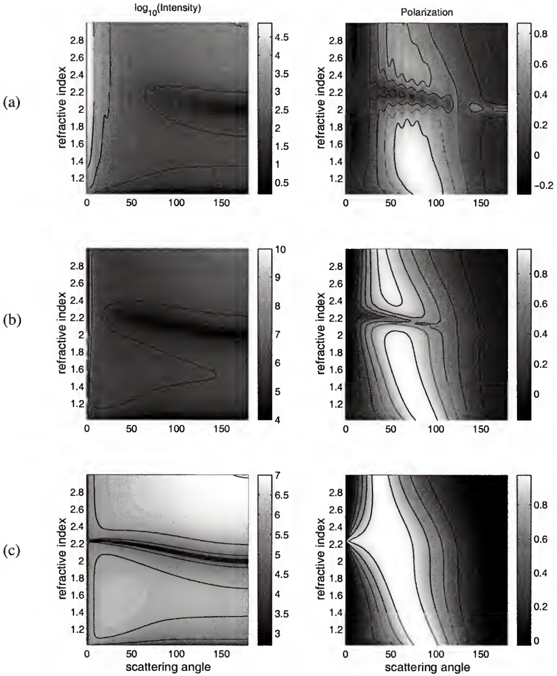

Figure 76: Simulation of the intensity (left column) and polarization (right column) of the light scattered by a square flake as a function of scattering angle and refractive index. In a) and b) the flakes are squares with the side 6.35 λ and 120 λ, respectively, and 0.25 λ thick. For comparison, c) shows the result of geometrical optics, which corresponds to a flake of infinite extent.

In the case of an absorbing flake (i.e. a flake with a refractive index with a non-zero imaginary part), the variations resulting from interference are reduced as part or all of the transmitted light is absorbed inside the flake. The amount of the transmitted light that is absorbed increases with the thickness of the flake. The effect of introducing absorption in the flake is illustrated in Figure 77, which shows the same simulation as the one in Figure 72, except that an imaginary part of 0.03 is added to the refractive index, i.e. $m = 1.62 - i0.03$. Comparing Figure 77 to Figure 72 we see that the periodic structure in intensity and polarization now are reduced with increasing thickness due to the resulting increase of absorption. Evidently, the larger the absorption is, the smaller the effects of interference will be.

6.1.4 Poly-dispersion

The examples presented above, show that although the variations in intensity and polarization caused by interference depend on the extent of the large dimensions of the flake, they do still remain to some degree, even as the large dimensions are taken to be much larger than the wavelength. On the other hand, if the thickness of the flake is changed, the properties of the scattering can change substantially. Thus, in the case of the scattering by poly-disperse flakes, i.e. a collection of particles with a varying thickness, the periodic structure in the intensity and polarization will be suppressed. The effect of this can be illustrated by averaging the scattering over a thickness distribution. In Figure 78, the data presented in Figure 72, have been averaged over a uniform thickness distribution of width 0.4 λ, and as a result most of the periodic structure in intensity and polarization, shown in Figure 72, has disappeared.

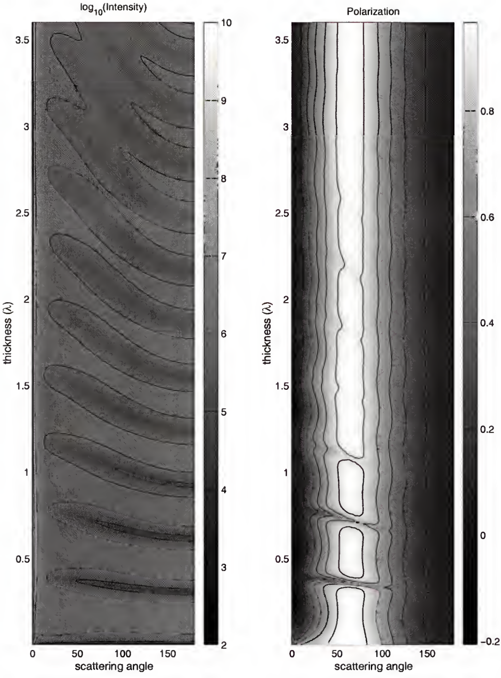

(a) (b)

Figure 77: Simulation of the intensity (a) and polarization (b) of the light scattered by a square flake (with a side of 120 λ and refractive index $m = 1.62 - i0.03$) as a function of scattering angle and thickness. Due to the absorption the effects of interference are reduced with increasing thickness (compare Figure 72).

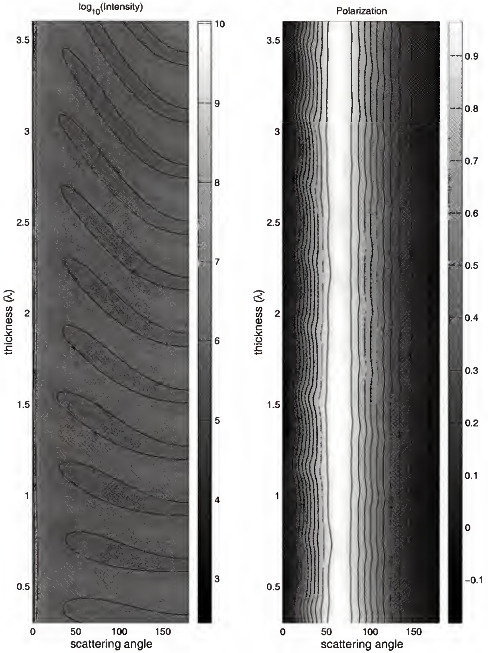

(a) (b)

Figure 78: Simulation of the intensity (a) and polarization (b) of the light scattered by a square flake (with a side of 120 λ and refractive index $m = 1.62$) as a function of scattering angle and thickness. Here the scattering is averaged over a uniform thickness distribution of width 0.4 λ and the effects of interference are suppressed (compare Figure 72).

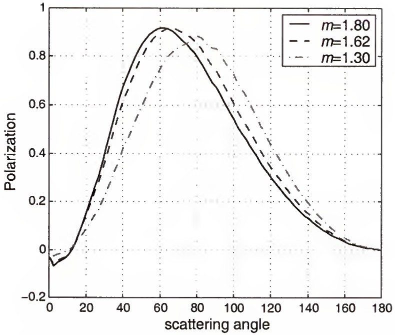

Figure 79: Linear polarization dependence on refractive index.

When the effects of interference are suppressed, either because of absorption or because of averaging the scattering over a thickness distribution, the linear polarization is relatively independent of flake thickness. The polarization function is found to have an asymmetric bell-shape with a maximum reaching close to 100% (Figure 79). As mentioned earlier, this polarization maximum, P_{max}, is located at the scattering angle for which the reflection of the parallel polarization has a minimum. Hence, as shown in Figure 79, the location of P_{max} is dependent on the real part of the refractive index, and the lower the refractive index is the closer the angular position of P_{max} will be to 90 degrees, which is the limit for a refractive index of one.

It is interesting to note that a linear polarization with a bell-like shape is a well-known property of Rayleigh scattering, i.e. scattering by particles much smaller than the wavelength. However, above it is shown that a bell-shaped polarization curve may also indicate flakes with dimensions larger than a wavelength. This polarization characteristic has also been noted by Zakharova and Mishchenko (2000,2001), for the scattering by wavelength-sized flakes and flake-like spheroids with large aspect ratios. Zakharova and Mishchenko (2000,2001) also note that for larger plates the maximum polarization is shifted from 90 degrees towards smaller scattering angles. We believe this shift can be explained by the fact that even in the case of wavelength-sized flakes, the scattering is determined to a large degree by surface scattering. As the large dimensions of the flake are made larger, the scattering becomes more dominated by the scattering from the large surfaces, and consequently dependent on the specular reflections.

6.2 Spectral Properties

From the interference effects seen in the intensity and polarization of the scattering by flakes, follows that the scattering is strongly wavelength dependent. This wavelength dependence can be exploited by comparing the scattering at various wavelengths. In particular color and polarimetric color may be useful diagnostic properties to look at. Color and polarimetric color, defined as $(I_{red} - I_{blue})/(I_{red} + I_{blue})$ and $(P_{red} - P_{blue})$, respectively, are gauges of the relative difference in intensity and polarization of the scattered light at a longer and a shorter wavelength or wavelength region, here referred to as red and blue, respectively. Color and polarimetric color were also among the compared scattering parameters in Chapter 5.

Figure 80 shows the rotational average of color and polarimetric color as a function of scattering angle and thickness. In this case the ratio of the longer and the shorter wavelength is 1.48, which corresponds to the wavelength difference between red and blue wavelengths in the visual. Because the underlying reason for the color and polarimetric color variations is interference, there is a correlation between them. This correlation is more pronounced at scattering angles 20 – 100 degrees, due to large changes in polarization at these angles. The strongest color variations are found at large scattering angles, close to back scattering, whereas the variations in polarimetric color take place at scattering angles 20 – 100 degrees, due to the just mentioned fact that this is where a large change in polarization may occur. The small variation in polarimetric color in the backscattering region is expected to disappear if the rotational average is extended to an average over random orientation, in which case the polarization is zero at both 0 and 180 degrees scattering angle.

We note that found is a possible property of the scattering by flakes, which is otherwise commonly found in the scattering by small particles, namely, blue color – another well-known property of Rayleigh scatterers.

6.3 The inverse Problem

It may be relatively straightforward to measure or to calculate the characteristics of the light scattered by a particle with known properties. On the other hand, to determine the properties of a particle by the way it scatters light is a rather difficult problem. This so-called *inverse problem* is the task we face when we want to monitor and investigate the physical properties of particles based on the way they scatter light. Based on simulations using our scattering model, our study of the light scattering characteristics of flakes has revealed a number of features that may be used to recognize flakes in a light scattering experiment.

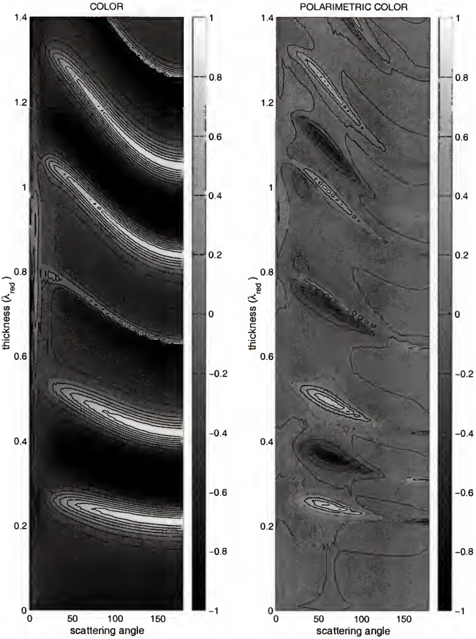

(a) (b)

Figure 80: Simulation of the color (a) and polarimetric color (b) of the light scattered by a square flake (with a side of 120 λ and refractive index $m = 1.62$) as a function of scattering angle and thickness. The ratio of the longer and the shorter wavelength is 1.48, corresponding to the wavelength difference between red and blue wavelengths in the visual.

Our scattering model is based on the fact that the scattering of flakes larger than a wavelength in extent is dominated by the scattering from the large surfaces. Although account is taken to diffracted fields, the scattering will be strongly directional, i.e. most light will be scattered in a narrow region around the forward direction and around the direction of specular reflection. Naturally, the larger the flake is the narrower these regions will be, in turn making it more difficult to successfully measure and analyze the scattered light by single flakes. However, if we can collect the light from a large number of flakes that may be assumed to be randomly oriented, the scattering is in effect averaged over a large number of orientations. In this case it may be possible to use the light scattering properties found with our model to recognize flakes.

Depending on the overall size of the flake the intensity will be more or less peaked in the forward direction while being relatively flat at larger scattering angles. The linear polarization curve resembles the polarization of Rayleigh scattering with a bell-like shape and a maximum polarization, P_{max}, of almost 100%. However, in contrast to Rayleigh scattering, the location of P_{max} is dependent on the refractive index (shifting towards smaller scattering angles with increasing refractive index).

In the case of transparent flakes with a narrow thickness distribution, interference effects make both intensity and polarization wavelength dependent, which in turn give rise to strong correlated variations in color and polarimetric color at scattering angles in the interval 20 – 100 degrees. Additionally, in the case of larger transparent flakes, deep minima may develop in the linear polarization curve.

In order to distinguish between flakes of a transparent, absorbing or a conducting material, we suggest that one should look at a combination of three scattering properties – polarization, color and polarimetric color – as a function of scattering angle. As illustrated in Figure 81, these three scattering properties will likely show a different combination of values for the three types of material, here represented from a) to c) by silicate (m = 1.62 –i0.003), carbon (m = 1.88 –i0.7) and metal assumed to be a perfect conductor. A transparent flake (Figure 81a) may be indicated by a combination of positive polarization and a correlation between color and polarimetric color. An absorbing flake (Figure 81b) will be indicated by positive polarization, blue color and neutral (i.e. zero) polarimetric color. In turn a conducting flake (Figure 81c) would be indicated by blue color and neutral polarization and polarimetric color.

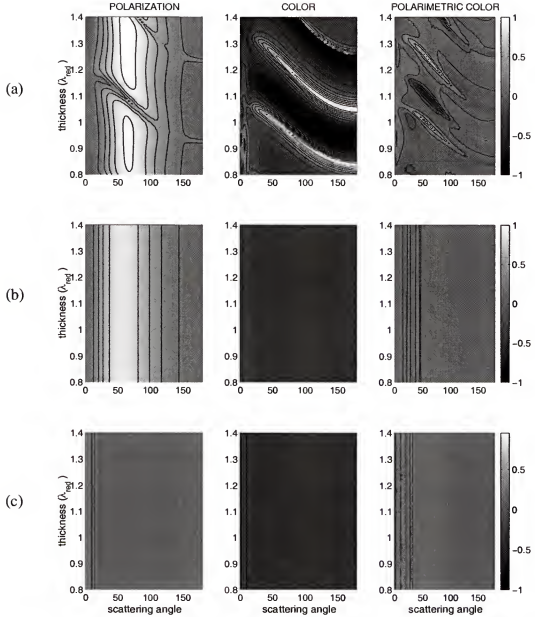

Figure 81: Simulations of the polarization (left column), color (center column) and polarimetric color (right column) of the light scattered by a square flake (with a side of 30 λ) as a function of scattering angle and thickness. The ratio of the longer and the shorter wavelength is 1.48, corresponding to the wavelength difference between red and blue wavelengths in the visual. In row (a) to (c) the material of the flake corresponds to (a) silicate ($m = 1.62 - i0.003$), (b) carbon ($m = 1.88 - i0.7$) and (c) metal assumed to be a perfect conductor. The color bar on the right is valid for all plots to the left.

CHAPTER 7
FLAKES IN COMETARY ATMOSPHERES

Cometary dust is believed to be an inhomogeneous collection of non-aligned non-spherical particles, which evolves as it moves away from the cometary nucleus. Observations of Comet Hale-Bopp (Jockers et al., 1997; Kolokolova et al., 2001) show rapidly changing light scattering properties in the inner coma (within 5000 km from the nucleus). Particularly, the color and polarization are much different than in the surrounding cometary atmosphere and cannot be explained by the light scattering from simple spherical particles. More complex particle geometries have been suggested. For example, evolving dust in the form of complex aggregates may explain these light scattering features (e.g. Kolokolova et al., 2001).

It has also been suggested that dust in the form of thin flakes may be produced by comets (e.g., Gustafson, 1990). In this chapter we investigate if thin flake-like dust particles, could explain light scattering features observed in comets. To explore this hypothesis, results of light scattering simulations using our theoretical model of the scattering by flakes (developed and tested in Chapters 4 and 5) are compared to the observations reported by Jockers et al. (1997) and Kolokolova et al. (2001). First, however, we present a brief review of comets and the cometary atmosphere, followed by a description of the process in which flakes may form and evolve.

7.1 What is a Comet?

A comet is an icy object thought to have formed in the outer solar nebula and today they are generally recognized as reservoirs of some of the most primitive material available in the solar system. The nucleus of a comet is a body with a typical dimension of a few kilometers composed of frozen gases (essentially water ice but also other ices such as e.g. CO, CO_2, NH_3 and CH_4) and silicate and organic dust. The activity of a comet that give rise to its often spectacular diffuse atmosphere and tail, is a result of the evaporation of the cometary ices. The evaporation of the ices takes place as the comet is heated by the solar radiation when its orbit brings it into the inner part of the solar system. The cometary atmosphere, also known as the coma, consists of the gas released from the nucleus together with dust grains being carried along with the escaping gas. The dust, once lifted off the nucleus surface, interacts with the sunlight and due to the radiation pressure a dust tail is formed. The gas is ionized by the ultraviolet light from the Sun and subsequently interacts with the solar wind to form a plasma tail. With highly eccentric orbits, however, comets spend most of their time at distances far away from the Sun where they remain frozen.

7.2 Cometary Dust Flakes

When discussing cometary dust it is common to refer to aggregated material of various nature, e.g. the Bird's-Nest model (Greenberg and Gustafson, 1981), which are thought of being aggregates of pristine interstellar grains. The Bird's-Nest aggregates are assumed to be released from active areas that expose matter, which has been protected in comet interiors. As the exposed ice sublimate, the dust particles are released. However, in order for dust particles to be lifted by the gas they need a sufficient surface-to-mass ratio.

Particles with lower ratio accumulate and, by trapping other dust grains in the gaps, a consolidated dust mantle may form nearly instantly (Shul'man, 1972; Rickman et al., 1990; Thiel et al., 1995). This mantle will stop the gas flow and shield the underlying material from direct sunlight. If gas pressure continues to build beneath the surface, it may eventually cause the mantle to rupture. Once the pressure exceeds the weight and cohesion of the mantle, the layer will burst resulting in the ejection of mantle fragments.

It has been suggested that a few layers of interstellar dust grains may suffice to efficiently quench the gas flow, subsequently causing the gas pressure to increase and rupture the layer, resulting in thin dust flakes being ejected into the coma. For example, in some computer models of the mantle formation by Rickman et al. (1990), thin layers of dust were carried away at the instant the gaps in the surface layer clogged up. A thin dust mantle may also be subject to fragmentation due to, e.g., thermal cracks or collisions puncturing the thin dust layer.

In laboratory experiments, Stephens and Gustafson (1991) found that thin flakes may indeed form on surfaces of sublimating dust/ice mixtures. Flakes may also be present in composite structures such as filamentary aggregates of clay particles, which if present will be released from a subliming ice surface (Saunders et al., 1986; Storrs et al., 1988; Sears et al., 1999).

Furthermore, the formation of dust flakes by a comet has also been suggested based on the dynamics of the Geminid meteoroids during atmospheric flight and of the Geminid meteor stream in space, which indicates that they may be flakes produced during cometary activity on asteroid 3200 Phaethon (Gustafson, 1990; Gustafson et al., 2000).

7.3 Observations of C/1995 O1 (Hale-Bopp)

In this section we give a brief review the observations of Comet C/1995 O1 Hale-Bopp (Jockers et al., 1997; Kolokolova et al., 2001) to which we will compare theoretical light scattering simulations for flakes. The observations (Figure 82) were made on March 31, 1997, at a phase angle of 47.8 degrees (with the comet at a distance of 0.91 AU from the Sun and 1.35 AU from the earth). In order to obtain colorimetric data, the observations, in the form of polarimetric CCD imaging, were carried out with a blue and a red narrowband filter. The two filters were centered at the wavelengths 443 nm and 642 nm, with bandwidths (FWHM) of 4.4 nm and 2.6 nm, respectively.

In Figure 83, profiles of the observed quantities (Figure 82) along the solar-antisolar direction (solar side positive while tail side negative) are shown. Hale-Bopp exhibits positive color that shows rapid increases with the distance away from the nucleus in both directions. Similarly the polarization rises with increasing distance from the nucleus. The polarimetric color is red with less spatial dependence and without an evident trend with regard to the distance from the comet nucleus.

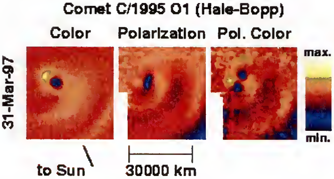

Figure 82: Images of color, polarization and polarimetric color observed in comet Hale-Bopp on March 31, 1997, at a phase angle of 47.8 degrees (Kolokolova et al., 2001). The displayed color ranges from 0% to 30 % per 100 nm; the polarization ranges from 12% to 20%; and the polarimetric color is in the range 1% to 5%.

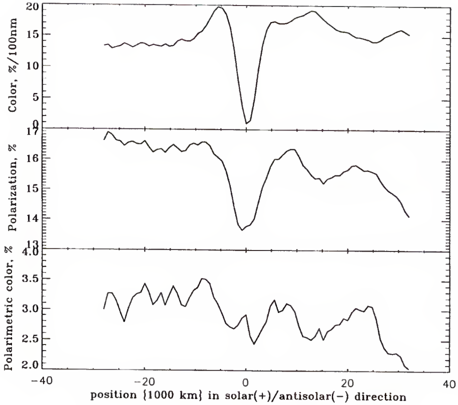

Figure 83: Color (% per 100 nm), polarization (%) and polarimetric color (%) in cuts through the coma of comet Hale-Bopp along the solar-antisolar direction through the images of Figure 82 (Kolokolova et al., 2001).

7.4 Modeling of Cometary Flakes

Here we use our light scattering approximation to simulate the light scattering by thin flakes with a thickness of up to 0.35 μm, i.e. typical of a few layers of interstellar particles. The narrow bandwidth of the filters used in the observations allows us to study the scattering by flakes with a narrow thickness distribution, thus no averaging over thickness is carried out. We look at the dependence of the light scattering properties on the refractive index and the thickness of the flake. The flakes are taken to be squares with a side of 8 μm, and the scattered light is calculated at the two wavelengths that the narrowband filter were centered on, i.e. 0.443 μm and 0.642 μm. The predicted light scattering properties are normalized with regard to the intrinsic color of the sun.

As the results of our theoretical simulations in this chapter are compared to observational data, we choose to present them as a function of the phase angle, which is the angle commonly used in comet observations. The phase angle is defined as the angle describing the angular distance between the observer and the Sun as seen from the comet. The phase angle is thus the complement to the scattering angle.

In Figure 84, the polarization of the light scattered by flakes with a refractive index corresponding to silicate with some organic content, m=1.7 - i0.1 is shown as a function of phase angle and the thickness of the flake. Figure 85 shows the polarization of the light scattered by flakes with a refractive index of pure silicate, with zero imaginary part (m=1.7 - i0.0). Next, Figure 86 and Figure 87 show the polarimetric color and color of the light scattered by flakes of refractive index 1.7 - i0.1 and 1.7 - i0, respectively.

In Figure 84 to Figure 87 one can see the following. First, the polarization is positive and has a maximum at medium phase angles. Second, there is a relation between the rather strong color and polarimetric color variations, i.e. when there is a change in color there is also a change in polarimetric color. Color and polarimetric color seem anti-correlated up to about 50 degrees. This dependence, however, should be considered with some caution because, if we were looking at an average of the scattering by truly randomly oriented flakes, the polarimetric color is expected to be neutral at small phase angles (Section 6.2). At larger phase angles, up to about 140 degrees, color and polarimetric color are strongly correlated. Third, when the imaginary part of the

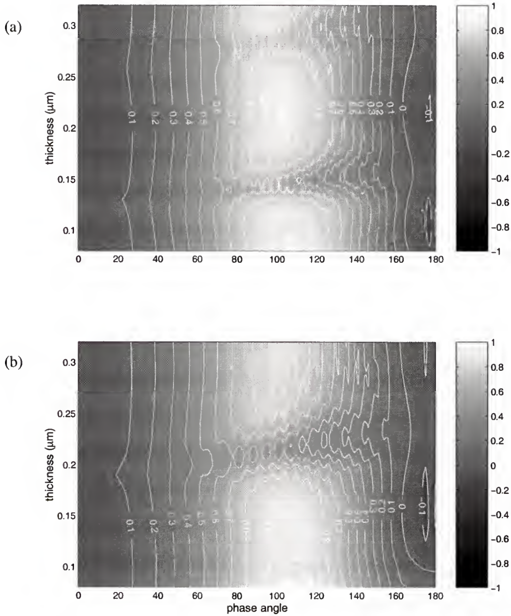

Figure 84: Theoretical predictions of the polarization of the scattered light by a square flake with a side of 8 μm, shown as a function of phase angle and thickness, at wavelengths 0.443 μm (a) and 0.642 μm (b). The refractive index is 1.7 - *i*0.1.

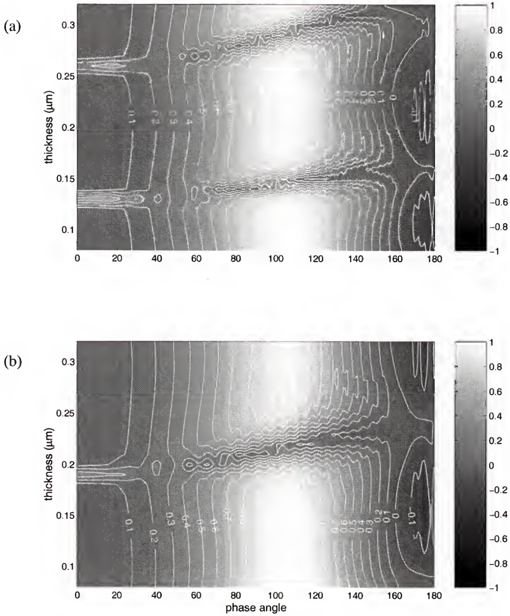

Figure 85: Theoretical predictions of the polarization of the scattered light by a square flake with a side of 8 μm, shown as a function of phase angle and thickness, at wavelengths 0.443 μm (a) and 0.642 μm (b). The refractive index is 1.7 - *i*0.

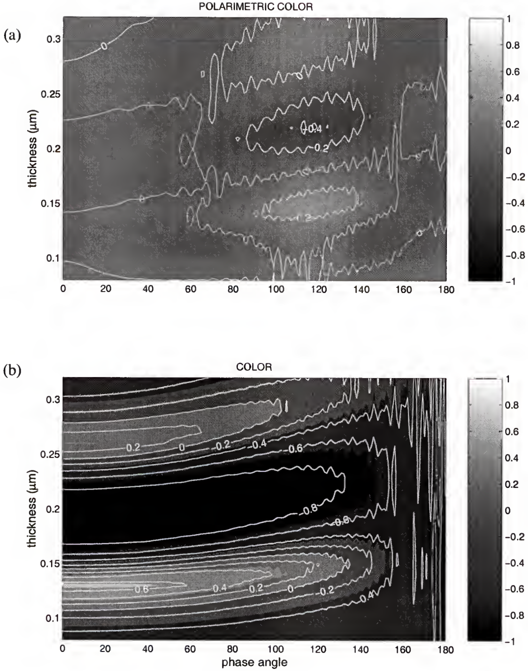

Figure 86: Theoretical predictions of the polarimetric color (a) and color (b) of the scattered light by a square flake with a side of 8 μm, shown as a function of phase angle and thickness. The refractive index is 1.7 - i0.1.

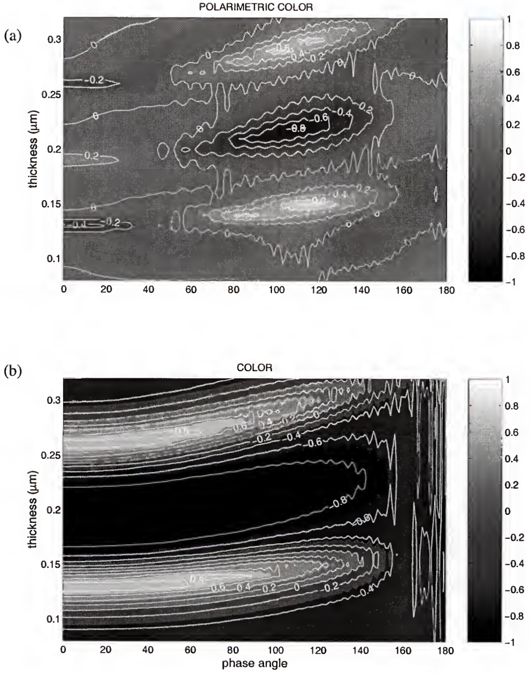

Figure 87: Theoretical predictions of the polarimetric color (a) and color (b) of the scattered light by a square flake with a side of 8 μm, shown as a function of phase angle and thickness. The refractive index is 1.7 - *i*0.

refractive index is increased the color is reduced and the polarimetric color becomes more neutral. In addition, when the real part of the refractive index is increased (not shown here) the trend is that the color variations are similar but shifted to smaller thickness.

7.5 Comparison with Observations

The wavelength dependence of the polarization in a coma is generally found to be flat for phase angles smaller than 30 degrees and increases with wavelength for larger phase angles (Chernova et al., 1993). In Figure 86 and Figure 87, we see, for the most part, that the polarimetric color is flat at smaller phase angles and increases with phase angle for flakes of thickness 0.12-0.17 μm and 0.25-0.32 μm. However, for flakes with thickness in the range 0.17-0.25 μm, the polarimetric color, in contrast, becomes blue at larger phase angles.

In the observations (made at a phase angle of 47.8 degrees) of comet Hale-Bopp (Jockers et al., 1997, Kolokolova, 2001) shown in Figure 83, we see that the overall color is red with a deep minimum near the nucleus. Red color in Figure 86 and Figure 87 at phase angle 47.8 degrees can be found at certain ranges in thickness, 0.12-0.15 μm and 0.25-0.28 μm, which more or less coincides with the regions of increasing red polarimetric color with phase angle. This is shown more clearly in Figure 88, where cuts through the contour plots in Figure 84 to Figure 87 have been plotted. (In Figure 88 polarization, color, polarization and polarimetric color have been added for flakes of refractive index m=1.7 - i0.05 to make the trends more visible).

It is thus found that the scattering by flakes of a certain range of thickness and refractive index may follow the general trends of the light scattering properties seen in the Hale-Bopp observations. However, can flakes explain the observed changes in the light scattering with increasing distance from the nucleus?

What may happen with the "flakes" as they move outward in the coma? We may expect two possible changes; (i) the flakes may become thinner. In the case of the above selected thickness regions (0.12-0.15 μm and 0.25-0.28 μm) the color becomes blue, which is not observed; (ii) if organic material is evaporating, one would expect the material to become more transparent, i.e. the imaginary part of the refractive index decreases. As seen in Figure 88, the result of lowering the absorption in the flake is that

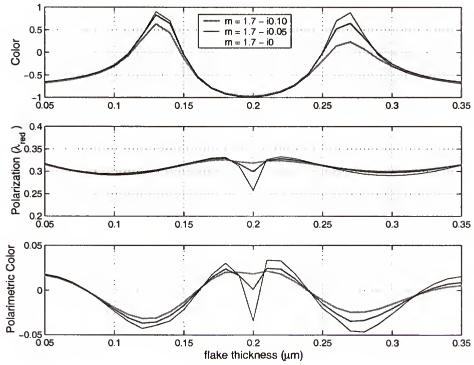

Figure 88: Theoretical predictions of the color, polarimetric color and polarization of the scattered light as a function of flake thickness and the imaginary part of the refractive index at phase angle of 47.8 degrees.

the color of the selected thickness regions increases, i.e. we have a reddening which does agree with observations. In the same thickness regions, there is a small decrease in polarimetric color and an even smaller decrease, if any, in polarization. However, as the change of polarization seen in the observations is relatively small and no obvious trend is visible in the polarimetric color, we cannot rule out dust flakes of certain mono-disperse thicknesses. The flake thickness regions (0.12-0.15 μm and 0.25-0.28 μm) for which the scattering is found to show similar trends as the ones seen in the observations are also consistent with the idea of the flakes consisting of a few layers of interstellar dust particles.

7.6 Summary

This chapter presents a comparison of light scattering features observed in the inner coma of comet Hale-Bopp and theoretically simulated light scattering properties of potential cometary dust flakes. The simulation of the light scattering properties of flakes is based on our approximate light scattering solution for a thin flake of arbitrary refractive index. We investigate the dependence of the color, polarization and polarimetric color on the refractive index and flake thickness.

Although, the scattering by flakes can not fully explain the specific light scattering features seen near the center of the coma, silicate flakes with some organic content and a thickness, typical of a few layers of interstellar dust grains, do show general scattering properties found for cometary dust, such as positive polarization with a maximum at medium phase angles, red color and an increase in polarimetric color with phase angle.

CHAPTER 8
SUMMARY AND CONCLUSIONS

We have developed an efficient new model for the scattering of electromagnetic radiation by a thin dielectric plate within the premises of the geometrical theory of diffraction. Our scattering model bridges the gap between low-frequency methods such as, for example, the discrete dipole approximation, and high-frequency approaches such as the geometric optics approximation.

After a review of the geometrical theory of diffraction and the impedance boundary conditions (Chapter 2) and a description of the microwave scattering facility (Chapter 3), where the test measurements were made for the assessment of the scattering model, the developed scattering model was derived (Chapter 4), assessed (Chapter 5) and applied to examine the scattering properties of flakes in general (Chapter 6) and of cometary dust in particular (Chapter 7).

The developed scattering model (Chapter 4) is based on the scattering by a rectangular flake, which is oriented in such a way that two of its edges are kept perpendicular to the scattering plane. From this geometry follows, that the normal to the flake's large surfaces is always directed in the scattering plane. The scattered radiation from the flake is viewed as a sum of two separate parts, which we refer to as (i) the externally scattered radiation and (ii) the transmitted scattered radiation. The finite thickness of the flake is first neglected and the flake is treated as if it is infinitesimally thin. The externally scattered field is determined by treating each of the two edges (perpendicular to the scattering plane) as an edge to a semi-infinite half-plane, from which the diffraction can be described using an impedance boundary condition solution. The transmitted scattered field, on the other hand, is approximated to the field diffracted through an opening of the same width and height as the flake. The dielectric properties of the flake are taken into account via a set of effective reflection and transmission coefficients, which includes all internal reflections and relates the transmitted field to the externally scattered field. The two separately treated parts are ultimately added together with the proper phase relation. That is, at this point, the finite thickness of the flake is taken into account.

Impedance boundary conditions are approximate and derived under the assumption that the refractive index is much greater than one. In order compensate for the inaccuracy inherent to the impedance boundary conditions for a lower refractive index we introduced (i) an effective refractive index and (ii) a corresponding correction factor. The introduction of an effective refractive index ensures a better description of the shape of the diffraction pattern, in particular when the radiation is incident at an angle near the Brewster angle. The correction factor adjusts the amplitude of the scattered radiation in the direction of the specular reflection.

The validity of our scattering model was assessed by a number of comparisons with laboratory microwave measurements carried out in the wavelength interval 2.7 – 4 mm (Chapter 5). Specifically, we looked at the angular and wavelength dependence of intensity and polarization to evaluate the model. A set of flakes ranging from a few to many wavelengths in size and with refractive indices of $1.62 - i0.003$ (acrylic) and $2.52 - i0.03$ (Bk7 glass) were used to test the accuracy of the model. In general, a good agreement is found between the predictions of our scattering model and the microwave measurements, when the large dimensions of the flake are at least 6 λ and the aspect ratio (width/thickness) is at least 25 (corresponding to a surface-equivalent-sphere size parameter of 16). A large aspect ratio ensures that the contribution from the edges, which our model does not account for, can be neglected in comparison to the scattering from the large faces of the flake. Moreover, it was shown that the model does predict the correct trends of the light scattering properties, even for a flake as small as 3 λ across.

As with any high-frequency method, the outcome improves for scattering objects with greater dimensions and it was shown that, when the dimensions of the flake are increased, the prediction of our scattering model approaches the result of the geometric optics approximation. Thus, our model can be used to simulate the scattering by flakes as small as a few wavelengths in size, as well as large flakes in the geometric optics regime. Furthermore, the use of impedance boundary conditions in modeling of the externally scattered radiation entails that the results also improve with a greater refractive index.

We also evaluated the possibility of using our model to describe the scattering by flakes in general and found that the model may be used to deduce scattering properties of flakes with other convex shapes. This was exemplified by measurements of the scattering by circular flakes. By comparing the scattering by flakes in different distributions of orientations we also found that the properties of the scattered light averaged over rotation computed with our model, offer a good approximation of the scattering properties for randomly oriented flakes. This is due to the fact that the former average includes the specular reflection, which appears to be the dominating contribution to the scattered light by randomly oriented of flakes. The scattering properties by randomly oriented flakes are of interest when the light is scattered by a large collection of non-aligned flakes.

In Chapter 6, the developed and tested scattering model was applied in a comprehensive study of the light scattering properties of thin flakes. It was found that if interference effects are suppressed (e.g., because of absorption within the flake), the linear polarization is relatively independent of the flake thickness. The linear polarization curve resembles the polarization of Rayleigh scattering with a bell-like shape and a maximum polarization, P_{max}, of almost 100%. However, in contrast to Rayleigh scattering, the location of P_{max} is, depending on refractive index, shifted towards smaller scattering angles. In the case of transparent flakes with a narrow thickness distribution, the effect of interference makes both intensity and polarization strongly wavelength dependent, which in turn gives rise to correlated variations in color and polarimetric color at scattering angles in the interval 20 – 100 degrees. In the case of larger transparent flakes, characteristic deep minima may develop in the linear polarization curve. The polarimetric and correlated spectral light scattering characteristics found in our investigation might be used as indicators for flakes.

In Chapter 7, the scattering model is used to investigate if thin flake-like dust particles can show light scattering properties observed in cometary atmospheres. We found that silicate flakes with some organic content and a thickness, consistent with a few layers of interstellar dust grains, do show general properties found in the scattering by cometary dust. These include positive polarization with a maximum at medium phase angles, red color and an increase in polarimetric color with phase angle.

APPENDIX
PRINCIPLE OF ELECTRODYNAMIC SIMILITUDE

The possibility of scaling a model of a given electromagnetic boundary problem arises from the linearity of Maxwell's equations and is referred to as the principle of electrodynamic (or electromagnetic) similitude. The principle of electrodynamic similitude is here derived from Maxwell's equations following Stratton (1941). As the starting point we take the Maxwell's equations for the macroscopic electromagnetic field in a homogenous and isotropic matter,

$$\begin{aligned} \nabla \times \mathbf{E} &= -\mu \frac{\partial \mathbf{H}}{\partial t} \\ \nabla \times \mathbf{H} &= \varepsilon \frac{\partial \mathbf{E}}{\partial t} + \sigma \mathbf{E} \end{aligned} \qquad \text{(A-1)}$$

In order to write these field equations in a dimensionless form, the following parameters are defined,

$$\begin{gathered} \mathbf{E} = e\mathsf{E} \qquad \mathbf{H} = h\mathsf{H} \\ \varepsilon = \varepsilon_0 \mathsf{e} \qquad \mu = \mu_0 \mathsf{m} \qquad \sigma = \sigma_0 \mathsf{s} \\ \text{length} = l_0 \mathsf{L} \qquad \text{time} = t_0 \mathsf{T} \end{gathered} \qquad \text{(A-2)}$$

where E, H, e, m, s, L and T are the dimensionless measure numbers of the field variables in a system for which the unit quantities are e, h, ε_0, μ_0, σ_0, l_0 and t_0. Equation (A-1) can now be rewritten

$$\begin{aligned} \nabla \times \mathsf{E} &= -\alpha \mathsf{m} \frac{\partial \mathsf{H}}{\partial \mathsf{T}} \\ \nabla \times \mathsf{H} &= \beta \mathsf{e} \frac{\partial \mathsf{E}}{\partial \mathsf{T}} + \gamma \mathsf{s} \mathsf{E} \end{aligned} \qquad \text{(A-3)}$$

where

$$\alpha = \frac{\mu_0 l_0}{t_0}\frac{h}{e}, \qquad \beta = \frac{\varepsilon_0 l_0}{t_0}\frac{e}{h}, \qquad \gamma = \sigma_0 l_0 \frac{e}{h}, \tag{A-4}$$

are dimensionless constants. In order for two electromagnetic boundary-value problems to be similar, it is only necessary that the coefficients αm, βe and γs are identical in both. By multiplying α with β and α with γ, the common ratio *e/h* in (A-4) can be eliminated, and the result is the following expressions

$$\mu_0\varepsilon_0\left(\frac{l_0}{t_0}\right)^2 = \text{constant}, \quad \mu_0\sigma_0\frac{l_0^{\,2}}{t_0} = \text{constant}. \tag{A-5}$$

For t_0 let us take the period T of the field, and for l_0 any length L that characterizes the size of the body on which the field is incident. The condition of similitude requires that the two characteristic parameters C_1 and C_2 in

$$\mu\varepsilon\left(\frac{L}{T}\right)^2 = C_1, \quad \mu\sigma\frac{L^2}{T} = C_2, \tag{A-6}$$

to be invariant to a change of scale. Suppose that the characteristic length L is halved. Then if ε and μ are left as they were, C_1 remains unchanged if the frequency is doubled. This alone does, however, not take care of C_2. In order for the half-scale model to exactly reproduce the full-scale conditions, it is also necessary to double the conductivity. Thus, it will be difficult to model large things with a high conductivity such as copper into smaller things at higher frequencies. This modeling difficulty also means that an oscillator built after a design to work at one frequency might fail to operate at a higher frequency due to a higher relative loss. In other instances it is sufficient to treat both the original device and model as perfect conductors, e.g. in the case of a cylindrical antenna

(King, 1945), the distribution of current and charge depends only in negligible degree on its conductivity, provided this is high, and the actual antenna of copper can be modeled in copper.

In the problem of electromagnetic scattering by particles, it is only the alternating field conductivity σ_a, which enter Maxwell's equations. The alternating field conductivity is often written in form of the imaginary part of the dielectric constant $\varepsilon'' = \sigma_a/\omega$. Hence, with the total dielectric constant $\varepsilon = \varepsilon' + j\varepsilon''$, Maxwell's equations can be written as

$$\begin{aligned} \nabla \times \mathbf{E} &= -\mu \frac{\partial \mathbf{H}}{\partial t} \\ \nabla \times \mathbf{H} &= \varepsilon \frac{\partial \mathbf{E}}{\partial t} \end{aligned} \tag{A-7}$$

and it is only necessary to consider

$$\mu\varepsilon\left(\frac{L}{T}\right)^2 = C_1 \tag{A-8}$$

from (A-6) invariant. By rewriting this expression in terms of the wavelength instead of the period,

$$\mu\varepsilon\left(\frac{L}{T}\right)^2 = \mu\varepsilon\left(\frac{Lc}{\lambda}\right)^2 = \left(\frac{L}{\lambda}\right)^2 = C_1 \tag{A-9}$$

it is seen that the scattering depends only on the ratio of particle size to wavelength. This has led to the widespread use of the size parameter, $2\pi a/\lambda$, i.e. the ratio of the circumference of a sphere with radius a to the wavelength λ. The concept of size parameter is also used when comparing the scattering from particles with other shapes than the sphere. In this case a is replaced by the radius of a sphere with same volume as the non-spherical particle, and hence the parameter referred to as the equal volume size parameter, is formed.

If the permittivity or permeability is wavelength dependent as they usually are, it is necessary to make the scattering model out of an *analog material*, which has the refractive index of the scattering object in the original scattering problem at the wavelength at which the scaled experiment is carried out.

LIST OF REFERENCES

Asano, S., and G. Yamamoto, "Light scattering by a spheroidal particle," *Appl. Opt. 14*, 29-49, 1975.

Balanis, C. A., *Antenna Theory: Analysis and Design*, John Wiley & Sons, New York, 1982.

Balanis, C. A., *Advanced Engineering Electromagnetics*, John Wiley & Sons, New York, 1989.

Barber, P., and C. Yeh, "Scattering of electromagnetic waves by arbitrarily shaped dielectric bodies," *Appl. Opt. 14*, 2864-2872, 1975.

Bohren, C. F., and D. R. Huffman, *Absorption and Scattering of Light by Small Particles,* John Wiley & Sons, New York, 1983.

Bouche, D. P., F. A. Molinet, and R. M. Mittra, "Asymtotic and hybrid techniques for electromagnetic scattering," *Proc. IEEE. 81(12),* 1658-1684, 1993.

Burnside, W. D., and K. W. Burgener, "High frequency scattering by a thin lossless dielectric slab," *IEEE.Trans. Antennas Propag. AP-31*, 104-110, 1983.

Chernova, G. P., N. N. Kieslev, and K. Jockers "Polarimetric characteristics of dust Particles as observed in 13 comets: comparisons of asteroids," *Icarus 103*, 144-158, 1993.

Draine, B. T., "The discrete-dipole approximation and its application to interstellar graphite grains," *Astrophys. J. 333*, 848-872, 1988.

Draine, B. T., "The discrete dipole approximation for light scattering by irregular targets," in *Light scattering by nonspherical particles*, eds., M. I. Mishchenko, J. W. Hovenier, and L. D. Travis, Academic Press, New York, pp.131-145, 2000.

Draine, B. T., and P. J. Flatau, "Discrete dipole approximation for scattering calculations," *J. Opt. Soc. Amer. A, 11*, 1491-1499, 1994.

Draine, B. T., and P. J. Flatau, *User guide for the discrete dipole approximation code DDSCAT (version 5a10)*, http://atol.ucsd.edu/~pflatau/scatlib/index.html (accessed 12/06/2001), 2000.

Draine, B. T., and J. J. Goodman, "Beyond Clausius-Mosetti: Wave propagation on a polarizable point lattice and the discrete dipole approximation," *Astrophys. J. 405*, 685-697, 1993.

Greenberg, J. M., and B. Å. S. Gustafson, "A comet fragment model for Zodiacal light particles," *Astron. Astrophys.* 93, 35-42, 1981.

Greenler, R., *Rainbows, Halos and Glories*, Peanut Butter Publishing, Milwaukee, 1999.

Gustafson, B. Å. S., "Comet ejection and dynamics of nonspherical dust particles and meteoroids," *Astrophys. J. 337*, 945-949, 1989a.

Gustafson, B. Å. S., "Geminid meteoroids traced to cometary activity on Phaethon," *Astron. Astrophys. 225*, 533-540, 1989b.

Gustafson, B. Å. S., "Are the Geminids high density porous flakes from a surface crust on Phaethon?" in *Asteroids, Comets Meteors III*, C. -I. Lagerkvist, B. A. Lindblad, P. Magnusson, and H. Rickman, eds., Uppsala Univ. Press, Uppsala, pp. 523-526, 1990.

Gustafson, B. Å. S., "Physics of Zodiacal dust," *Ann. Rev. of Earth and Planetary Sciences 22*, 553-595, 1994.

Gustafson, B. Å. S., "Microwave analog to light scattering: a modern implementation of a proven method to achieve precise control," *J. Quant. Spectrosc. Radiat. Transfer 55(5)*, 663-672, 1996.

Gustafson, B. Å. S., L. Adolfsson, D. Liljeblad, and T. Sigfrids, "Evidence from atmospheric deceleration that Geminids are spinning flakes," Poster presented at International Astronomical Union Colloquium 181 in Canterbury, England. April 10-14, 2000.

Gustafson, B. Å. S., L. Kolokolova, "A systematic study of light scattering by aggregate particles using the microwave analog technique: Angular and wavelength dependence of intensity and polarization," *Journal of Geophysical Research 104(D24)*, 31711-31720, 1999.

Harrington, R. F., *Field Computation by Moment Methods*, Macmillan, New York, 1968.

Herman, M. I., and J. L. Volakis, "High frequency scattering by a resistive strip and extensions to conductive and impedance strips," *Radio Sci. 22*, 335-349, 1987.

Herman, M. I., J. L. Volakis, and T. B. A. Senior, "Analytic expressions for a function occurring in diffraction theory," *IEEE.Trans. Antennas Propag. AP-35*, 1083-1086, 1987.

Jackson, J. D., *Classical Electrodynamics*, John Wiley & Sons, New York, 1975.

Jockers, K., V. K. Rosenbuch, T. Bonev, and T. Credner,Earth, "Images of polarization and colour in the inner coma of comet Hale-Bopp," Earth, Moon and Planets 78, 373, 1997.

Keller, J. B., "Geometrical theory of diffraction," *J. Opt. Soc. Amer. 52(2),* 116-130, 1962.

Kolokolova, L., K. Jockers, and G. Chernova, "Properties of cometary dust from color and polarization," *Icarus 126*, 351-361, 1997.

Kolokolova, L., K. Jockers, B. Å. S. Gustafson, and G. Lichtenberg, "Color and Polarization as indicators of comet dust properties and evolution in the near-nucleus coma," *Journal of Geophysical Research, 106*, 10113-27, 2001.

Kouyoumjian R. G., "The geometrical theory of diffraction and its applications," in *Numerical and Asymtotic Techniques in Electromagnetics*, R. Mittra, eds., Springer, New York, pp. 165-215, 1975.

Kouyoumjian, R. G., and P. H. Pathak, "A uniform geometrical theory of diffraction for an edge in a perfectly conducting surface," *Proc. IEEE 62*, 1448-1481, 1974.

Ksienski, D. A., and T. B. A. Senior, "Scattering by small thin dielectric particles," *Appl. Phys. B 38*, 225-231, 1985.

Kuik, F., J. F. de Haan, and J. W. Hovenier, "Single scattering of light by circular cylinders," *Appl. Opt. 33*, 4906-4918, 1994.

Leontovich, M. A., *Investigations on Radiowave Propagation, Part II*, Printing House of the Academy of Sciences, Moscow, 1948.

Le Vine, D. M., R. H. Lang, and S. S. Seker, "Scattering from arbitrarily oriented dielectric disks in the physical optics regime," *J. Opt. Soc. Am. 73(10),* 1255-1262, 1983.

Le Vine, D. M., A. Schneider, R. H. Lang, and H. G. Carter, "Scattering from thin dielectric disks," *IEEE.Trans. Antennas Propag. AP-33*, 1410-1413, 1985.

Lorenz, L. V., "Sur la lumière réfléchie et réfractée par une sphere transparente," in *Qeuvres Scientifiques de L.. Lorenz*, revues et anotées par H. Valentiner, Leman et Stage, Copenhagen, pp. 405-529, 1898.

Macke, A. "Scattering of light by polyhedral ice crystals," *Appl. Opt. 32,* 2780-2788, 1993.

Maliuzhinets, G. D., "Excitation, reflection and emission of surface waves from a wedge with given face impedances," *Sov. Phys. Doklady 3*, 752-755, 1958.

Meixner, J., and W. Andrejewski, "Strenge Theorie der Beugung ebner elektromagnetischer Wellen an der vollkommen leitenden ebenen Schirm," *Ann. Phys. 7*, 157, 1950.

Mie, G.,"Beiträge zur Optik trüber Medien, speziell kolloidaler Metallösungen," *Ann. Phys. 25*, 377-445, 1908.

Mishchenko, M. I., and L. D. Travis, "T-matrix computations of light scattering by large spheroidal particles," *Opt. Commun. 109,* 16-21, 1994.

Mishchenko, M. I., and L. D. Travis, "Capabilities and limitations of current FORTRAN implementation of the T-matrix method for randomly oriented, rotationally symmetric scatterers," *J. Quant. Spectrosc. Radiat. Transfer 60,* 309-324, 1998.

Mishchenko, M. I., D. J. Wielaard, and B. E. Carlson, "T-matrix computations of zenith-enhanced lidar backscatter from horizontally orientated ice plates," *Geophys. Res. Lett. 24,* 771-774, 1997.

Platt, C. M. R., "Lidar backscatter from horizontal ice crytal plates," *J. Appl. Meteorol. 17*, 482-488, 1978.

Purcell, E. M., and C. R. Pennypacker, "Scattering and absorption of light by nonspherical dielectric grains," *Astrophys. J. 186*, 705-714, 1973.

Rayleigh, Lord, "On the incidence of aerial and electric waves upon small obstacles in the form of ellipsoids or elliptic cylinders, and on the passage of electric waves through a circular aperture in a conducting screen," *Philos. Mag. 44*, 28-52, 1897.

Rickman, H., J. A. Fernández, and B. Å. S. Gustafson, "Formation of stable dust mantles on short-period comet nuclei," *Astron. Astrophys. 237(2),* 524-535, 1990.

Rouviere, J.-F., N. Douchin, and P. F. Combes, "Diffraction by lossy dielectric wedges using both heuristic UTD formulations and FDTD," *IEEE.Trans. Antennas Propag. AP-47*, 1702-1708, 1999.

Saunders, R. S., F. P. Fanale, T. J. Parker, J.B Stephens, and S. Sutton, "Properties of filamentary residues from dispersions of clay in ice," *Icarus 66*, 94-104, 1986.

Sears, D. W. G., H. W. Kochan, and W. F. Huebner "Laboratory simulation of the physical processes occurring on and near the surfaces of comet nuclei," *Meteoritics & Planetary Science 34*, 497-525, 1999.

Senior, T. B. A., "Impedance boundary conditions for imperfectly conducting surfaces," *Appl. Sci. Res. B 8*, 418-436, 1960.

Senior, T. B. A., "Half-plane edge diffraction," *Radio Sci. 10*, 645-650, 1975.

Senior, T. B. A., and J. L. Volakis, *Approximate Boundary Conditions in Electromagnetics*, The Institution of Electrical Engineers, London, 1995.

Shul'man, L. M. "The evolution of cometary nuclei," in *The Motion, Evolution of Orbits, and Origin of Comets*, G. A. Chebotarev, E. I. Kazimirchak-Polonskaya, and B. G. Marsden, eds, pp. 271-276, Dordrecht, Reidel, 1972.

Spitzer, L., *Physical processes in the interstellar medium*, John Wiley & Sons, New York, 1978.

Stephens, J.R. and B. Å. S. Gustafson, "Laboratory reflectance measurements of analog to "dirty" ice surfaces on atmosphereless solar system bodies," *Icarus 94*, 209-217, 1991.

Storrs, A. D., F. P. Fanale, R. S. Saunders, and J.B Stephens, "The formation of filamentary sublimate residues (FSR) from mineral grains," *Icarus 76*, 493-512, 1988.

Stratton, J. A. *Electromagnetic Theory*, McGraw-Hill, New York, 1941.

Syed, H. H. and J. L. Volakis, "An approximate solution for scattering by an impedance wedge at skew incidence," *Radio Sci. 30*, 505-524, 1995.

Thiel, K., G. Kölzer, H. Kochan, P. Lämmerzahl, and E. Lorenz, "Phenomenology and dynamic behavior of the dust component in the KOSI experiments," *Planet. Space Sci. 43(3/4),* 375-390, 1995.

Twersky, V., "Multiple scattering of waves and optical phenomena," *J. Opt. Soc. Amer. 52(2),* 145-171, 1962.

Van Bladel, J. "Some remarks on Green's dyadic for infinite space," *IRE Trans. Antennas Propag. 9*, 563-566, 1961.

van de Hulst, H. C., *Light Scattering by Small Particles*, Dover Publications, Inc., New York, 1957.

Volakis, J. L., "A uniform geometrical theory of diffraction for an imperfectly conducting half-plane," *IEEE.Trans. Antennas Propag. AP-34*, 172-180, 1986.

Wait, J. R., "Scattering of a plane wave from a circular dielectric cylinder at oblique incidence," *Can. J. Phys. 33*, 189-195, 1955.

Waldemarsson, K. W. T., and B. Å. S. Gustafson, "Light scattering by thin flakes," in *Light scattering by nonspherical particles: Halifax contributions*, G. Videen, Q. Fu, and P. Chýlek, eds., US Army Research Laboratory, Adelphi, Maryland, pp. 34-37, 2000.

Waterman, P. C., "Matrix formulation of electromagnetic scattering," *Proc. IEEE 53*, 805-812, 1965.

Weil, H., and C.-M. Chu, "Scattering and absorption of electromagnetic radiation by thin dielectric disk," *Appl. Opt. 15*, 1832-1836, 1976.

Wielaard, D. J., M. I. Mishchenko, A. Macke, and B. E. Carlson, "Improved T-matrix computations for large, nonabsorbing and weakly absorbing nonspherical particles," *Appl. Opt. 36,* 4305-4313, 1997.

Yanamandra-Fisher, P. A., and M. S. Hanner, "Optical properties of nonspherical particles of size comparable to the wavelength of light: application to comet dust," *Icarus 138*, 107-128, 1999.

Zakharova, N. T., and M. I. Mishchenko, "Scattering properties of needlelike and platelike ice spheroids with moderate size parameters," *Appl. Opt. 39*, 5052-5057, 2000.

Zakharova, N. T., and M. I. Mishchenko, "Scattering by randomly oriented thin ice disks with moderate equivalent-sphere size parameters," *J. Quant. Spectrosc. Radiat. Transfer*, 70, 465-71, 2001.

BIOGRAPHICAL SKETCH

K. W. Tomas Waldemarsson was born on September 19, 1969, in Skövde, Sweden, the son of Sixten and Rut Waldemarsson. He grew up in the village of Sjogerstad just outside Skövde with his parents and younger sister Ulrika. In between graduating from Västerhöjdskolan (Upper Secondary School in Skövde) in the summer of 1989, and his service in the Swedish army that began in the spring of 1990, Tomas traveled through Europe and somewhat by chance he found employment at Ultralight AG in Liechtenstein. Here, he gained experience in the manufacturing of ultraviolet lamps (used in various curing processes) and in the challenging art of blowing quartz. Later, during his university studies he would come back to work at Ultralight during the summers. In the Swedish army he served as *Trafikare*, a position where he worked with traffic regulation and the movement (or *scattering)* of large troops.

In the fall of 1991 Tomas moved to Stockholm to study engineering physics at the Royal Institute of Technology. After a year at the Federal Institute of Technology, Zürich, and upon completing his master's thesis at CERN, Geneva, he was awarded his Master of Science degree in December 1995. Tomas then enrolled in the astronomy graduate program at the University of Florida where he studied light scattering and gained experience in the development of space instrumentation under the guidance of Dr. Bo Gustafson. Tomas will receive his doctorate degree in December of 2001.

I certify that I have read this study and that in my opinion it conforms to acceptable standards of scholarly presentation and is fully adequate, in scope and quality, as a dissertation for the degree of Doctor of Philosophy.

Bo Å. S. Gustafson, Chairman
Professor of Astronomy

I certify that I have read this study and that in my opinion it conforms to acceptable standards of scholarly presentation and is fully adequate, in scope and quality, as a dissertation for the degree of Doctor of Philosophy.

Ewan M. Thomson
Associate Professor of Electrical and Computer Engineering

I certify that I have read this study and that in my opinion it conforms to acceptable standards of scholarly presentation and is fully adequate, in scope and quality, as a dissertation for the degree of Doctor of Philosophy.

Stan F. Dermott
Professor of Astronomy

I certify that I have read this study and that in my opinion it conforms to acceptable standards of scholarly presentation and is fully adequate, in scope and quality, as a dissertation for the degree of Doctor of Philosophy.

Yu-Lin Xu
Associate Scientist, Astronomy

I certify that I have read this study and that in my opinion it conforms to acceptable standards of scholarly presentation and is fully adequate, in scope and quality, as a dissertation for the degree of Doctor of Philosophy.

R.K. P

Robert K. Piña
Assistant Professor of Astronomy

I certify that I have read this study and that in my opinion it conforms to acceptable standards of scholarly presentation and is fully adequate, in scope and quality, as a dissertation for the degree of Doctor of Philosophy.

Ludmilla Kolokolova
Assistant Scientist, Astronomy

This dissertation was submitted to the Graduate Faculty of the Department of Astronomy in the College of Liberal Arts and Sciences and to the Graduate School and was accepted as partial fulfillment of the requirements for the degree of Doctor of Philosophy.

December, 2001

Dean, Graduate School